INTERNATIONAL ATOMIC ENERGY AGENCY
UNITED NATIONS EDUCATIONAL, SCIENTIFIC AND CULTURAL ORGANIZATION
INTERNATIONAL CENTRE FOR THEORETICAL PHYSICS
I.C.T.P., P.O. BOX 586, 34100 TRIESTE, ITALY, CABLE: CENTRATOM TRIESTE

SMR.550 - 31

SPRING COLLEGE IN MATERIALS SCIENCE ON

"NUCLEATION, GROWTH AND SEGREGATION IN MATERIALS SCIENCE AND ENGINEERING"

(6 May - 7 June 1991)

BACKGROUND MATERIAL FOR SEMINAR ON

"THE THEORY OF SINTERING AND THE EFFECTS OF ANISOTROPY OF SURFACE AND GRAIN BOUNDARY ENERGIES ON SINTERING"

Part II

J.L. BLENDELL
United States Department of Commerce
National Institute of Standards and Technology
Building 223, A215
Gaithersburg, Maryland 20899
U.S.A.

SINTERING OF CERAMICS

Dr.John E. Blendell

Ceramics Division
Materials Science and Engineering Laboratory
National Institute of Standards and Technology
Gaithersburg, MD 20899 USA

Recent theories of sintering of ceramics have greatly advanced our understanding of the underlying physical processes. Models have been developed which include multiple atomic transport mechanisms, surface and interface anisotropy, impurity effects and complex geometries. These models are closer to the situations in actual powder samples than the first order modelling previously used. While none of these effects have been completely understood, their importance is now known and furthermore the interrelationships among them are recognized.

These lectures will give an overview of sintering, some practical examples and will discuss the effect of anisotropy. The theory of the sintering of ceramics will be presented. The first section will be on the thermodynamics (driving forces) and the kinetics (mechanisms and paths) of solid state sintering. The second section will discuss the effects due to the presence of additional phases (solid and liquid) and external driving forces (mechanical and chemical). The third section will present effects of anisotropy and will contain current research on the effect of crystal symmetry on interface migration in the presence of a liquid phase, grain boundary migration and facetting of solid-vapor interfaces.

SINTERING OF CERAMICS

Carol A. Handwerker, John E. Blendell, and Robert L. Coble*

National Institute of Standards and Technology
Materials Science and Engineering Laboratory
Gaithersburg MD 20899 USA

*Massachusetts Institute of Technology
Cambridge MA 02139 USA

INTRODUCTION

The primary goal of sintering research is the controlled manipulation of microstructure. Out of the entire range of microstructures which are theoretically possible, each material system will be able to achieve only a subset of them, depending on the intrinsic material properties. Within these material constraints, the aim is to produce microstructures which enhance specific properties. Our understanding of the relationships among materials processing, microstructure, and properties is just beginning to emerge, and is producing unexpected results. For example, in a recent study of toughness in Al_2O_3 by Bennison and Lawn, microstructures with platy grains and a bimodal grain size distribution in undoped Al_2O_3 exhibited a greater resistance to crack propagation than did the more uniform microstructures in MgO-doped Al_2O_3 [1]. As a result of this emerging understanding, the focus of sintering science is changing from the modification of microstructures in incremental ways for correspondingly incremental improvement in properties to more effectual manipulation of microstructures to optimize properties. However, the production of the optimum microstructure will be dependent on both the material and the application and may require radically different processing routes for different materials. In this review paper, we have examined the research in sintering science over the past five years which has advanced the goal of microstructure manipulation.

THEORETICAL MODELLING AND MODEL MICROSTRUCTURES

Over the past five years, substantial progress has been made in developing more realistic sintering models and in designing materials to test these theories. The basis of the current theoretical advancement is that the specific set of coupled kinetic processes operating in certain systems can be separated and, thus, the enthusiasm for the modelling of competing mechanisms in sintering has been restored. When the sintering of a system cannot be categorized by a small subset of possible sintering processes, simplified geometries can be used to examine the roles of various processes in

Science of Sintering
Edited by D. P. Uskokovic *et al.*
Plenum Press, New York

microstructure development. The recent advances in sintering experiments have been made possible by a revolution in the control of powder characteristics and processing. This revolution, fomented by H. K. Bowen, provides enormous flexibility in the design of specific microstructures [2]. In the following discussion, theories and their complementary model experiments are discussed together.

The simplest model whose use continues to provide insight is the two-sphere model. An example of recent results is the numerical simulation of neck growth by surface and grain boundary diffusion [3]. In agreement with previous studies [4], there exists a limiting ratio of grain boundary diffusivity to surface diffusivity above which the densification rate does not increase because surface diffusion is required to redistribute matter in the region of the neck.

The next step in geometrical complexity, is the sintering of a row of spheres. For this geometry, the number of concurrent processes which can be treated is large because each particle has only two neighbors and, if is assumed that there are no torques on the particles to rotate them out of the axially symmetrical position, the mathematical statement of the problem is simplified. An important new development is that differential densification has now been treated in a row of spheres by allowing a section of the chain to begin to densify before the rest of the chain [5,6]. It has been calculated that, when the other sections begin to densify the chain will either become uniform in its sintering or will break up catastrophically into individual segments depending on the relative rates of coarsening and densification and the dihedral angle.

This problem of differential densification and development of heterogeneous microstructures has recently been a topic of intense theoretical and experimental investigation [7-15]. The approach has been from two extremes in initial microstructures. In the first, mono-sized powders are packed and sintered, and the size of final defects are correlated with the initial amount of ordering [12,13]. In the second case, dense inclusions are placed into a powder compact and the effect of the non-densifying inclusions on the densification rate of the matrix is evaluated [14]. These two approaches reflect the extremes seen in the technology of powder processing with controlled composition and physical characteristics and of processing of ceramic-matrix composites. The types of heterogeneities examined over the last 5 years range from large cracks between regions of perfect packing to large spherical pores in a matrix containing smaller pores, to sintering of a porous matrix around a higher density spherical inclusion. The advances in sintering of composites are summarized in the next section.

A major result is that the maximum sintering stress is on the order of 0.1 - 2 MPa regardless of microstructure [7-11]. This result is important because the sintering stress determines the opposing tensile stress required to keep particles from densifying or, for higher tensile stresses, to pull particles apart. The size of the sintering stress is a major factor in specifying HIP'ing and hot pressing conditions to improve reliability of sintered composites.

Experiments on 2-D arrays of monosized or bimodally-sized particles have shown that crack-like defects develop in the imperfectly packed regions separating perfectly packed regions [12,13]. Liniger and Raj found that packing should be random to maximize final density and minimize final defect size. An additional important result is that differential densification between poorly packed and well-packed regions lead to the desintering of particle-particle necks, as predicted by the calculation for the row of sintering spheres. In addition, differential densification and desintering were found to be more important than asymmetrical neck growth in producing heterogeneous microstructure. The final result of this study is the suggestion that a *narrow but not mono-sized* particle size distribution provides the most homogeneous powder compact, the highest final density, and the lowest amount of sintering damage in the final sintered body.

As a result of the improvements in processing, primarily from the control of particle size and use of colloidal techniques, model uniform microstructures have now been fabricated in Al_2O_3 [16-19] ZrO_2 [20], Y_2O_3 [21,22], TiO_2[23,24], Si_3N_4 [25], and mullite [26,27]. In 1981, Rhodes' study of agglomerate effects on ZrO_2 sintering demonstrated that colloidal processing can be used to produce uniform, dense microstructures at low temperatures that show a resistance to discontinuous grain growth. A recent example is the use of colloidal processing of Al_2O_3 with a fine particle size (0.16 μm) and an extremely narrow particle size distribution to sinter Al_2O_3 to 99.5% of theoretical density at 1150°C [16,17].

The use of colloidal processing techniques for easily-sinterable materials, such as Al_2O_3 and TiO_2, creates microstructures which approach the simple geometrical models for sintering. With correct processing, microstructural parameters are representative of the microstructure at the scale of a few grains as well as the compact as a whole. These experimental developments permit a re-evaluation of 3-D sintering models based on uniform microstructures described by repeating unit cells [18,28-30]. The unit cell typically consists of a single grain of a space-filling geometry with pores along the boundary between grains. With these unit cell models, microstructure evolution during sintering is followed with the following features: competition between coarsening and densification and scaling laws for the sintering of a bimodal pore size distribution. The microstructural parameters needed experimentally to compare with the models are easily measurable parameters: density, average pore size, pore size distribution, grain size, grain size distribution, surface area, and so on.

There are many combinations of microstructural features that can be used to follow the competition between densification and coarsening, for example, pore size-grain size or surface area-boundary area [30,32-34]. The most reliably and easily measured are grain size and density. From plots of density versus grain size, changes in the slope of trajectories are due to changes in the ratio of coarsening rate to densification rate. These plots are of special utility because transitions between processes can be seen from changes in the slope for a given run and changes in microstructure with processing can be determined by comparing grain size at a different density [18,35]. For example, studies by Edelson and Glaeser and by Barringer showed that monosized TiO_2 follows the same density-grain size trajectory for the temperature range 1000° to 1160°C for a variety of processing conditions [23,24].

Systems which coarsen more than they densify have also been examined: TiO_2 in HCl [36], ZrO_2 in HCl [37], ZnO in H_2 [38], Fe_2O_3 [39]. Because each of these systems can be sintered close to theoretical density in air, the ratio of the coarsening rate to the densification rate can be varied by changes in atmosphere [40,41]. Studies of coarsening are important to our understanding of the generation of crack-like flaws by sintering. Specifically, coarsening processes maintain particle coordination without the generation of tensile stresses at particle contacts. When densification occurs, particles with lower coordination numbers will be under a tensile stress and these sintered necks will dedensify. If the necks sizes are increased by coarsening, dedensification and the generation of crack-like pores can be suppressed. These concepts have been demonstrated in studies of ZnO powders [42] and glass, alumina, and ZnO powders sintered to rigid substrates in which controlled amounts of coarsening at low temperature prior to high temperature densification led to denser final microstructures than with high temperature densification alone [43]. Grain growth during the intermediate stage of sintering has also been shown to increase homogeneity in pore size in a powder compact containing large pores by coalescence of smaller pores, while the larger pores grow less [44].

An additional refinement in sintering theory has been a consideration of how the free surface-grain boundary dihedral angle affects: the driving force for sintering [5,6,45], the breakup of cylindrical channels in the transition of intermediate to final stage sintering [46], the attachment of pores to grain boundaries during grain growth [47], and the transition to abnormal grain growth [48]. Using Kingery and Francois' model relating pore curvature, dihedral angle, and number of grains surrounding a pore [49], Lange suggested that grain growth may be necessary to lower the pore coordination for pore shrinkage to be possible thermodynamically. While that concept is valid, calculations by Zhao and Harmer [29] and by Evans and Hsueh [50] indicate that the sintering kinetics for large pores are so slow that even when a large pore can shrink thermodynamically, grain growth is ineffective in promoting densification. Other dihedral angle effects on sintering are discussed in more detail elsewhere [51]. These new models incorporating dihedral angle effects are especially timely since measurements of the free surface-grain boundary dihedral angle demonstrate that the average dihedral angle in undoped Al_2O_3, MgO-doped Al_2O_3, and MgO polycrystals is in the range 106° - 117°, not 150° as previously measured [52-53] Measurements of dihedral angle by Ikegami et al. show the same trends but the average values are slightly higher [54].

Our old workhorse, Al_2O_3, has been used to examine the effects of pore size, dopants, and liquid phases on pore-boundary separation and the orientation dependence of grain growth. Model experiments of a single crystal sapphire growing into a fine-grained matrix have been performed using sapphire crystals with c-axis, a-axis, and 60° off c-axis cuts in contact with dense polycrystalline samples [55-59]. The matrices examined are: with and without arrays of pores at the single crystal-matrix interface, with [55,59] and without [56-58] a silicate liquid, and with and without MgO. An important feature of some of these studies is the controlled etching of pore sizes and shapes in the sapphire surface using photolithographic techniques in order to measure accurately the effect of pore size and pore spacing on the conditions for pore-boundary separation [56-58]. The results include:

1. MgO doping to Al_2O_3 without a liquid appeared to increase D_s, thereby increasing pore mobility.

2. The pore spacing is a critical variable for breakaway with pores in undoped Al_2O_3 remaining attached to the growing sapphire (c-axis cut) for pore spacings less than 6 μm and for times up to 20 hrs.

3. In MgO-doped Al_2O_3, pore arrays moved with the growing interface at a faster velocity but pore-boundary separation occurred at an annealing time of 10 hrs, independent of pore spacing.

4. Without a liquid, c-axis sapphire grew into an MgO-matrix faster than into undoped Al_2O_3.

5. In the presence of a silicate liquid, c-axis sapphire grew more slowly than a-axis sapphire, with the difference in velocity between c-axis and a-axis increasing as the Ca to Si ratio increased. The authors suggested that this difference in velocity results from the process being interface controlled.

The latter notion of interface control conforms to Burke's suggestion that, since MgO is not found at grain boundaries in Al_2O_3 (but is so effective at suppressing breakaway grain growth) that the model for crystal growth on well-developed facets with steps and ledges and kinetics should be adopted for Al_2O_3 [60]. Thus, a very small amount of MgO at the steps/kinks could "poison" growth at special growth sites. However, the observation that MgO-additions increase the boundary mobility of c-axis sapphire without liquid or pores, summarized above, is in direct conflict with this notion. More work is required to address some of these discrepancies.

The effect of second phase particle pinning of grain boundaries during grain growth has been studied through experiments on Al_2O_3 with FeO particles [61], ZrO_2 with Al_2O_3 particles [62], and Y_2O_3 doped with La [63]. FeO and La-yttria phases appear to inhibit grain growth while Al_2O_3 particles in ZrO_2 have little effect on grain growth. A new evaluation of the Zener criteria for boundaries pinned by pores for various microstructures and theoretical formulations establishes the ranges over which different pinning equations are applicable [64].

It has become widely accepted that many ceramics earlier thought to be single phase bodies in fact contain liquids at the sintering temperature due to impurities in the powder or introduced during powder processing and sintering [65-71]. These liquids degrade the creep resistance at high temperatures and the uncontrolled amounts of liquid lead to wide variations in measured properties. For example, abnormal grain growth in undoped Al_2O_3[68] and Fe_2O_3 [65] was induced by unintentional silicate-based liquid phases. This has led to increased attention to the initial chemical powder composition and to control of contamination by clean-room processing [72-77]. In addition, organic inclusions introduced during processing may leave no chemical residue but may cause damage to the matrix during sintering or themselves comprise flaws after sintering that seriously degrade the mechanical properties at low temperatures.

Other recent theoretical studies have examined the kinetics and thermodynamics of particle rotation during sintering [78] and the contiguity of sintered structures [79]. Of particular interest from an engineering point of view are two studies on the non-destructive characterization of the progress of sintering using elastic property measurements [80] and SANS [81].

COMPOSITES

There is a natural link between sintering of single phase powders and composite sintering: any variability in the shape, particle size distribution, and degree of agglomeration in a powder may lead to inhomogeneous sintering resulting from heterogeneity stresses. Theoretical analyses have determined that inclusions with different densities than the matrix will retard the densification of the matrix by the creation of a hydrostatic tensile stress in the matrix of the order of 0.5 to 2 MPa [15,82-89]. For particulate composites, a rough estimate of the magnitude of the tensile stress is the volume fraction of the particles multiplied by the sintering stress, Σ. The magnitude of the heterogeneity stress was verified experimentally by Ostertag from the bending during sintering of Al_2O_3 compacts reinforced in an asymmetrical pattern with SiC fibers [90,91]. As determined both theoretically and experimentally, increases in the fraction of heterogeneities in the matrix or in the difference in initial density between heterogeneity and matrix lead to a increasing suppression of matrix sintering rate and lowering of the final density.

The number of different composite systems and experimental variables examined is impressive. Among the many studies of systems where the matrix and the dense inclusions are the same material are: dense MgO cylinders in MgO powder [92]; alumina agglomerates in alumina [93]; yttria agglomerates of various strengths in yttria powder [94]. Sintering of dissimilar materials has been examined in systems as diverse as SiC fibers, whiskers, or particulate in Al_2O_3 [95], Al_2O_3 agglomerates in TiO_2 [96], TiC-reinforced Al_2O_3 [97], BN-reinforced SiC [98], mullite produced by sol-gel processing reinforced with SiC whiskers [99-102], ZrO_2 particles in Al_2O_3 [103], B_4C-TiB_2 composites [104], and SiC-reinforced glass [105].

Most theoretical work has focused on identifying stress generation in the matrix resulting from the difference in densification between the matrix and the inclusion/agglomerate. The stress field generated by differential sintering around a spherical dense inclusion is composed of a tensile hoop stress and a radial compressive stress, with a tensile mean stress [82]. The magnitude of the stress depends on the relative rates of creep and matrix densification, and microstructural variables, such as the volume fraction and size of the inclusions. The creep rate is typically described in terms of a matrix viscosity which changes during densification [106- 113]. If the creep rate and densification rates are controlled by different mechanisms with different activation energies, the effect of dense inclusions may be changed by changing temperature. On the other hand, if same mechanism controls both creep and densification, then changes in temperature will produce no benefit.

In experiments on viscous matrices with dense inclusions, there appear to be three regimes of behavior as a function of inclusion volume fraction. At volume fractions ≤ 0.1, the densification rates of the composites can be described by a simple rule-of-mixtures. Only over a narrow range of inclusion volume fractions (between 0.1 and 0.12) are the results in agreement with the Scherer's theory for viscous sintering with rigid inclusions. However, for higher volume fractions, the densification rate deviates significantly from either of these models. In experiments on crystalline matrices with dense inclusions, the measured densification rates are significantly lower than predicted by theory over all ranges of inclusion volume fraction [86].

The explanation for this discrepancy between theory and experiment remains controversial. Scherer has argued that the stresses are of the same order as the sintering stress and cannot, therefore, explain the magnitude of the effect in polycrystals containing many heterogeneities/inclusions [111]. In addition, application of a hydrostatic pressure only slightly greater than the tensile hydrostatic stress is predicted to eliminate the effect of the inhomogeneities. However, retardation of matrix densification is observed for small volume fractions and for particles as small as the matrix particle size [86]. Bordia and Raj found that the application of a low quasi-hydrostatic pressure <10MPa would suppress damage formation in the matrix but does not restore the matrix densification rate to the rate without heterogeneities [114].

One plausible argument is that heterogeneities are imperfectly distributed so that heterogeneities form interconnected structures over short distances in the matrix. The percolation limit for a given particle shape and size distribution gives an estimate of the particle volume fraction when particles form a completely interconnected structure that cannot densify. For single-sized, spherical particles, the percolation limit is at a volume fraction of 0.16. At volume fractions smaller than the percolation limit, inhomogeneities will sinter together and, thereby, limit the density of matrix in the vicinity of the sintered heterogeneities. An additional explanation is that the powder packing density near a heterogeneity may be lower than in the matrix away from the inclusion and will, therefore, lead to a lower limiting density [45,84]. The magnitudes of these two effects must be calculated to assess their contributions to the observed suppression of matrix densification rate.

An alternate explanation proposed by Mataga is that the sintering in heterogeneous powder is not properly described by a linear, isotropic sintering model [115]. Mataga suggested that a non-linear material model may be required as a result of non-linear stress dependence on sintering rate, a creep threshold, or non-linear creep. He noted, however, that significant deviations from linear behavior are necessary to explain the experimental results. (Additional factors may be a change in the diffusion path due to the sintering stress [111] or a change in the coarsening/sintering trajectory in the presence of dense inclusions.)

In light of these theoretical and experimental results, Rahaman and Jeng have suggested practical guidelines for minimizing damage formation in composite systems [102]:

1. The packing in the matrix should be maximized.

2. The inclusions/agglomerates should be distributed *uniformly* not *randomly*, in the matrix to minimize inclusion/agglomerate interactions.

3. The optimum sinterability conditions for the unreinforced matrix should be used for sintering the reinforced composite.

4. If the powder is amorphous, the composite should be densified before crystallization occurs.

Of these four guidelines, (3) is the most provocative. What really is the proper sintering schedule for a composite as compared with the matrix without the reinforcing material? What is the effect of coarsening - to strengthen the necks before densification or to narrow the particle size distribution before densification and grain growth begin ? For materials that sinter easily under a variety of conditions, such as the classic model material Al_2O_3, the sintering heat treatment for composites may be very different from that which produces the highest final density of the matrix alone.

An alternative approach to preventing damage formation in composites is to allow the matrix to sinter to almost full density before it comes into contact with the fiber by creating a void space of controlled thickness around the inclusion. This void space can be produced by coating the dense inclusion with an organic which burns off before sintering. This approach also has the advantage that the bonding between the fiber and the matrix can be controlled by the initial gap thickness [106].

It should be noted that in the previous section, the systems chosen to examine stress generation in the matrix exhibit little or no intermediate phase formation between the matrix and the reinforcing materials. In many engineering situations the only possible materials for a specific application may react and it is the ceramic engineer's task to minimize the extent of reaction by careful, innovative processing.

An additional factor influencing the sinterability and final properties of composites is thermal expansion anisotropy when the same material is used for matrix and reinforcement and thermal expansion mismatch when the phases of the matrix and reinforcement are different. During heating of composites, neck formation begins at the same time that stresses develop. The stress generation during heating will then depend on the ratio of the creep rate required to relieve thermal expansion mismatch stresses and heterogeneity stresses to the densification rate.

LIQUID PHASE SINTERING

The progress in theory and experiment for solid state sintering summarized above has been matched by similar accomplishments in the field of liquid phase sintering. Before citing specific research topics, we would like to acknowledge the completion of a major work in liquid phase sintering: the book *Liquid Phase Sintering* by Randall M. German [116]. This textbook is an excellent general reference which is, as Prof. German states, truly materials-independent and appropriate for engineers and scientists with diverse technical backgrounds. We congratulate Prof. German on his accomplishment and recognize his significant contribution to the field.

The past five years have brought a better understanding of the processes occurring in the neck region where two solid particles are in contact with liquid, in assemblages of particles filled with liquid, and in the transient state when the liquid first becomes molten. The calculation of the equilibrium configuration of particles and liquid and the forces generated by a liquid meniscus was demonstrated by Heady and Cahn for liquid phase sintering of spherical and jagged particles [117,118]. The calculation is based on an energy minimization subject to certain conditions, such as volume conservation. Recent calculations by Park, Cho, and Yoon have used this approach to model the filling of isolated pores by liquid during liquid phase sintering [119]. Grains were assumed to maintain their equilibrium shape determined by the balance between the tendency of grains to become spherical ("sphering force") and the negative capillary pressure due to the liquid menisci. The filling of pores and contact flattening were found to depend on liquid volume fraction and grain size, thereby leading to greater pore filling as the grain size increases. This gradual pore filling as grain growth/coarsening proceeds explains the experimentally observed agglomerate formation during the early stages of liquid phase sintering. The thermodynamic criteria for sequential pore filling in different 2-D particle geometries were also examined by Shaw [120].

From Park, Cho, and Yoon, an additional result of special importance is that particles completely surrounded by liquid but having a vacuum-filled pore in the center of the liquid is an unstable equilibrium. An infinitesimal perturbation leads to filling of the spherical void. In contrast, if the pore is filled with an insoluble gas, the pore will reach a stable equilibrium size. This is contrary to the liquid phase sintering model previously derived by Kingery [121]. The observation of pores completely surrounded by liquid means that an entrapped gas is limiting the final density, and that removal of the gas by alternate processing techniques will allow the structure to achieve a higher density.

A major advancement in liquid phase sintering, as well as in high temperature materials properties, is the recognition that surface forces exist between two solid surfaces forming the neck region between two sintering particles. The surface forces have many sources, for example, electrostatic interactions, van der Waals attraction, or structural (steric) forces, and can lead to an equilibrium thickness of liquid separating the two solids. The measurement of surface forces between ceramic surfaces at room temperature is an active research area, made possible by the development of a technique for measurement of surface forces. For liquid phase sintering, the nature of these interactions will affect liquid redistribution as the volume fraction and/or grain size of the particle change and will, in many cases, determine the mechanical properties at high temperature.

Clarke has examined the equilibrium thickness of a thin intergranular where structure within the liquid determines the surface forces [122]. In a complementary experimental study by Greil and Weiss, the equilibrium thickness of thin liquid silicate layers in β-SiAlON was found to be constant for increases in the liquid volume fraction

from 2% to 10% [123]. In addition, structure in a thin intergranular liquid phase was detected in an anorthite-based liquid in Al_2O_3 [124].

In many of the theoretical treatments described above, equilibrium configurations are the endpoints of the calculations. In liquid phase sintering experiments, the creation of equilibrium configurations is preceded by solid state sintering, disintegration of the sintered skeleton as melting occurs, mixed fluid and particle flow, particle dilatation, rearrangement, and finally to disintegration of the individual particles [125]. Grains will grow by grain growth/Ostwald ripening and coalescence processes. Grain shape may also change due to facetting transitions and/or growth rate anisotropy in the presence of a liquid phase. The identification of each stage is important in relating changes in processing variables to changes in microstructure. Selected examples of these processes are presented below.

As with solid state sintering, the magnitude of the sintering stress that provides the driving force for liquid phase sintering is an important parameter in determining sinterability. The magnitude of the sintering stress has been calculated by De Jonghe and coworkers for liquid phase systems, as well as for solid-state systems, from the ratio of the densification rate at no load to the creep rate with an applied uniaxial load. In the MgO-Bi_2O_3 system, De Jonghe and Srikanth found that the sintering stress was a constant throughout densification [126]. The calculated stress was low - 0.08 MPa - corresponding to a meniscus radius of curvature of about 6 μm, a value much larger than the MgO particle size. The low value of the sintering stress was attributed to formation of agglomerates by the sequential pore filling as suggested by Shaw and by Park, Cho, and Yoon.

In the final stages of sintering, grain growth/coarsening/Ostwald ripening, discontinuous grain growth, and densification occur simultaneously. Three recent studies illustrate the effect of the liquid phase on discontinuous grain growth and pore coalescence. In a study of grain growth in TiO_2-rich $BaTiO_3$, Hennings, Janssen, and Reynen found that the grain size of abnormally growing grains decreases with increasing additions of TiO_2-enriched seed grains[127]. Also, the grain size increases with increasing TiO_2 content to maximum at 2 mol% excess TiO_2. As noted above, studies of sintering and grain growth in undoped Al_2O_3 and Fe_2O_3 revealed that discontinuous grain growth can originate from regions containing a calcium-alumino-silicate second phase [65,68]. These results suggest that discontinuous grain growth is accelerated by a non-uniform distribution of liquid phase. A study of normal grain growth and pore coalescence in the MgO-$CaMgSiO_4$ system demonstrated that the coalescence of gas-filled pores is controlled by the rate of grain growth/Ostwald ripening of the solid grains [128].

An important feature of many liquid phase sintering systems is the facetting and shape change of the solid particles when they come into contact with the liquid. For example, pronounced facetting has been observed in anorthite- Al_2O_3 [59, 129, 130] and in β'-sialons [131]. The same growth phenomena identified for crystal growth in systems with facetted liquid-solid interfaces are expected to operate in these liquid phase sintering systems [132]. Among these phenomena are: (1) growth on a facet can be limited by the nucleation of a stable ledge, also known as "2-D nucleation limited growth"; (2) growth and dissolution shapes are not expected to be the same; (3) screw dislocations and special twin boundaries can serve as nucleation sites for growth in slow growing directions.

EFFECTS OF APPLIED PRESSURE: HOT PRESSING, HIP'ING, AND SINTER-FORGING

The industrial use of applied pressure to densify a wide variety of difficult-to-sinter materials has increased over the last several years. This has coincided with a increase in modelling of the effects of applied pressure on sintering [133-140]. These models fall into two different types. There are models based on the visco-elastic response of the porous compact to the applied stress. The constitutive equations for the entire body over the whole range of deformation are specified and then the response is numerically calculated [133-137]. An alternative approach is to divide the densification up into different regimes, as shown in hot pressing or hot isostatic pressing (HIP'ing) maps [138-140]. Within a regime a single mechanism will dominate, and the dividing lines between regimes are where the rates of densification are equal. The conditions required to obtain a desired microstructure can be estimated from trajectories on maps. The results of both techniques are consistent and provide insight into the densification process and the observed shape changes during hot isostatic pressing (HIP'ing). For example, a densification front moves inward during HIP'ing as densification proceeds. The main reason for the development of this densification front is a nonuniform temperature distribution during heating. The hotter material near the outer edge will densify faster. The heat conduction through the dense outer region can further change the temperature distribution. Also the dense outer region can support some of the load and thus reduce the pressure on the porous interior. These effects can lead to very anisotropic shape changes during HIP'ing. To study the densification in a systematic manner, model experiments have been preformed by Kaysser and co- workers [125]. The deformation of a single, polycrystalline particle under an applied uniaxial load was studied. In this technique they were able to measure changes in the geometry during densification.

The effect of nonuniform stresses during sintering is not clear. The addition of a shear stress, or uniaxial stress to a compact during sintering has yielded results which suggest that the creep rate may be control the rate of densification. The applied stress increases the creep rate significantly, so that it is no longer rate-controlling [141,142]. This effect is of importance only when creep is the rate limiting process which, for ceramics, occurs in a very limited number of systems. A more pronounced effect of shear stresses is an enhancement of the rearrangement during sintering. Large processing defects can be broken down during shear deformation, but would be stable during cold isostatic pressing [143]. Such large defects can also be removed during HIP'ing if the material is in a regime where extensive plastic deformation can occur, either by diffusion of dislocation motion [144-146].

A wide variety of materials which are difficult to densify at atmospheric pressure have been successfully sintered with the application of moderate to high pressures [147-150]. HIP'ing has been used to great advantage for removing defects in sintered

metallic materials. It has been noted however, that near surface defects may increase in severity during post- sintering HIP'ing [151]. The development of HIP maps, and the underlying data base necessary for their use, has allowed the conditions to achieve high density to be estimated in advance of the experiment [152,153].

While experiments have shown the tremendous benefits of applied pressure on sintering, there are many limitations. The most severe is the bloating, or desintering problem associated with many HIP'ed or hot pressed materials. The bloating is due to two main effects. Oxidation of impurities which were incorporated during pressing produces a internal gas pressure which causes pore growth. This can be avoided by restricting use to inert environments, but this limits the usefulness of the materials. Another source of bloating is due to pores which remain in the material after pressing. These pores are due either to trapped residual gas or to thermodynamic stability of the pores as a result of the surface energy to boundary energy ratio [52,121]. While the applied pressure will reduce the size of such defects as compared to pressureless sintering, when the pressure is removed the defects are not in thermodynamic equilibrium and at elevated temperatures, they will grow until they are in equilibrium. This again limits the use temperature of a HIP'ed material. This effect implies that the minimum pressure possible should be used, and that the major benefit due to pressure will be an increase in the densification of large defects.

CASE STUDIES

Zirconia

Zirconia, one of the toughest ceramic materials, has mechanical properties which are dependent both on microstructure and chemistry. Additives are required to stabilize the tetragonal phase and give high toughness. Also, the grain size must be kept small to retain the metastable tetragonal phase at room temperature. For a detailed review of recent work in zirconia see Somiya et.al.[154]. Zirconia is a material which sinters well. Densities above 99% are achieved under a wide range of processing conditions and dopant concentrations. [1] Two important factors in determining the time and temperature required for densification are the starting powder particle size and the degree of powder agglomeration, as summarized below.

Ultrafine zirconia powders (10-20nm) forming 1-10 μm agglomerates can be produced by chemical precipitation [155,156] and these powders sinter to full density at 1400°C in 2 hrs. At the initial stage of sintering, density decreases with time [156] resulting from differential densification in the agglomerated powder. Density increases when grain growth begins. This coarsening at the initial stage of sintering is not disastrous in this system due to the extremely small grain size, even after grain growth. Rhodes [20] demonstrated that deagglomeration of ZrO_2 can reduce the time and temperature required to sinter a commercial power from 4 hours at 1500°C to 1 hour at 1100°C. An additional factor limiting final density is that gas evolution from residual organics used in washing the powders can cause bloating/desintering at higher

[1] One difficulty in interpreting the density data is the fact that the changes in the fraction of the different phases lead to changes in density without any change in porosity.

temperatures. Powders produced by electro-refining and grinding [157] have similar ultimate densities and properties as compared with chemically produced powders, but with somewhat reduced sintering rates. This allows a greater degree of control over the dimensional stability of the material.

Additions of Ce, Y, Ca, Mg, or Ti to stabilize the tetragonal phase do not reduce the sinterability of the powders [158-163] and, if Si is present as an impurity, may increase the densification by the formation of a silicate- based liquid phase. Also, the addition of 40% ZrO_2 to ZrC allowed the densification of the composite at 2000°C [164] if the green density was >55%.

Sinter forging of zirconia powders [165] determined that densification can occur by plastic flow at pressures and temperatures of 1400°C. Through hot forging of dense materials [146] it was found that fine- grained zirconia could be deformed but large grained zirconia could not. Diffusion control was thought to be limiting, probably due to the limited number of independent active slip systems. Thus for plasticity, diffusional accommodation is necessary and is only possible in fine-grained materials at the strain rates used. Sintering followed by HIP'ing has been used to remove large pores (30-40μm) and achieve full density at 1200°C [144], most likely due to plastic flow in addition to increased driving force for densification. It is necessary to achieve high density (>96%) before HIP'ing to prevent open pores from limiting the final density.

Dielectric ceramics

For production of dielectric ceramics by sintering, the critical issue is control of the microstructure. While many additives have been introduced to improve the electrical properties, recent work has focused on additives added to improve the sinterability and retard grain growth. Typically the additives promote the formation of a liquid phase and thus allow sintering to occur at low temperature [166-169], but may also work by reducing the vapor transport [170]. In the Pb-Mg-Nb-O system, avoidance of the pyrochlore phase is important, and the presence of liquid phases [171-173] controls not only the microstructure but also the phase content of the samples. With the formation of a liquid phase, the heating schedule becomes important: fast heating rates may lead to an inhomogeneous distribution of liquid phase [174].

Many dielectric materials have high vapor pressures at the sintering temperatures. This leads to weight loss and compositional changes during sintering. Some additives reduce the volatilization [175], but the problem is usually solved by adding an excess of the volatile components. Fast firing can reduce the problem as the material spends less time at temperature, and, therefore, has a finer grain size [176] than conventionally sintered PZT materials.

Different sintering atmospheres may also change the sintering behavior [177]. This can be for a variety of reasons. Often the coarsening rates can be reduced in specific atmospheres. In certain cases the phase relations may change as the atmosphere changes. Another possibility is that the defect concentrations change with atmosphere and thus the diffusion coefficients also change. All these effects are very system specific

and need to be examined for each new system. A knowledge of how specific effects influence sintering can be used to estimate the behavior from other measurements.

While high density is important, removal of all porosity is not as important to electronic properties as having a small grain size. The presence of a liquid phase can promote exaggerated grain growth in $BaTiO_3$ [69], as well as in alumina, discussed above, and in $Ba_2YCu_3O_{6+x}$. In ferroelectrics large grains are generally not desired due to domain migration within the grains. Also, for non-cubic materials, microcracking due to thermal expansion anisotropy is reduced at small grain sizes [178]. Some of this effect can be eliminated by texture development produced by hot pressing [179]. While hot pressing or hot forging lead to better microstructures, use of pressure sintering is precluded for most electronic applications.

ZnO Varistors

In ZnO varistors, the presence of a grain boundary phase controls the properties. The distribution of the intergranular phase is influenced by the composition, sintering temperature and atmosphere [180]. In pure ZnO, various additives have been shown to affect the relative rates of coarsening verses densification [181]. As discussed above, this may be advantageous in promoting neck growth to prevent cracking due to differential densification.

Ceramic superconductors

While there have been many studies of ceramic superconductors, few have systematically examined their sintering behavior. It is now clear that the formation of liquid phases at high temperature often controls the microstructure evolution [182]. More definitive sintering studies are difficult to perform because the liquidus is strongly dependent on composition and atmosphere [183-185]. Although a variety of techniques have been used to improve the properties of ceramic superconductors [186- 190] with differing degrees of success, microstructural control in these systems will require careful control of all the processing parameters.

Ferrites

In most applications for ferrites, the important properties are the magnetic properties which are limited by the microstructure. Small grain sizes and pore-free materials are generally desired. These features are controlled most often by controlling the atmosphere during sintering to both suppress volatilization [191] and to affect diffusion coefficients through changes in the defect chemistry [192-194]. For a review of the current state of processing of ferrites, see Wang [195]. The use of an acicular powder leads to a smaller grain-sized dense Ni-Zn ferrite than the use of conventional powders [196]. The sintering of ultrafine powders also resulted in Ni-Zn ferrite and Co ferrite [197] with submicron-sized grains. Reactive sintering of Zn ferrite was not at all useful [198] but rather produced microstructures worse that conventionally processed powders. The use of a low temperature melting phase (Bi_2O_3) was shown to yield optimum electrical and magnetic properties for the case of 1% additions to Li-Ti ferrites [199]. The properties declined for larger Bi_2O_3 additions.

Silicon Carbide and Silicon Nitride

The development of techniques for sintering of SiC and Si_3N_4 has been reviewed by Greskovich and Prochazka [200]. They give the sintering conditions for selected compositions, with an emphasis on describing the conditions which control densification. In both these technologically important materials, coarsening mechanisms compete with densification mechanisms. Achievement of high density requires suppression of the coarsening processes. A wide range of conditions for a variety of compositions have been examined by many other authors [201-217]. Effects of additives, oxygen content, homogeneity, precursor type and size, temperature and sintering atmosphere have been considered. While these materials cannot be sintered without additives at atmospheric pressure, materials with excellent properties can be obtained by careful selection of the initial powders, the additives and the sintering conditions. Again, the optimum sintering conditions depend on the desired properties of the sintered body [217,218].

Special techniques

In addition to pressureless sintering, hot pressing and HIP'ing, there are several other techniques which have been used to produce dense materials. Very high pressures have been used for sintering several difficult-to-densify materials. Self combustion sintering with an applied pressure of 3GPa has been used to densify TiC [219], diamond has been densified at 7.7GPa and 2000°C [220], and BN has been densified using shock compaction [221] with pressures estimated to be over 33GPa. These pressures are beyond the pressures normally obtained in commercial systems and will only be applicable to special systems. Microwave and RF plasma sintering has been successful for sintering a variety of materials, such as Al_2O_3 [222-224], Al_2O_3-ZrO_2 composites [225], ZrO_2 [226] and ferrites [227] in short times. Shock activation of powders before sintering has been shown to have beneficial effects on the densification of AlN [228] and Al_2O_3 [229]. Vapor phase transport can also contribute to enhanced densification when materials are sintered in a temperature gradient [230-232]. There is a net migration of the sample down the temperature gradient and material is deposited in the neck surface in the cold regions after leaving the particle surfaces in the hot region. Thermal cycling effects on densification are though to be due to temperature gradients in the sample while it is equilibrating [233].

Reactive sintering

The formation of composites by direct reaction of liquid metals [234,235] is a unique method for producing large components. Composites of ZrC and reinforcing ZrB_2 platelets have been produced with porosities less than 1% by reaction between liquid Zr metal and B_4C. A wide variety of ceramic materials have been sintered under conditions where a reaction is also taking place. In many cases the reaction aids the densification process, but in some cases the reaction is not desired and the conditions need to be manipulated to reduce the amount of reaction. B_4C- TiB_2 composites sintered with Fe additions resulted in dense (>97%), fine grained material

[236]. Fe formed a liquid phase which aided densification and excess TiB_2 inhibited grain growth. In the Al_2O_3-TiC system, the reaction produces CO_2 which reduces densification [97]. However, rapid heating minimized this effect by reducing the time spent in a temperature range where the reaction occurred, and dense materials were obtained. In reactive sintering of ZrC-ZrO_2 composites, the amount of excess ZrO_2 was found to be important in determining the density of the sintered material [237]. In the case of Cr_2O_3 with TiO_2 additions, the densification depended on the atmosphere, with little densification in air and increasing as Po_2 decreased [238]. It was felt that this was due to a change in the defect chemistry rather then suppression of Cr volatilization. The effect of H_2O on the sintering of MgO is not well understood [239]. Closed pores were observed to shrink while the open pores coarsened, indicating that H_2O may activate surface or vapor transport. In the $MgAl_2O_4$-SiO_2 system, the sintering mechanism changed with temperature [240]. At low temperatures, viscous flow of SiO_2 dominated until the formation of crystobalite and then diffusion controlled the densification. At higher temperatures the formation of cordierite caused an expansion of the sample, and the grains were spinel cores surrounded by cordierite. Dense Al_2TiO_5 can be formed by reactive sintering of Al_2O_3 and TiO_2 [96,241], but careful control of the sintering temperature was required.

Very porous mullite gels (44% dense) can be sintered to 97% density but the resulting structure consists of elongated grains of $3Al_2O_3$- 2SiO2 and fine grained Al_2O_3-$2SiO_2$ [101]. The structure of the gel may have an effect on the final microstructure produced [242]. Seeding of the gels to provide nucleation sites for the reaction proved effective in getting dense materials with a uniform grain size [243,244]. Seeding has also been effectively used for Al_2O_3 [244] and Al_2O_3-ZrO_2 composites [99].

SUMMARY

Significant advances in modelling of solid-state and liquid-phase sintering and grain growth have been made. The major driving force behind these advances has been the realization that fundamental thermodynamic concepts could be extended beyond what had been done for the two-sphere model. In particular, models of pore filling in multi-particle groups for liquid phase sintering and of the stability of a row of sintering spheres have provided new insight into the processes governing sintering. Improved powder processing has lead to the creation of closer-to-ideal microstructures with which to test theoretical predictions of models that assume uniform microstructures.

A major shift in research has been made to sintering in the presence of intentional and unintentional non-densifying inclusions. Modelling and experiment have examined the effects on the densification of a finer grained matrix by large particles (or agglomerates) of the matrix material and of dense particles, whiskers, or fibers of a different phase intended for reinforcement. Even for small volume fractions of inclusions, the matrix sinterability is seriously impeded. Strength-controlling defects can form in the matrix as a result of sintering in the presence of dense inclusions. Because of the severity of matrix damage during sintering, the analysis of damage formation during sintering and, in particular, the factors which inhibit crack formation are topics of wide interest. So far the theoretical estimates of the stresses produced by these heterogeneities do not seem to agree with experiment. However, there is a general recognition that application of constitutive laws is required for properly describing constrained sintering in single- and two-phase bodies.

For many composite systems, hot pressing may be required to produce high density materials. Unfortunately, applied pressure is not a panacea for composite systems: damage to high aspect ratio whiskers or fibers during pressure-sintering may degrade the mechanical properties of the composite and the applied pressure does not restore the sinterability to the level without inclusions. However, hot pressing and HIP'ing are viable techniques for producing ceramic parts. For example, a commercial cutting tool has been manufactured by hot pressing SiC whiskers in an Al_2O_3 matrix.

Of the recent research on hot pressing and HIP'ing, the generation of hot pressing and HIP'ing mechanism maps has the greatest impact on the use of pressure-sintering techniques in manufacturing. Although an extensive data base is required for the generating these maps, the data base is smaller than for the corresponding sintering maps/diagrams, since the number of mechanisms which dominate tends to be small when pressures are applied. These maps can also be used on-line in research and development to follow the densification process and to determine changes in processing conditions in real time.

When pressureless sintering, hot-pressing, and HIP'ing are not effective, or a special system presents unique opportunities, different techniques for processing should be used. The use of reactive sintering, shock activation, microwave sintering, self-combustion sintering and plasma sintering is of advantage only in the systems which allow the processing to exploit the special characteristics of these methods.

The case studies presented demonstrate the use of the fundamentals outlined in the beginning of the paper. Knowledge of the relationships between the observed microstructure and the processes which give rise to such microstructures has allowed the processing to be manipulated to achieve a specific microstructure. Without this understanding of the fundamentals of sintering, improvement of the properties of a specific material must occur by trial and error and in an incremental manner. Sintering has now progressed to the point where material development can be done more systematically to optimize properties.

ACKNOWLEDGEMENTS

The financial support of the U. S. Air Force Office of Scientific Research (Program Manager: Dr. Liselotte Schioler), the Max Planck Society, and the International Institute for the Science of Sintering are gratefully acknowledged.

REFERENCES

1. S. J. Bennison and B. R. Lawn, "Role of interfacial grain-bridging sliding friction in the crack-resistance and strength properties of non- transforming ceramics," submitted to Acta Metall.

2. H. K. Bowen, "Basic Research Needs on High-Temperature Ceramics for Energy Applications," Mat. Sci. Eng. 44 1-56 (1980).

3. H. E. Exner, "Neck Shape and Limiting GBD/SD Ratios in Solid State Sintering," Acta Metall. 35, 587-591 (1987).

4. W. S. Coblenz, J. M. Dynys, R. M. Cannon, and R. L. Coble, "Initial Stage Sintering Models: A Critical Assessment," in: *Sintering Processes*, ed. G. C. Kuczynski, Plenum Press, 1980.

5. W. C. Carter, R. M. Cannon ,"Sintering Microstructures: Instabilities and the Interdependence of Mass Transport Mechanisms," in: *Ceramic Transactions*, Vol. 7, Eds. C. A. Handwerker, J. E. Blendell, and W. A. Kaysser, American Ceramic Society, Westerville, Ohio, 1989, in press.

6. R. M. Cannon, W. C. Carter, "Interplay of Sintering Microstructures, Driving Forces, and Mass Transport Mechanisms," J. Amer. Ceram. Soc. 72 [8] 1550-1555 (1989).

7. K. R. Venkatachari, R. Raj, "Shear Deformation and Densification of Powder Compacts," 69 [6] 499-506 (1986).

8. M. N. Rahaman, L. C. De Jonghe, "Effect of Shear Stress on Sintering," J. Amer. Ceram. Soc. 69 [1] 53-58 (1986).

9. R. K. Bordia, *Sintering of Inhomogeneous or Constrained Powder Compacts: Modelling and Experiments*, Ph.D Thesis, Cornell University, Ithaca, NY, 1986.

10. T. Cheng, R. Raj, "Measurement of the Sintering Pressure in Ceramic Films," J. Amer. Ceram. Soc. 71, [4] 276-80 (1988).

11. L. C. DeJonghe, M. N. Rahaman, "Sintering stress of homogeneous and heterogeneous powder compacts," Acta Metall. 36 223-229 (1988).

12. E. G. Liniger, R. Raj, "Packing and Sintering of Two-Dimensional Structures Made from Bimodal Particle Size Distributions," J. Amer. Ceram. Soc. 70 [11] 843-849 (1987).

13. E. G. Liniger, "Spatial Variations in the Sintering Rate of Ordered and Disordered Particle Structures," J. Amer. Ceram. Soc. 71 [9] C-408- C-410 (1988).

14. M. W. Weiser, L. C. De Jonghe, " Rearrangement During Sintering in Two-Dimensional Arrays," J. Amer. Ceram. Soc. 69 [11] 822-26 (1986).

15. R. Raj, R. K. Bordia, "Sintering behavor of bi-modal powder compacts," Acta Metall. 32 1003-1020 (1984).

16. T.-S. Yeh, M. D. Sacks, "Effect of Particle Size Distribution on the Sintering of Alumina," J. Amer. Ceram. Soc. 71 [12] C-484-C-487 (1988).

17. T.-S. Yeh, M. D. Sacks, "Effect of Green Microstructure on Sintering of Alumina," in: *Ceramic Transactions*, Vol. 7, Eds. C. A. Handwerker, J. E. Blendell, and W. A. Kaysser, American Ceramic Society, Westerville, Ohio, 1989, in press.

18. M.A. Occhionero, J.W. Halloran, "The Influence of Green Density Upon Sintering," in: *Sintering and Heterogeneous Catalysis*, edited by G.C. Kuczynski, Albert E. Miller,, Gordon A. Sargent, Plenum Press (New York), Materials Science Research, Vol. 16.

19. C. P. Cameron, R. Raj, "Grain-Growth Transition During Sintering of Colloidally Prepared Alumina Powder Compacts," J. Amer. Ceram. Soc. 71 [12] 1031-35 (1988).

20. W.H. Rhodes, "Agglomerate and Particle Size Effects on Sintering Yttria-Stabilized Zirconia," J. Amer. Ceram. Soc. 64 [1] 19-22 (1981).

21. D. J. Sordelet, M. Akinc, "Sintering of Monosized, Spherical Yttria Powders," J. Amer. Ceram. Soc. 71 [12] 1148-53 (1988).

22. D. J. Sordelet, M. Akinc,"Sintering of Monosized, Spherical Y_2O_3 Powders," in: *Ceramic Transactions*, Vol. 7, Eds. C. A. Handwerker, J. E. Blendell, and W. A. Kaysser, American Ceramic Society, Westerville, Ohio, 1989, in press.

23. E. A. Barringer, H. K. Bowen, "Formation, Packing, and Sintering of Monodisperse TiO_2 Powders," J. Amer. Ceram. Soc. 65 [12] C-199-C-201 (1982).

24. L. H. Edelson, A. M. Glaeser, "Role of Particle Substructure in the Sintering of Monosized Titania," J. Amer. Ceram. Soc. 71 [4] 225-35 (1988).

25. T. M. Shaw, B. A. Pethica, "Preparation and Sintering of Homogeneous Silicon Nitride Green Compacts," J. Amer. Ceram. Soc. 69 [2] 88-93 (1986).

26. Y. Hirato, I. A. Aksay; "Colloidal Consolidation and Sintering Behavior of CVD-Processed Mullite Powders," Mat. Sci. Res. Vol. 21 *Ceramic Microstructures '86: Role of Interfaces* 611-621 (1988).

27. N. Otsuka,"Sintering of Monodisperse Particles, Seramikkusu, 22 473-8 (1987).

28. J. Zhao, M. P. Harmer, "Effect of Pore Distribution on Microstructure Development: II, Matrix Pores," J. Amer. Ceram. Soc. 71 [2] 113-20 (1988).

29. J. Zhao, M. P. Harmer, "Effect of Pore Distribution on Microstructure Development: II, First- and Second-Generation Pores," J. Amer. Ceram. Soc. 71 [7] 530-39 (1988).

30. T. Ikegami, "Microstructural Development during Intermediate- and Final-Stage Sintering," Acta Meta.. 35 667-675 (1987).

31. A. D. Rollett, D. J. Srolovitz, and M. P. Anderson,"Simulation and Theory of Abnormal Grain Growth-Anisotropic Grain Boundary Mobilities," in: *Ceramic Transactions*, Vol. 7, Eds. C. A. Handwerker, J. E. Blendell, and W. A. Kaysser, American Ceramic Society, Westerville, Ohio, 1989, in press.

32. N. J. Shaw, R. J. Brook, "Structure and Grain Coarseing During the Sintering of Alumina," J. Amer. Ceram. Soc. 69 107-110 (1986).

33. T. Yamaguchi, H. Kosha, "Sintering of Acicular Fe_2O_3 Powder," J. Amer. Ceram. Soc. 64 C-84 - C-85 (1981).

34. H. Kuno, M. Tsuchiya, Cumulative pore volume difference (CPVD) in the study of pore changes during compaction or sintering, Powder Technology, 52 187-92 (1987).

35. K. A. Berry, M. P. Harmer, "Effect of MgO Solute on Microstructure Development in Al_2O_3," J. Amer. Ceram. Soc. 69 [2] 143-49 (1986).

36. M. J. Readey, D. W. Readey, "Sintering TiO_2 in HCl Atmospheres," J. Amer. Ceram. Soc. 70, [12] C-358-C-361 (1987).

37. M. J. Readey, D. W. Readey, "Sintering of ZrO_2 in HCl Atmospheres," J. Amer. Ceram. Soc. 69 [7] 580-82 (1986).

38. T. Quadir, D. W. Readey, "Microstructure Development of Zinc Oxide in Hydrogen," J. Amer. Ceram. Soc. 72 [2] 297-302 (1989).

39. J. Lee, D.W. Readey, "Microstructure Development of Fe_2O_3 in HCl Vapor," in:*Sintering and Heterogeneous Catalysis*, edited by G.C. Kuczynski, Albert E. Miller, and Gordon A. Sargent, Plenum Press (New York), Materials Science Research, Vol. 16.

40. D.W. Readey, J. Lee and T. Quadir, "Vapor Transport and Sintering of Ceramics," in: *Sintering and Heterogeneous Catalysis*, edited by G.C. Kuczynski, Albert E. Miller, and Gordon A. Sargent, Plenum Press (New York), Materials Science Research, Vol. 16.

41. D. W. Readey ,"Vapor Transport and Sintering," in: *Ceramic Transactions*. Vol. 7, Eds. C. A. Handwerker, J. E. Blendell, and W. A. Kaysser, American Ceramic Society, Westerville, Ohio, 1989, in press.

42. L. C. DeJonghe, M. N. Rahaman, M.-Y. Chu, and R. J. Brook, "Effect of Heating Rate on Sintering and Coarsening," submitted to J. Amer. Ceram. Soc.

43. T. J. Garino, H. K. Bowen, "Deposition and Sintering of Particle Films on a Rigid Substrate," J. Amer. Ceram. Soc. 70 C315-C317 (1987).

44. L. C. De Jonghe, M. N. Rahaman, and M. Lin, "The Role of Powder Packing in Sintering," in : Ceramic Microstructures '86, Role of Interfaces, Ed. J. A. Pask and A. G. Evans, Plenum Press, New York, 1987, 447-454.

45. W. C. Carter, A. M. Glaeser, "The Morphological Stability of Continuous Intergranular Phases: Thermodynamic Considerations," Acta Metall. 35 237-45 (1987).

46. F.F. Lange, "Sinterability of Agglomerated Powders," J.Amer.Ceram.Soc. 67 83-89 (1984).

47. C. H. Hsueh, A. G. Evans, and R. L. Coble, "Microstructure development during final/intermediate stage sintering - I. Pore/Grain Boundary Separation," Acta Metall. 30 1269-1279 (1982).

48. A. D. Rollett, D. J. Srolovitz, and M. P. Anderson, "Simulation and theory of abnormal grain growth - anisotropic grain boundary energies and mobilities," Acta Metall. 37 [4] 1227-1240 (1989).

49. W. D. Kingery, B. Francois, "The sintering of crystalline oxides, I. Interactions between grain boundaries and pores," in: *Sintering and Related Phenomena*, Ed. G. C. Kuczynski, N. Hooten, and C. Gibbon, Gordon and Breach, NY (1967) 471-499.

50. A. G. Evans, C. H. Hsueh, "Behavior of Large Pores During Sintering and Hot Isostatic Pressing," J. Amer. Ceram. Soc. 69 [6] 444-48 (1986).

51. J. E. Blendell, C. A. Handwerker, "Effect of Chemical Composition on Sintering of Ceramics," J. Crystal Growth 75 138-160 (1986).

52. C. A. Handwerker, J. M. Dynys, R. M. Cannon, and R. L. Coble, "Dihedral Angles in MgO and Al_2O_3: Distributions from Surface Thermal Grooves," accepted by J. Amer. Ceram. Soc.

53. C. A. Handwerker, J. M. Dynys, R. M. Cannon, and R. L. Coble, "Metal Reference Line Technique for Obtaining Dihedral Angles from Surface Thermal Grooves," accepted by J. Amer. Ceram. Soc.

54. T. Ikegami, K. Kotani, "Some Roles of MgO and TiO_2 in Densification of a Sinterable Alumina," J. Amer. Ceram. Soc. 70 [12] 885-90 (1987).

55. Y. Finkelstein, S. M. Wiederhorn, B. J. Hockey, C. A. Handwerker, and J. E. Blendell ,"Migration of Sapphire Interfaces into Vitreous Bonded Aluminum Oxide", in: *Ceramic Transactions*, Vol. 7, Eds. C. A. Handwerker, J. E. Blendell, and W. A. Kaysser, American Ceramic Society, Westerville, Ohio, 1989, in press.

56. J. Rödel, A. M. Glaeser,"Morphological Evolution of Pore Channels in Alumina", in: *Ceramic Transactions*, Vol. 7, Eds. C. A. Handwerker, J. E. Blendell, and W. A. Kaysser, American Ceramic Society, Westerville, Ohio, 1989, in press.

57. J. Rödel, A. M. Glaeser,"Pore Drag in Alumina," in: Ceramic Transactions, Vol. 7, Eds. C. A. Handwerker, J. E. Blendell, and W. A. Kaysser, American Ceramic Society, Westerville, Ohio, 1989, in press.

58. J. W. Rödel, *Application of Controlled Interfacial Pore Structures to Pore Perturbation and Pore Drag in Alumina*, Ph.D thesis, University of California, Berkeley, 1988 (LBL Publication No. LBL-26211).

59. W. A. Kaysser, M. Sprissler, C. A. Handwerker, and J. E. Blendell, "Effect of a Liquid Phase on the Morphology of Grain Growth in Alumina," J. Amer. Ceram. Soc. 70 [5] 339-343 (1987).

60. J. E. Burke,"Control of Grain Boundary Mobility," in: *Ceramic Transactions*. Vol. 7, Eds. C. A. Handwerker, J. E. Blendell, and W. A. Kaysser, American Ceramic Society, Westerville, Ohio, 1989, in press.

61. J. Zhao, M. P. Harmer, "Sintering of Ultra-High-Purity Alumina Doped Simultaneously with MgO and FeO," J. Amer. Ceram. Soc. 70 [12] 860-66 (1987).

62. F. F. Lange, T. Yamaguchi, B. I. Davis, P. E. D. Morgan, "Effect of ZrO_2 Inclusions on the Sinterability of Al_2O_3," J. Amer. Ceram. Soc. 71 [6] 446-48 (1988).

63. W.H. Rhodes, "Controlled Transient Solid Second-Phase Sintering of Yttria," J. Amer.Cer. Soc. 64 [1] 13-19 (1981).

64. D. L. Olgaard, B. Evans, "Effect of Second-Phase Particles on Grain Growth in Calcite, J. Amer. Ceram. Soc. 69 [11] C-272-C-277 (1986).

65. P. K. Gallagher, D. W. Johnson, Jr., and F. Schrey, "Some Effects of the Source and Calcination of Iron Oxide on Its Sintering Behavior," Bull. Amer. Ceram. Soc. 55 [6] 589-593 (1976).

66. S. J. Bennison, M. P. Harmer, "Effect of MgO Solute on the Kinetics of Grain Growth in Al_2O_3," J. Amer. Ceram. Soc. 66 [5] C90-C92 (1983).

67. S. J. Bennison, M. P. Harmer, "Grain-Growth Kinetics for Alumina in the Absence of a Liquid Phase," J. Amer. Ceram. Soc. 68 [1] C22-C24 (1985).

68. C. A. Handwerker, P. A. Morris, R. L. Coble, "Effects of Chemical Inhomogeneities on Grain Growth and Microstructure in Al_2O_3," J. Amer. Ceram. Soc. 72 [1] 130-36 (1989).

69. M. H. Drofenik, "Grain Growth During Sintering of Donor-Doped $BaTiO_3$," J. Amer. Ceram. Soc. Vol. 69, 1986, [1] C-8-C-9.

70. D. F. K. Hennings, R. Janssen, P. J. L. Reynen, "Control of Liquid- Phase-Enhanced Discontinuous Grain Growth in Barium Titanate," J. Amer. Ceram. Soc. Vol. 70, 1987, [1] 23-27.

71. D. Kolar ,"Discontinuous Grain Growth in Multiphase Ceramics," in: Ceramic Transactions, Vol. 7, Eds. C. A. Handwerker, J. E. Blendell, and W. A. Kaysser, The American Ceramic Society, Westerville, Ohio, 1989, in press.

72. C. A. Handwerker, *Sintering and Grain Growth of MgO*, Sc.D Thesis, M.I.T., Cambridge MA, 1983.

73. P. A. Morris ,"Impurities in Ceramics: Processing and Effects on Properties," in: *Ceramic Transactions*, Vol. 7, Eds. C. A. Handwerker, J. E. Blendell, and W. A. Kaysser, American Ceramic Society, Westerville, Ohio, 1989, in press.

74. P. A. Morris, *High-Purity Al_2O_3: Processing and Grain Boundary Structures*, Ph.D Thesis, M.I.T., Cambridge MA, June 1986.

75. P. A. Morris, R. H. French, R. L. Coble, F. N. Tebbe, U. Chowdhry, "Clean-Room and CO_2-Laser Processing of Ultra High-Purity Al_2O_3," in *Defect Properties and Processing of High- Technology Nonmetallic Materials*, Ed. Y. Chen, 60, Materials Research Society, Pittsburgh, PA, 1986, p.79.

76. S. J. Bennison, *The Effect of MgO on the Sintering of High Purity Alumina*, Ph.D Thesis, Lehigh University, 1987.

77. J. E. Blendell, H. K. Bowen, and R. L. Coble, "High Purity Alumina by Controlled Precipitation from Aluminum Sulfate Solutions," Bull. Amer. Ceram. Soc. 63 797-804 (1984).

78. J. W. Cahn ,"Grain Rotation in Sintering: An Examination of Driving Force Arguments," in: *Ceramic Transactions*, Vol. 7, Eds. C. A. Handwerker, J. E. Blendell, and W. A. Kaysser, American Ceramic Society, Westerville, Ohio, 1989, in press.

79. S. Prochazka ,"Surface Area, Average Mean Curvature and Chemical Potential in Porous Bodies," in: *Ceramic Transactions*, Vol. 7, Eds. C. A. Handwerker, J. E. Blendell, and W. A. Kaysser, American Ceramic Society, Westerville, Ohio, 1989, in press.

80. D. J. Green, C. Nader, and R. Brezny, "The Elastic Behavior of Partially-Sintered Alumina," in: *Ceramic Transactions*, Vol. 7, Eds. C. A. Handwerker, J. E. Blendell. and W. A. Kaysser, American Ceramic Society, Westerville, Ohio, 1989, in press.,

81. K. G. Frase, K. Hardman-Rhyne, "Porosity in Spinel Compacts Using Small-Angle Neutron Scattering," J. Amer. Ceram. Soc. 71 [1] 1-6 (1988).

82. R. K. Bordia, R. Raj, "Sintering of TiO_2-Al_2O_3 Composites: A Model Experimental Investigation," J. Amer. Ceram. Soc. 71 302-310 (1988).

83. J. P. Smith, G. L. Messing, "Sintering of Bi-modally Distributed Alumina Powders," J. Amer. Ceram. Soc. 67 238-42 (1984).

84. B. Kellett, F. F. Lange, "Stresses Induced by Differential Sintering in Powder Compacts," J. Amer. Ceram. Soc. 67 369-71 (1984).

85. L. C. DeJonghe, M. N. Rahaman, and C. H. Hsueh, "Transient Stresses in Bimodal Compacts During Sintering," Acta Metall. 34 1467-71 (1986).

86. M. W. Weiser, L. C. De Jonghe, "Inclusion Size and Sintering of Composite Powders," J. Amer. Ceram. Soc. 71 C125-127 (1988).

87. R. K. Bordia, G. W. Scherer,"On Constrained Sintering - Parts I, II, and III," Acta Metall. 36 2393-2416 (1988).

88. L. C. DeJonghe, M. N. Rahaman, "Sintering stress of homogeneous and heterogeneous powder compacts," Acta Metall. 36 223-229 (1988).

89. M. N. Rahaman, L. C. De Jonghe, "Effect of Rigid Inclusions on Sintering," in: *Ceramic Transactions*, Vol. 1, Ed. G. L. Messing, E. R. Fuller, and H. Hausner, American Ceramic Society, Westerville, Ohio, 1988, 887-896.

90. C. P. Ostertag ,"Reduction in Sintering Damage of Fiber-Reinforced Composites," in: *Ceramic Transactions*, Vol. 7, Eds. C. A. Handwerker, J. E. Blendell, and W. A. Kaysser, American Ceramic Society, Westerville, Ohio, 1989, in press.

91. C. P. Ostertag, "Technique for Measuring Stresses Which Occur During Sintering of a Fiber-Reinforced Ceramic Composite," J. Amer. Ceram. Soc. 70 C355-C357 (1987).

92. C. P. Ostertag, P. G. Charalambides and A. G. Evans ,"Observations and Analysis of Sintering Damage," in: *Ceramic Transactions*, Vol. 7, Eds. C. A. Handwerker, J. E. Blendell, and W. A. Kaysser, American Ceramic Society, Westerville, Ohio, 1989, in press.

93. W. H. Tuan, E. Gilbert, and R. J. Brook, "Sintering of heterogeneous ceramic compacts," J. Mat. Sci. 24 1062-68 (1980).

94. M. Ciftcioglu, M. Akinc, and L. Burkhart, " Effect of Agglomerate Strength on Sintered Density for Yttria Powders Containing Agglomerates of Monosize Spheres," J. Amer. Ceram. Soc. 70 C329-C334 (1987).

95. T. N. Tiegs, P. F. Becher, "Sintered Al_2O_3-SiC-Whisker Composites," Bull. Amer. Ceram. Soc. 66 339-42 (1987).

96. S. Kamiya, H. K. Bowen; "Microstructural Control of Al_2O_3-TiO_2 Composites by Cyclic Annealing," in: *Ceramic Transactions*, Vol. 1, Ed. G. L. Messing, E. R. Fuller, and H. Hausner, American Ceramic Society, Westerville, Ohio, 1988, 978-985.

97. M. P. Borom, M. Lee, "Effect of Heating Rate on Densification of Alumina-Titanium Carbide Composites," Adv. Ceram. Mat. 1 335-40 (1986).

98. G. Valentine, A. N. Palazotto, R. Ruh, and D. C. Larsen, "Thermal Shock Resistance of SiC-BN Composites," Adv. Ceram. Mat. 1 81-87 (1986).

99. G. L. Messing, M. Kumagai, "Low Temperature Sintering of Seeded Sol-Gel-Derived, ZrO_2-Toughened Al_2O_3 Composites," J. Amer. Ceram. Soc. 72 40-44 (1989).

100. M. Ishitsuka, T. Sato, T. Endo, M. Shimada, "Sintering and Mechanical Properties of Yttria-Doped Tetragonal ZrO_2 Polycrystal/Mullite Composites," J. Amer. Ceram. Soc. 70 [11] C342-C346 (1987).

101. M. N. Rahaman, L. C. DeJonghe, S. L. Shinde, P. H. Tewari; "Sintering and Microstructure of Mullite Aerogels," J. Amer. Ceram. Soc. 71 [7] C338-C341 (1988).

102. M. N. Rahaman, D.-Y. Jeng, "Sintering of Mullite and Mullite- Matrix Composites," in: *Ceramic Transactions*, Vol. 7, Eds. C. A. Handwerker. J. E. Blendell, and W. A. Kaysser, American Ceramic Society, Westerville, Ohio, 1989, in press.

103. Y.L. Tian, D. L. Johnson, and M. E. Brodwin, "Microwave Sintering of Al_2O_3-ZrO_2 Composites," in: *Ceramic Transactions*, Vol. 1, Ed. G. L. Messing, E. R. Fuller, and H. Hausner, American Ceramic Society, Westerville, Ohio, 1988, 933-938.

104. D. K. Kim, C. H. Kim, "Pressureless Sintering and Microstructural Development of B_4C-TiB_2 Composites," Adv. Ceram. Mat. 3 52-55 (1988).

105. M. N. Rahaman, L. C. De Jonghe, "Effect of Rigid Inclusions on Sintering of Glass Powder Compacts," J. Amer. Ceram. Soc. 70 C348-C351 (1987).

106. C.-H. Hsueh, A. G. Evans, R. M. Cannon, and R. J. Brook, "Viscoelastic Stresses and Sintering Damage in Heterogeneous Powder Compacts," Acta Metall. 34 927-36 (1986).

107. R. K. Bordia, G. W. Scherer, "Sintering of Composites: A Critique of Available Analyses," in: *Ceramic Transactions*, Vol. 1, Ed. G. L. Messing, E. R. Fuller, and H. Hausner, American Ceramic Society, Westerville, Ohio, 1988, 872-886.

108. G. W. Scherer, "Viscous Sintering with a Pore-Size Distribution and Rigid Inclusions," J. Amer. Ceram. Soc. 71 [10] C447-C448 (1988).

109. G. W. Scherer, "Sintering of Rigid Inclusions," J. Amer. Ceram. Soc. 70 719-725 (1987).

110. C.-H. Hsueh, "Comment on "Sintering with Rigid Inclusions"," J. Amer. Ceram. Soc. 71 C314-C315 (1988).

111. G. W. Scherer, "Reply," J. Amer. Ceram. Soc. 71 C315-316 (1988).

112. C.-H. Hsueh, "Sintering of Whisker-Reinforced Ceramics and Glasses," J. Amer. Ceram. Soc. 71 C441-C444 (1988).

113. Kurt R. Mikeska, George W. Scherer, and Rajendra K. Bordia, "Constitutive Behavior of Sintering Materials," in: *Ceramic Transactions*, Vol. 7, Eds. C. A. Handwerker, J. E. Blendell, and W. A. Kaysser, American Ceramic Society, Westerville, Ohio, 1989, in press.

114. R. K. Bordia, R. Raj, "Hot Isostatic Pressing of Ceramic/Ceramic Composites at Pressures < 10MPa," Adv. Ceram. Mat. 3 122-26 (1988).

115. P. A. Mataga ,"Retardation of Sintering in Heterogeneous Powder Compacts," in: *Ceramic Transactions*, Vol. 7, Eds. C. A. Handwerker, J. E. Blendell, and W. A. Kaysser, American Ceramic Society, Westerville, Ohio, 1989, in press.

116. R. M. German, *Liquid Phase Sintering*, Plenum Press, New York, 1985.

117. R. B. Heady and J. W. Cahn, "An Analysis of Capillary Force in Liquid Phase Sintering," Met. Trans. 1 185 (1970).

118. J. W. Cahn and R. B. Heady, "Analysis of Capillary Force in Liquid Phase Sintering of Jagged Particles," J. Amer. Ceram. Soc. 53 [7] 406 (1970).

119. H. Park, S. Cho, and D. N. Yoon, "Pore Filling During Liquid Phase Sintering," Met. Trans. A. 15A 1075-80 (1984).

120. T. M. Shaw, "Liquid Redistribution during Liquid Phase Sintering," J. Amer. Ceram. Soc. 69 [1] 27-34 (1986).

121. W. D. Kingery, "Densification during Sintering in the Presence of a Liquid Phase: I. Theory," J. Appl. Phys. 30 [3] 301-306 (1959).

122. D. R. Clarke, "On the Equilibruim Thickness of Intergranular Glass Phases," J. Amer. Ceram. Soc. 70 [1] 15-22 (1987).

123. P. Greil, J. Weiss, "Evaluation of Microstructure of β-SiAlON Solid solution Materials Containing Different Amounts of Amorphous Grain Boundary Phase," J. Mat. Sci. 17 1571 (1982).

124. J. E. Marion, C. H. Hsueh, and A. G. Evans, "Liquid Phase Sintering of Ceramics," J. Amer. Ceram. Soc. 70 [10] 708-13 (1987).

125. W. A. Kaysser, "Sintering and HIP with a Liquid Phase,"in: Ceramic Transactions, Vol. 1, Ed. G. L. Messing, E. R. Fuller, and H. Hausner, The American Ceramic Society, Westerville, Ohio, 1988, 955-968.

126. L. C. DeJonghe, V. Srikanth, "Liquid-Phase Sintering of MgO-Bi_2O_3," J. Amer. Ceram. Soc. 71 [7] C356-C358 (1988).

127. D. F. K. Hennings, R. Janssen, P. J. L. Reynen, "Control of Liquid-Phase-Enhanced Discontinuous Grain Growth in Barium Titanate," J. Amer. Ceram. Soc. 70 [1] 23-27 (1987).

128. U.-C. Oh, Y.-S. Chung, D.-Y. Kim, and D. N. Yoon, "Effect of Grain Growth on Pore Coalescence During the Liquid-Phase Sintering of MgO-$CaMgSiO_4$ Systems," J. Amer. Ceram. Soc. 71 [10] 854-57 (1988).

129. P.L. Flaitz, J.A. Pask, "Penetration of Polycrystalline Alumina by Glass at High Temperatures," J. Amer. Ceram. Soc. 70, 449-455 (1987).

130. H. Song, R. L. Coble, Liquid Phase Sintered Al_2O_3: I, Origin and growth kinetics of plate-like abnormal grains and II, Morphology of plate-like abnormal grains, submitted to J. Amer. Ceram. Soc.

131. D.-D. Lee, S.-J. L. Kang, and D. N. Yoon, "Mechanism of Grain Growth and $\alpha - \beta'$ Transformation During Liquid-Phase Sintering of β'-Sialon," J. Amer. Ceram. Soc. 71 [9] 803-808 (1988).

132. For example, B. Lewis, "Nucleation and crystal growth," in: *Crystal Growth*, Ed. B. Pamplin, Pergamon Press, New York, 1975, pp. 12-39.

133. A. Nohara, T. Nakagawa, T. Soh, T. Shinke, "Numerical Simulation of the Densification Behaviour of Metal Powder During Hot Isostatic Pressing," Inter. J. Numer. Methods in Engineering 25 213-225 (1988).

134. M. Oyane, S. Shima, Y. Kono, "Theory of Plasticity for Porous Metals," Bull. JSME 16 [99] 1254-1262 (1973).

135. B. Aren, E. Navara, "Modelling Shape Change of Parts Produced by Hot Isostatic Pressing of Powders," Powder Metallurgy 31 [2] 101-105 (1988).

136. M. Abouaf, J. L. Chenot, G. Raisson, P. Bauduin, "Finite Element Simulation of Hot Isostatic Pressing of Metal Powders," Inter. J. Numer. Methods in Engineering 25 191-212 (1988).

137. J. Besson, M. Abouaf, "Numerical Simulation of Hot Isostatic Pressing of Ceramic Powders, International Conference on Hot Isostatic Pressing of Materials, Antwerp 25-27 April, 1988.

138. W-B. Li, M. F. Ashby, K. E. Easterling, "On Densification and Shape Change During Hot Isostatic Pressing," Acta Metall. 35 [12] 2831-2842 (1987).

139. W. Li, K. E. Easterling, "Stresses Developed in the Hot Isostatic Pressing of Metals and Ceramics," Holaniluiea Mechanical Report, 1287:48T, 1-21, 1987.

140. C. Brodhag, F. Thevenot, "Progress in Hot Pressing: Transitory Phenomena during Temperature Chenges," in: Ceramic Transactions, Vol. 1, Ed. G. L. Messing, E. R. Fuller, and H. Hausner, American Ceramic Society, Westerville, Ohio, 1988, 947-954.

141. M. M. Rahaman, L. C. De Jonghe, C. H. Hsueh, "Creep During Sintering of Porous Compacts," J. Amer. Ceram. Soc. 69 [1] 58-60 (1986).

142. M. Lin, M. N. Rahaman, L. C. DeJonghe, "Creep-Sintering and Microstructure Development of Heterogeneous MgO Compacts," J. Amer. Ceram. Soc. 70 [5] 360-366 (1987).

143. K. R. Venkatachari, R. Raj, "Enhancement of Strength through Sinter Forging" J. Amer. Ceram. Soc. 70 [7] 514-20 (1987).

144. A. P. Druschitz, "Processing Zirconia by Sintering/Hot Isostatic Pressing," Advanced Ceramic Materials, 3 [3] 254-56 (1988).

145. S. T. Lin, R. M. German, "Compressive Stress for Large-Pore Removal in Sintering," J. Amer. Ceram. Soc. 71 [10] C-432-C-433 (1988).

146. B. J. Kellett, F. F. Lange, "Hot Forging Characteristics of Fine Grained ZrO_2 and Al_2O_3/ZrO_2 Ceramics," J. Amer. Ceram. Soc. 69 [8] C-172-C-173 (1986).

147. T. Hattori, M. Yoshimura, S. Somiya, "High-Pressure Hot Isostatic Pressing of Synthetic Mica," J. Amer. Ceram. Soc. 69 [8] C-182-C-183 (1986).

148. B. K. Lograsso, D. A. Koss, "Densification of Titanium Powder During Hot Isostatic Pressing," Met. Trans. 19A 1767-1773 (1988).

149. James G. Schroth, Alan P. Druschitz,"Optimizing Unencapsulated Hot Isostatic Pressing of Al_2O_3," in: Ceramic Transactions, Vol. 7, Eds. C. A. Handwerker, J. E. Blendell, and W. A. Kaysser, American Ceramic Society, Westerville, Ohio, 1989, in press.

150. H. Schubert, W. A. Kaysser ,"HIPing of Alumina," in: Ceramic Transactions, Vol. 7, Eds. C. A. Handwerker, J. E. Blendell, and W. A. Kaysser, American Ceramic Society, Westerville, Ohio, 1989, in press.

151. B. J. Kellett, F. F. Lange, "Experiments on Pore Closure During Hot Isostatic Pressing and Forging," J. Amer. Ceram. Soc. 71 [1] 7-12 (1988).

152. A. S. Helle, K. E. Easterling, M. F. Ashby, "Hot-Isostatic Pressing Diagrams: New Developments," Acta Metall. 33 [12] 2163-2174 (1985).

153. S. Nair, J. K. Tien, "Densification Mechanism Maps for Hot Isostatic Pressing (HIP) of Unequal Sized Particles," Met. Trans. A, 18A (1987) 97-107.

154. *Science and Technology of Zirconia III*, Ed. S. Somiya, N. Yamamoto, H. Yanagida, (Advances in Ceramics, Vol 24), American Ceramic Society, Westerville, OH, 1988.

155. S. Somiya, M. Yoshimura, "Microstructure Development of Hydrothermal Powders and Ceramics," in: *Ceramic Microstructures '86 Role of Interfaces* (Materials Science Research), 21 464-475.

156. J.-M. Wu, C.-H. Wu, "Sintering Behavior of Highly Agglomerated Ultrafine Zirconia Powders," J. Mat. Sci. 23 3290-3299 (1988).

157. S. Blackburn, M. P. Hitchiner, C. R. Kerridge, "Green Density Characteristics and Densification Kinetics of PSZ Powders Produced by Electro-Refinning," in: Ceramic Transactions, Vol. 1, Ed. G. L. Messing, E. R. Fuller, and H. Hausner, American Ceramic Society, Westerville, Ohio, 1988, 864-865.

158. J.-G. Duh, H.-T. Dai, "Sintering, Microstructure, Hardness and Fracture Toughness Behavior of Y_2O_3-CeO_2-ZrO_2," J. Amer. Ceram. Soc. 71 [10] 813-19 (1988).

159. J.-G. Duh, H.-T. Dai, W.-Y. Hsu, "Synthesis and Sintering Behavior in CeO_2-ZrO_2 Ceramics," J. Mat. Sci. 23 2786-2791 (1988).

160. R. M. Dickerson, M. V. Swain, A. H. Heuer, "Microstructural Evolution in Ca-PSZ and the Room-Temperature Instability of Tetragonal ZrO_2," J. Amer. Ceram. Soc. 70 [4] 214-20 (1987).

161. C. L. Lin, D. Gan, P. Shen, "Stabilization of Zirconia Sintered with Titanium," J. Amer. Ceram. Soc. 71 [8] 624-29 (1988).

162. M. Ishitsuka, T. Sato, T. Endo, M. Shimada, "Sintering and Mechanical Properties of Yttria-Doped Tetragonal ZrO_2 Polycrystal/Mullite Composites," J. Amer. Ceram. Soc. 70 [11] C342-C346 (1987).

163. H.-Y. Lu, J.-S. Bow, "Effect of MgO Addition on the Microstructure Development of 3 mol% Y_2O_3-ZrO_2," J. Amer. Ceram. Soc. 72 [2] 228-31 (1989).

164. E. Min-Haga, W. D. Scott, "Sintering and Mechanical Properties of ZrC-ZrO_2 Composites," J. Mat. Sci. 23 2865-2870 (1988).

- 29 -

165. P. C. Panda, J. Wang, R. Raj, "Sinter-Forging Characteristics of Fine-Grained Zirconia," J. Amer. Ceram. Soc. 72 [12] C-507-C-509 (1988).

166. G. Zhilun, L. Longtu, G. Suhua, Z. Ziaowen, "Low Temperature Sintering of Lead-Based Piezoelectric Ceramics," J. Amer. Ceram. Soc. 72[3] 486-91 (1989).

167. J. P. Guha, H. U. Anderson, "Reaction During Sintering of Barium Titanate with Lithium Fluoride," J. Amer. Ceram. Soc. 69 [8] C193-C194 (1986).

168. G. M. Dynna, Y.-M. Chiang, "Mechanisms of Grain Growth Enhancement and Inhibition in Donor-Doped Barium Titanate," in: Ceramic Transactions, Vol. 7, Eds. C. A. Handwerker, J. E. Blendell, and W. A. Kaysser, American Ceramic Society, Westerville, Ohio, 1989, in press.

169. J.-S. Chen, R.-J. Young, T.-B. Wu, "Densification and Microstructural Development of $SrTiO_3$ sintered with V_2O_5," J. Amer. Ceram. Soc. 70 [10] C260-264 (1987).

170. V. L. Richards, "Agglomerate Size Effect on Sintering of Doped Lanthanum Chromite," in: Ceramic Transactions, Vol. 1, Ed. G. L. Messing, E. R. Fuller, and H. Hausner, American Ceramic Society, Westerville, Ohio, 1988, 897-898.

171. J. P. Guha, D. J. Hong, H. U. Anderson, "Effect of Excess PbO on the Sintering Characteristics and Dielectric Properties of $Pb(Mg_{1/3}Nb_{2/3})O_3$-Based Ceramics," J. Amer. Ceram. Soc. 71 [3] C152-C154 (1988).

172. J. P. Guha, H. U. Anderson, "Microstructural Inhomogeneity in Sintered $Pb(Mg_{1/3}Nb_{2/3})O_3$-$PbTiO_3$ Based Dielectrics," J. Amer. Ceram. Soc. 70 [3] C39-C40 (1987).

173. M. F. Yan, W. W. Rhodes, "Sintering, Microstructures and Dielectric Properties of $Pb(Mg_{1/3}Nb_{2/3})O_3$ Composition," in: Ceramic Transactions, Vol. 7, Eds. C. A. Handwerker, J. E. Blendell, and W. A. Kaysser, American Ceramic Society, Westerville, Ohio, 1989, in press.

174. Y.-S. Yoo, J.-J. Kim and D.-Yeon Kim, "Effect of Heating Rate on the Microstructural Evolution During Sintering of $BaTiO_3$ Ceramics," J. Amer. Ceram. Soc. 70 [11] C322-C324 (1987).

175. Z. S. Ahn, W. A. Schulze, "Conventionally Sintered $(Na_{0.5}, K_{0.5})NbO_3$ with Barium Additions," J. Amer. Ceram. Soc. 70 [1] C18-C21 (1987).

176. C. E. Baumgartner, "Fast Firing and Conventional Sintering of Lead Zirconate Titanate Ceramic," J. Amer. Ceram. Soc. 71 [7] C350-353 (1988).

177. B.-S. Chiou, S.-T. Lin, J.-G. Duh, "The Effect of Sintering Conditions on the Grain Growth of the $BaTiO_3$-Based GBBL Capacitors," J. Mat. Sci. 23 3889-3893 (1988).

178. P. Duran, J. F. F. Lozano, F. Capel, C. Moure, "Large Electromechanical Anisotropic Modified Lead Titanate Ceramics," Journal of Materials Science **23** 4463-4469. (1988).

- 30 -

179. T. Kimura, T. Yoshimoto, FN. Lida, Y. Fujita, T. Yamaguchi, "Mechanism of Grain Orientation During Hot-Pressing of Bismuth Titanate," J. Amer. Ceram. Sco. 72[1] 85-89 (1989).

180. J. P. Gambino, W. D. Kingery, G. E. Pike, L. M. Levinson, H. R. Phillipp, "Effect of Heat Treatments on the Wetting Behavior of Bismuth- Rich Intergranular Phases in ZnO:Bi:Co Varistors," J. Amer. Ceram. Soc. 72 [4] 642-45 (1989).

181. J. Kim, T. Kimura, T. Yamaguchi, "Sintering of Sb_2O_3-doped ZnO," J. Mat. Sci. **24** (1989) 213-219 (1989).

182. J.E. Blendell, J.S. Wallace, M.J. Hill, "Effect of Po_2 on Microstructure of $Ba_2YCu_3O_{6+x}$," submitted to J. Am Ceram. Soc. 1989.

183. R.S. Roth, C.J. Rawn, F. Beech, J.D. Whitler, J.O. Anderson, "Phase Equilibria in the System Ba-Y-Cu-O-CO_2 in Air," Ceramics Superconductors II - Research Update, 243-251 (1988).

184. T. Aselage, K. Keefer, "Liquidus Relations in Y-Ba-Cu Oxides," J. Mat. Res. 3 [6] 1279-1291 (1988).

185. J.E. Ullman, R.W. McCallum, J.D. Verhoeven, "Effect of Atmosphere and Rare Earth on Liquidus Relations in RE-Ba-Cu Oxides," J. Mat. Res., 4 [4] 752-755 (1989).

186. K. Sadananda, A. K. Singh, M. A. Iman, M. Osofsky, V. Le Tourneau, L. E. Richards, "Effect of Hot Isostatic Pressing on $RBa_2Cu_3O_7$ Superconductors," Adv. Ceram. Mat. 3 [5] 524-26 (1988).

187. J. J. Rha, K. J. Yoon, S.-J. L. Kang, D. N. Yoon, "Rapid Calcination and Sintering of $YBa_2Cu_3O_x$ Superconductor Powder Mixture in Inert Atmosphere," J. Amer. Ceram. Soc. 71 [7] C328-C329 (1988).

188. P. Sarkar, T. B. Troczynski, K. J. Vaidya, P. S. Nicholson, "Reaction Sintering of $YBa_2Cu_3O_x$ in Different Oxygen partial Pressures," Ceramics Superconductors II - Research Update, 204-215 (1988).

189. J. S. Wallace, B. A. Bender, S. H. Lawrence, and D. J. Schrodt, "Reaction Sintering High-Density, Fine-Grained $Ba_2YCu_3O_{6.5+x}$ Superconductors Using $Ba(OH)_2H_2O$," Ceramics Superconductors II - Research Update, 243-251 (1988).

190. K. Sawano, A. Hayashi, T. Ando, T. Inuzuka, H. Kubo, "Processing of Superconducting Ceramics for High Critical Current Density," Ceramics Superconductors II - Research Update, 282-293 (1988).

191. P. Sainamthip, V. R. W. Amarakoon, "Role of Zinc Volatilization on the Microstructure Development of Manganese Zinc Ferrites," J. Amer. Ceram. Soc. 71 [8] 644-48 (1988).

192. J. T. Mullin, R. J. Willey, "Grain Growth of Ti-Substituted Mn-Zn Ferrites," Fourth International Conference on Ferrites Part 1 (Advances in Ceramics, Vol. 15), American Ceramic Society, Westerville, OH, 1985, 187- 191.

193. H. Rikukawa, I. Sasaki, "On the Sintering Atmosphere of Mn-Zn Ferrites," Fourth International Conference on Ferrites Part 1 (Advances in Ceramics, Vol. 15), American Ceramic Society, Westerville, OH, 1985, 215-219.

194. C. M. Srivastava, N. Venkataramani, R. Aiyar, "Studies on the Sintering Mechanism and on Texturization in the Hot-Pressed System (Mn, Zn, Fe)Fe_2O_4," Fourth International Conference on Ferrites Part 1 (Advances in Ceramics, Vol. 15), American Ceramic Society, Westerville, OH, 1985, 193-200.

195. *Fourth International Conference on Ferrites*, Ed. F.F.Y. Wang, Advances in Ceramics, Vol. 15, Amer. Ceramic Society, Westerville, OH, 1985.

196. K. Omatsu, T. Kumura, T. Yamaguchi, "Sintering of Acicular NiZn- Ferrite Powder," Ceramic Microstructures '86 - Role of Interfaces (Materials Science Research), 21 623-631 (1986).

197. S. Komarneni, E. Fregeau, E. Breval, R. Roy, "Hydrothermal Preparation of Ultrafine Ferrites and Their Sintering," J. Amer. Ceram. Soc. 71 [1] C26-C28 (1988).

198. F. J. C. M. Toolenaar, M. T. J. Verhees, "Reactive Sintering of Zinc Ferrite," J. Mat. Sci. **23** 856-861 (1988).

199. P. Kishan, D. R. Sagar, S. N. Chatterjee, J. K. Nagpaul, N. Kumar, K. K. Laroia, "Optimization of Bi_2O_3 Content and Its Role in Sintering of Lithium Ferrites," Fourth International Conference on Ferrites Part 1 (Advances in Ceramics Vol 15), Amer. Ceramic Society, Westerville, OH, 1985, 207-213.

200. C. Greskovich, S. Prochazka, "Selected Sintering Conditions for SiC and Si_3N_4 Ceramics," Ceramic Microstructures '86 - Role of Interfaces, Materials Science Research, 21 601-610 (1986).

201. T. M. Shaw, B. A. Pethica, "Preparation and Sintering of Homogeneous Silicon Nitride Green Compacts," J. Am Ceram. Soc. 69 [1] 88-93 (1986).

202. B. A. Bishop, M. S. Spotz, W. E. Rhine, H. K. Bowen, J. R. Fox, "Sintering of Silicon Carbide Prepared From a Polymeric Precursor," in: Ceramic Transactions, Vol. 1, Ed. G. L. Messing, E. R. Fuller, and H. Hausner, American Ceramic Society, Westerville, Ohio, 1988, 856-857.

203. William J. Hurley, Jr., Leonard V. Interrante, Roberto Garcia, and Robert H. Doremus ,"Sintering and Microstructural Studies of Nanosized Crystalline Si_3N_4 and Si_3N_4/AlN Powders Derived from Organometallic Precursors," in: Ceramic Transactions, Vol. 7, Eds. C. A. Handwerker, J. E. Blendell, and W. A. Kaysser, American Ceramic Society, Westerville, Ohio, 1989, in press.

204. O. J. Gregory, S.-B. Lee, R. C. Flagan, "Reaction Sintering of Submicrometer Silicon Powder," J. Amer. Ceram. Soc. 70 [3] C-52-C-55 (1987).

205. J. A. Palm, C. D. Greskovich, "Thermomechanical Properties of Hot- Pressed $Si_{2.9}Be_{0.1}N_{3.8}O_{0.2}$ Ceramic," Bull. Amer. Ceram. Soc. 59 [4] 447-452 (1980).

206. S. Bandyopadhyay, J. Mukerji, "Sintering and Properties of Sialons without Externally Added Liquid Phase," J. Amer. Ceram. Soc. 70 [10] C273- 277 (1987).

207. C. Greskovich, W. D. Pasco, G. D. Quinn, "Thermomechanical Properties of a New Composition of Sintered Si_3N_4," Bull. Amer. Ceram. Soc. 60 [9] 1165-1170 (1984).

208. W. A. Sanders, D. M. Mieskowski, "Strength and Microstructure of Si_3N_4 with ZrO_2 Additions," Adv. Ceram. Mat. 1 166-73 (1986).

209. M. H. Lewis, G. Leng-Ward, and C. Jasper, "Sintering Additive Chemistry in Controlling Microstructure and Properties of Nitride Ceramics,"in: Ceramic Transactions, Vol. 1, Ed. G. L. Messing, E. R. Fuller, and H. Hausner, The American Ceramic Society, Westerville, Ohio, 1988, 1019-1033.

210. P. K. Das, J. Mukerji, "Sintering Behavoir and Properties of Si_3N_4 Sintered with Nitrogen-Rich Liquid in the System Y_2O_3-AlN-SiO_2," Adv. Ceram. Mat. 3 [3] 238-43 (1988).

211. M. Omori, H. Takei, "Preparation of Pressureless-Sintered SiC- Y_2O_3-Al_2O_3," J. Mat. Sci. 23 3744-3749 (1988).

212. N. Hirosaki, A. Okada, K. Matoba, "Sintering of Si_3N_4 with the Addition of Rare-Earth Oxides," J. Amer. Ceram. Soc. 71 [3] C-144-C-147 (1988).

213. L. Cordrey, D. E. Niesz, and D. J. Shanefield ,"Sintering of Silicon Carbide with Rare-Earth Additions," in: Ceramic Transactions, Vol. 7, Eds. C. A. Handwerker, J. E. Blendell, and W. A. Kaysser, The American Ceramic Society, Westerville, Ohio, 1989, in press.

214. T. Takahashi ,"The Sintering Behavior of Y_2O_3-MgO-ZrO_2 Doped and Y_2O_3-Yb_2O_3 Doped Silicon Nitride," in: Ceramic Transactions, Vol. 7, Eds. C. A. Handwerker, J. E. Blendell, and W. A. Kaysser, American Ceramic Society, Westerville, Ohio, 1989, in press.

215. C. O'Meara, J. Sjoberg ,"The Development of Microstructure in Pressureless Sintered Si_2N_2O Bodies," in: Ceramic Transactions, Vol. 7, Eds. C. A. Handwerker, J. E. Blendell, and W. A. Kaysser, The American Ceramic Society, Westerville, Ohio, 1989, in press.

216. R. Jimbou, Y. Suzuki, R. Sugita, "Sintering of SiC-ZrB_2/AlN Heating Element by Hot-Pressing," in: Ceramic Transactions, Vol. 7, Eds. C. A. Handwerker, J. E. Blendell, and W. A. Kaysser, American Ceramic Society, Westerville, Ohio, 1989, in press.

217. W.A. Sanders, G. Baaklin, "Correlation of Processing and Sintering Variables with the Strength and Radiography of Silicon Nitride," Adv. Ceram. Mat. 3 [1] 88-94 (1988).

218. W.D. Carter, P.H. Holloway, C. White, R Clausing, "Boron Distribution in Sintered Silicon Carbide," Adv. Ceram. Mat. 3 [1] 62-65 (1988).

219. O. Yamada, Y. Miyamoto, M. Koizumi, "High-Pressure Self-Combustion Sintering of Titanium Carbide," J. Amer. Ceram. Soc. 70 [9] C-206-C-208 (1987).

220. M. Akaishi, S. Yamaoka, J. Tanaka, T. Ohsawa, O. Fukunaga, "Synthesis of Sintered Diamond with High Electrical Resistivity and Hardness," J. Amer. Ceram. Soc. 70 [10] C237-C239 (1987).

221. T. Akaishi, A. B. Sawaoka, "Dynamic Compaction of Cubic Boron Nitride Powders," J. Amer. Ceram. Soc. 69 [4] C-78-C-80 (1986).

222. M. A. Janney, H. D. Kimrey, "Microstructure Evolution in Microwave Sintered Alumina," in: Ceramic Transactions, Vol. 7, Eds. C. A. Handwerker. J. E. Blendell, and W. A. Kaysser, American Ceramic Society, Westerville, Ohio, 1989, in press.

223. M. A. Janney, H. D. Kimrey, "Microwave Sintering of Alumina at 28 GHz," in: Ceramic Transactions, Vol. 1, Ed. G. L. Messing, E. R. Fuller, and H. Hausner, American Ceramic Society, Westerville, Ohio, 1988, 919-924.

224. Y. L. Tian, H. S. Dewan, M. E. Brodwin, and D. Lynn Johnson, "Microwave Sintering Behavior of Alumina Ceramics," in: Ceramic Transactions, Vol. 7, Eds. C. A. Handwerker, J. E. Blendell, and W. A. Kaysser, American Ceramic Society, Westerville, Ohio, 1989, in press.

225. Y.L. Tian, D. L. Johnson, and M. E. Brodwin, "Microwave Sinteirng of Al_2O_3-ZrO_2 Composites," in: Ceramic Transactions, Vol. 1, Ed. G. L. Messing, E. R. Fuller, and H. Hausner, American Ceramic Society, Westerville, Ohio, 1988, 933-938.

226. J. Wilson, S. M. Kunz, "Microwave Sintering of Partially Stabilized Zirconia," J. Amer. Ceram. Soc. 71 [1] C40-C41 (1988).

227. F. Okada, S. Tashiro, M. Suzuki, "Microwave Sintering of Ferrites," Fourth International Conference on Ferrites Part 1, (Advances in Ceramics Vol 15), Amer. Ceramic Society, Westerville, OH, 1985, 201-205.

228. E. K. Beauchamp, M. J. Carr, R. A. Graham, "Hot-Pressing of Shock-Activated Aluminum Nitride," Advanced Ceramic Materials, 2 [1] 79-84 (1987).

229. R.F. Davis, Y. Horie, R.O. Scattergood, H. Palmore, III, "Defects Produced by Shock Conditioning: An Overview," Advances in Ceramics Vol 10, Structure and Properties of MgO and Al_2O_3 Ceramics, Ed. W.D. Kingery, American Ceramic Society, Westerville, OH, 1984.

230. D. Beruto, R. Botter, and A. W. Searcy, "The Influence of Thermal Cycling on Densification: Further Tests of a Theory," in: Ceramic Transactions, Vol. 1, Ed. G. L. Messing, E. R. Fuller, and H. Hausner, American Ceramic Society, Westerville, Ohio, 1988, 911-918.

231. D. Beruto, R. Botter, A. W. Searcy, "Influence of Temperature Gradients on Sintering: Experimental Tests of a Theory," J. Amer. Ceram. Soc. 72 [2] 232-35 (1989).

232. A. W. Searcy, "Theory for Sintering in Temperature Gradients: Role of Long-Range Mass Transport," J. Amer. Ceram. Soc. 70 [3] C61-C62 (1987).

233. D. Beruto, R. Botter, A. W. Searcy, "The Influence of Thermal Cycling on Densification: Further Tests of a Theory," in: Ceramic Transactions, Vol. 1, Ed. G. L. Messing, E. R. Fuller, and H. Hausner, American Ceramic Society, Westerville, Ohio, 1988, 911-912.

234. W. B. Johnson, T. D. Claar, G. H. Schiroky, "Preparation and Processing of Platelet Reinforced Ceramics by the Directed Reaction of Zirconium with Boron Carbide," to be published in in Ceramic Engineering and Science Proceedings; 9 [7-8] (1989).

235. T. D. Claar, W. B. Johnson, C. A. Andersson, G. H. Schiroky, "Microstructure and Properties of Platelet Reinforced Ceramics Formed by the Directed Reaction of Zirconium with Boron Carbide," to be published in: Ceramic Engineering and Science Proceedings, 9 [7-8] (1989).

236. D.K. Kim, C.H. Kim, "Pressureless Sintering and Microstructural Development of B_4C-TiB_2 Composites," Advanced Ceramic Materials, 3 [1] 52-55 (1988).

237. D. Barnier, F. Thevenot, "Fabrication of ZrC_xO_y and ZrC_xO_y-ZrO_2 Composite Ceramics," In: Ceramic Transactions: Ceramic Powder Science II, Vol. 1, Edited by Gary L. Messing and Edwin R. Fuller, American Ceramic Society, Westerville, OH, 1988.

238. H. Nagai, K. Ohbayashi, "Effect of TiO_2 on the Sintering and the Electrical Conductivity of Cr_2O_3," J. Amer. Soc. 72 [3] 400-03 (1989).

239. D. Beruto, R. Botter, "H_2O-Catalyzed Sintering of ≈2 nm-Cross-Section Particles of MgO," J. Amer. Ceram. Soc. 70 [3] 155-59 (1987).

240. R.J. Higgins, H.K. Bowen, "Preparation and Sintering Behavior of Fine-Grained $MgAl_2O_4$-SiO_2 Composites," Adv. in Ceram., Vol. 21, 691-98, 1987.

241. H. Okamura, E. A. Barringer, and H. K. Bowen, "Preparation and Sintering of Monosized Al_2O_3-TiO_2 Composite Powder," J. Amer. Ceram. Soc. 69 [2] (1986) C-22-C-24.

242. Y. Hirata, I.A. Aksay, "Colloidal Consolidation and Sintering Behavior of CVD-Processed Mullite Powders," In: Ceramic Microstructures '86: Role of Interfaces, Mat. Sci. Res. Vol. 21. Edited by J.A. Pask and A.G. Evans.

243. T.J. Mroz, Jr., J. W. Laughner, "Sintered Microstructures of Seeded Mullite Gels," in: Ceramic Transactions, Vol. 7, Eds. C. A. Handwerker, J. E. Blendell, and W. A. Kayser, American Ceramic Society, Westerville, Ohio, 1989, in press.

244. T. J. Mroz, Jr.,, J. W. Laughner, "Microstructures of Mullite Sintered from Seeded Sol-Gels," J. Amer. Ceram. Soc. 72[3] 508-509 (1989).

245. J. L. McArdle, G. L. Messing, "Seeding with γ-Alumina for Transformation and Microstructure Control in Boehmite-Derived α-Alumina, " J. Amer. Ceram. Soc. 69 [5] C-98-C-101 (1986).

JOURNAL DE PHYSIQUE
Colloque C5, supplément au n°10, Tome 49, octobre 1988

EQUILIBRIUM CRYSTAL SHAPES AND SURFACE PHASE DIAGRAMS AT SURFACES IN CERAMICS

C.A. HANDWERKER, M.D. VAUDIN and J.E. BLENDELL

Institute of Materials Science and Engineering, National Bureau of Standards, Gaithersburg, MD 20899, U.S.A.

Résumé — La forme d'équilibre d'un cristal est la forme qui minimise l'énergie libre total du cristal et peut contenir l'un des éléments suivants: des facettes, des côtés aigus, des surfaces courbes lisses, et des angles. Le relation entre l'énergie libre de surface par unité de surface, γ, et la forme d'équilibre du cristal est évidente d'après le diagramme de Wulff, diagramme polaire de γ en fonction des vecteurs normaux, $\hat{n}$. Cabrera, Cahn, Rottman et Wortis ont décrit les limites entre les surfaces du cristal à l'équilibre (par example, entre les plans adjacents de facettes) en tant que transitions de phase des surfaces. Si $\gamma(\hat{n})$ est fonction de la temperature, de la pression ou du potentiel chimique des composants, la forme d'équilibre du cristal peu changer. Ce changement de la forme d'équilibre peut être représenté par un diagramme de phase de surface avec les axes d'orientation de surface en fonction de l'orientation angulaire par rapport à une orientation arbitraire de référence, de la temperature, de la pression ou de la composition chimique. Les transitions de phase des surfaces de MgO a été determinée en fonction de la concentration de NiO en tant que soluté et le diagramme de phase des surfaces ont été construits.

Abstract — The equilibrium shape of a crystal is the shape which minimizes the total surface free energy of the crystal and may contain any or all of the following: facets, sharp edges, smoothly curved surfaces, and corners. The relationship between the surface free energy per unit area, γ, and the equilibrium crystal shape is seen straightforwardly from the Wulff plot, the polar plot of γ as a function of orientation of the normal vectors, $\hat{n}$. Cabrera, Cahn, and Rottman and Wortis have described the boundaries between surfaces on the equilibrium crystal (for example, between adjacent facet planes) as surface phase transitions. If $\gamma(\hat{n})$ changes with temperature, pressure, or chemical potentials of the components, the equilibrium shape of the crystal may change. This change in equilibrium shape can be represented by a surface phase diagram with axes of surface orientation, in terms of angle from an arbitrary orientation, and temperature, pressure, or chemical composition. The surface phase transitions of MgO have been determined as a function of NiO solute concentration and surface phase diagrams have been constructed.

This research is supported in part by the Office of Naval Research.

1. Background.

The character of interfaces in engineering materials is frequently the controlling factor in materials fabrication and performance. Due to increasing demands placed on materials in service, it is necessary to understand how these interfaces change in response to changes in processing variables, such as temperature, pressure, and chemical potential. From the time of Gibbs [1],

the general thermodynamic principles describing these changes have been known. However, the specific details of the structures and energies of surfaces and interfaces in real materials are required in order to use the surface thermodynamics in a predictive mode.

In this paper, we describe one approach we have taken in the study of how the relative energies and equilibrium morphologies of surfaces change with temperature and chemical potential. We present the results of an experimental study of equilibrium crystal shapes as a function of composition in the *MgO-NiO* system and use these results to construct equilibrium surface phase diagrams describing the transitions between crystal shapes.

2. Equilibrium crystal shapes.

The equilibrium shape of a crystal is the shape which minimizes the total surface free energy of the crystal. The relationship between the surface free energy per unit area, γ, and the equilibrium crystal shape is shown straightforwardly from the Wulff plot, the polar plot of γ as a function of orientation of the normal vectors, $\hat{n}$ |2|. The inner envelope of planes perpendicular to the vectors $\gamma(\hat{n})$ defines the equilibrium shape |3|. Although this construction is useful from a pedagogical point of view, in nature we observe the crystal shape, not the plot of $\gamma(\hat{n})$. However, by using the Wulff plot several important characteristics of equilibrium crystal shapes become clear: (1) The equilibrium shape is convex. (2) It may contain any or all of the following features: facets, sharp edges, smoothly curved surfaces, and corners. (3) By changing the relative values of γ for certain orientations, the equilibrium shape can change.

Cabrera, Cahn, and Rottman and Wortis |4-7| have described several convenient ways to view the equilibrium shape and its change with temperature. The transitions between adjacent crystal faces can be viewed as surface phase transitions. For example, at the intersection between two facet planes or at a nontangential intersection between a facet plane and a smoothly curved surface (Figure 1a and b), the surface energy changes discontinuously, corresponding to a first order transition. A second order transition occurs at the tangential intersection of a facet with a curved surface if the surface energy does not change discontinuously (Figure 1c). The smoothly curved (non-facetted) regions on the crystal shape are frequently referred to as being "rough". With these transitions defined in the same way we define bulk phase transitions, the change in the equilibrium shape with temperature, pressure, or chemical potential can be easily represented by a surface facetting transition diagram with axes relative top the crystal shape, in terms of angle from an arbitrary orientation, and the changing variable. The information which the surface facetting transition diagram contains is the orientation at which a transition occurs. The positions of first order transitions are indicated as dotted lines and second order transitions by solid lines, in accordance with the convention used by Rottman and Wortis, who calculated interface phase diagrams for cubic crystals as a function of temperature using statistical mechanics.

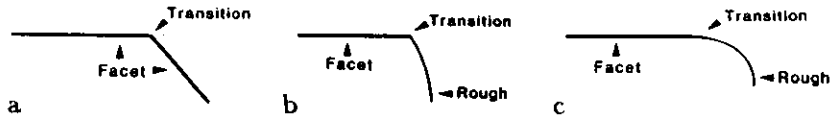

Figure 1. Schematics of surface phase transition. (a) and (b) are first order. (c) is second order.

A surface facetting phase diagram can then be constructed from the surface facetting transition diagrams and the crystal shapes. A surface facetting phase diagram shows the number of coexisting facet planes and rough surfaces as a function of the normal to the surface plane. This is directly analagous to a bulk phase diagram, with interface normal replacing composition and with facets corresponding to line compounds and rough surfaces on the equilibrium crystal shape corresponding to solid solutions. For example, when the equilibrium crystal shape is a cube, any surface whose normal is not normal to one of the six facets planes will decompose into a mixture of three {001} facets, except for surfaces with a ⟨100⟩ normal, which will decompose into two {001} facets. A surface facetting phase diagram for the cube will, thus, contain regions showing two-phase equilibrium and three-phase equilibrium. In this paper only the surface facetting transition diagram will be shown.

The change in the equilibrium shape of crystals with temperature is understood much better than with other variables. With increasing temperature, step energies decrease, facets shrink and a larger fraction of the area of the crystal becomes rough |8,9- |. With changes in chemical potentials, the change in the equilibrium shape depends on the details of adsorption and surface reconstructions.

While there have been several reports of changes in the equilibrium shape with annealing in different multi-component atmospheres |10,11- |, there have been few studies where a single variable other than temperature is changed systematically.

3. Experimental Procedures.

The system *MgO-NiO* forms an fcc solid solution at temperatures below the melting point of *NiO*, 1990°C. The equilibration studies were performed using *MgO-NiO* powder mixtures with *MgO:NiO* molar ratios of 100:0, 99:1, 95:5, 90:10, 80:20, 50:50, 40:60, 20:80, 10:90, 0:100. The background impurity concentrations of the *MgO* powder, determined by induction coupled plasma emission spectroscopy, were 750 Ba, 400 Ca, 80 Mn, 3540 Na, 450 Sr (μg/g *Mg* metal basis) and of the *NiO* powder, as provided by the manufacturer, were 6 Cu, 1 Ca, and 1 Si (μg/g *Ni* metal basis). The powders were mixed for two minutes in a vibratory mill, using plastic balls. The powders were placed in high purity Al_2O_3 or *Pt* crucibles and annealed at 1500°C for 55 h to homogenize the mixtures. The morphologies of the powder surfaces were examined by SEM.

4. Facetting Transitions and Surface Phase Diagrams.

The morphologies of the *MgO-NiO* powders are shown in Figure 2 and the corresponding 3-D equilibrium shapes and the projected views along the ⟨001⟩ and ⟨011⟩ zone axes are shown in Figure 3. Major changes in equilibrium shape occur with changes in the *Ni* concentration. The equilibrium shapes at low fractions of *Ni* (*MgO:NiO* = 100:0, 99:1, 99:5) are cuboidal with (100) facets and rough regions separating the (100) facets. The areas of the facets are large relative to the rough areas separating them. The intersections between the (100) facets and the rough regions appear to be continuous; the surface energy changes continuously where the facets and the rough areas join and the transition is second order. The second order transition is seen in the ⟨001⟩ zone axis (Figure 2(b)). The (90:10) powders show a minimum in the size of the (001) facets and the rough regions are almost spherical. For powders with higher *Ni* concentrations (80:20, 50:50, 40:60), the size of the (100) facets increases. The transitions between the (100) facets and the rough regions are clearly first order, as indicated in the SEM micrographs by the well-defined edge at the intersection. At higher concentrations of *Ni* (20:80, 10:90), (111) facets appear, the size of (100) facets decreases, and a rough region still exists separating facets. The intersections between the (111) and the (100) facets, between the (100) facets and the rough regions, and between the (111) facets and the rough regions are all first order. For pure *NiO* (0:100), the rough regions are

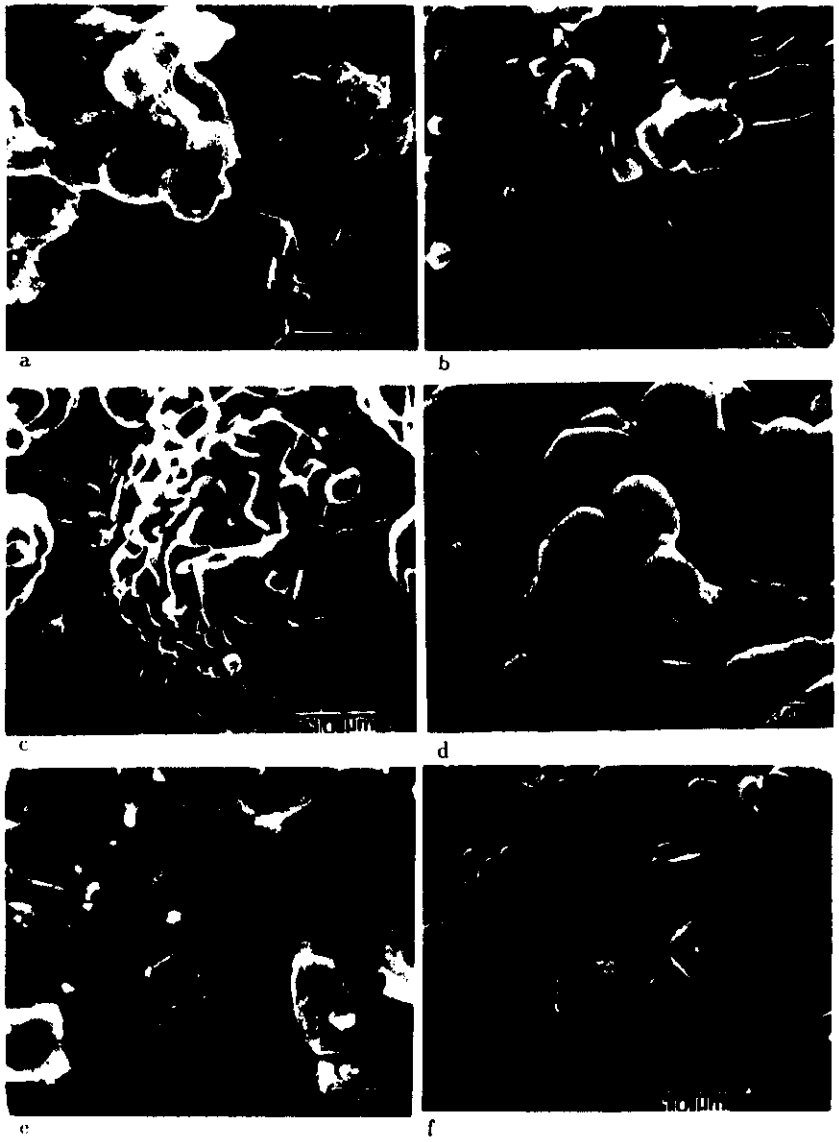

Figure 2. SEM micrographs of *MgO-NiO* powders annealed at 1500°C for 55 h: *MgO:NiO* (a) 100:1; (b) 99:1; (c) 95:5; (d) 90:10; (e) 80:20; (f) 50:50; (g) 40:60; (h) 20:80; (i) 10:90; and (j) 0:100.

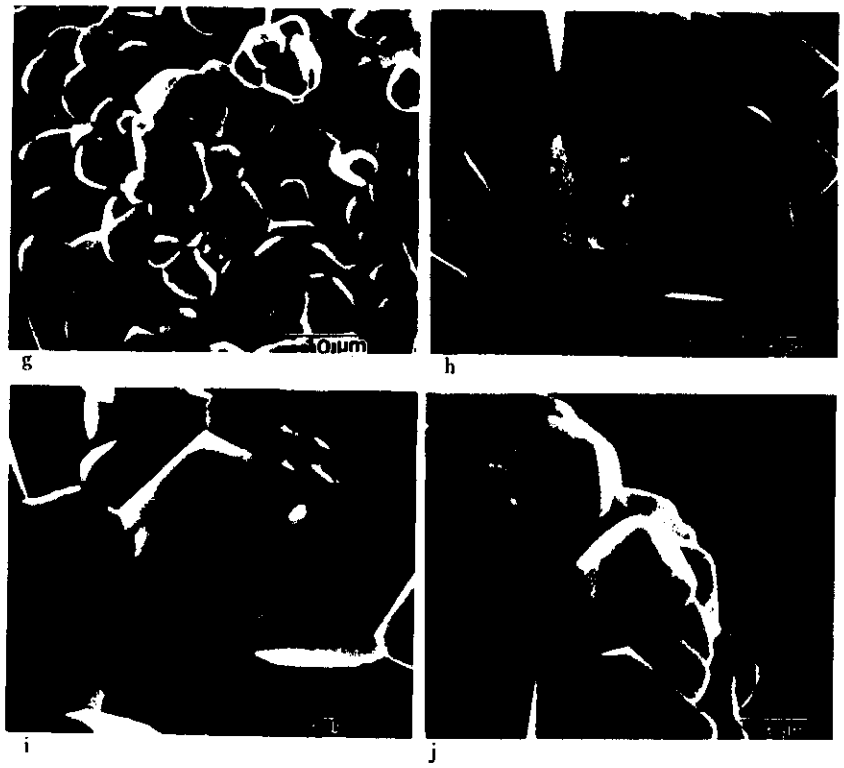

Figure 2. continued

very small and the relative areas of the (100) and the (111) facets have increased. In pure *NiO*, all of the intersections are also first order transitions.

The shapes and their transitions described above are plotted in the surface phase transition diagrams for the ⟨001⟩ and the ⟨011⟩ zone axes, Figure 4a and b. The upper parts of both curves show that, at low *Ni* concentrations, the size of the (001) facets decreases with increasing *Ni* concentration. The size of the (001) facets increases with *Ni* concentration for *Ni* concentrations greater than 10% (90:10). The appearance of (111) facets occurs between 60% and 80% *Ni*. There are no data between these two compositions to determine the exact composition where (111) facets first appear. The hypothetical construction on the diagram between these two compositions corresponds to the appearance of a (111) facet surrounded by rough regions, that is, all facet planes are separated by rough regions. For *Ni* concentrations greater than 80%, the (100) and the (111) facets intersect but small rough regions remain separating facets of the same type.

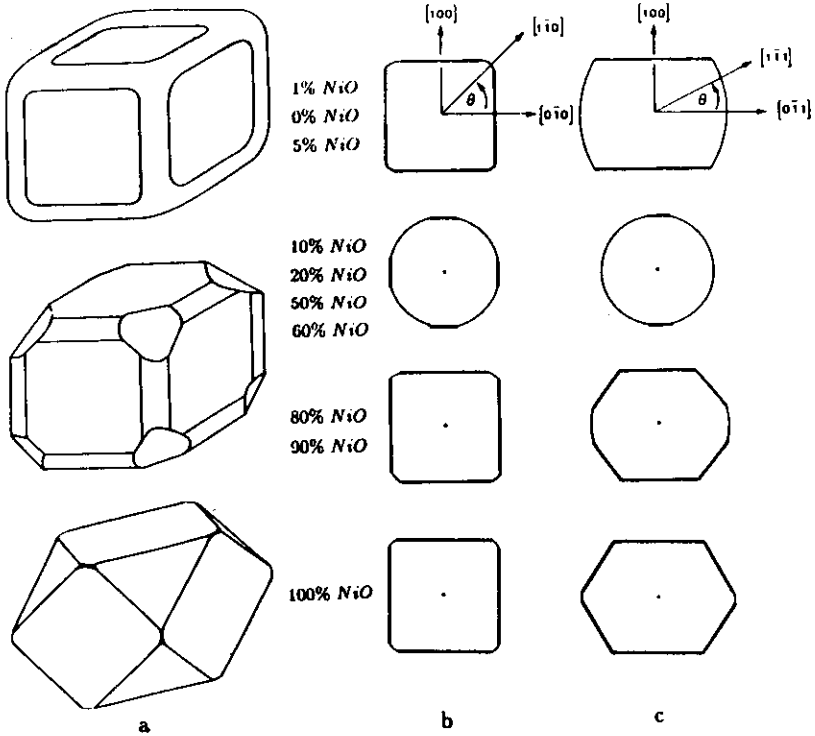

Figure 3. Equilibrium shapes shown in (a) 3-D views, (b) ⟨001⟩, and (c) ⟨011⟩ zone axes.

5. Summary.

The equilibrium crystal shapes and the surface phase diagrams for the *MgO-NiO* system at 1500°C in air have been determined. The equilibrium crystal shape changes with composition, indicating major changes in the Wulff plot, $\gamma(\hat{n})$. These results emphasize that interfaces which are initially stable may become unstable as the composition of the interface changes during processing and service. This effect is not limited to vapor-solid interfaces, as discussed here, but is applicable to all interfaces, including grain boundaries.

While reporting these equilibrium crystal shapes and phase transition diagrams for the *MgO-NiO* system, we warn the reader that the equilibrium shapes are extremely sensitive to the background impurity level. A wide variety of equilibrium shapes are found in undoped *MgO* derived from different sources. Cubes of *MgO* with sharp edges and corners are formed by burning *Mg* metal and by decomposition of magnesium hydroxychlorides in air; rough, unfacetted surfaces are formed on *MgO* powders by the decomposition of ultra-clean hydrated magnesium carbonate. In a continuation of this study, ultra-clean powder and clean room processing techniques are being used to limit sources of chemical contamination and to make it easier to identify how $\gamma(\hat{n})$ is changing with composition.

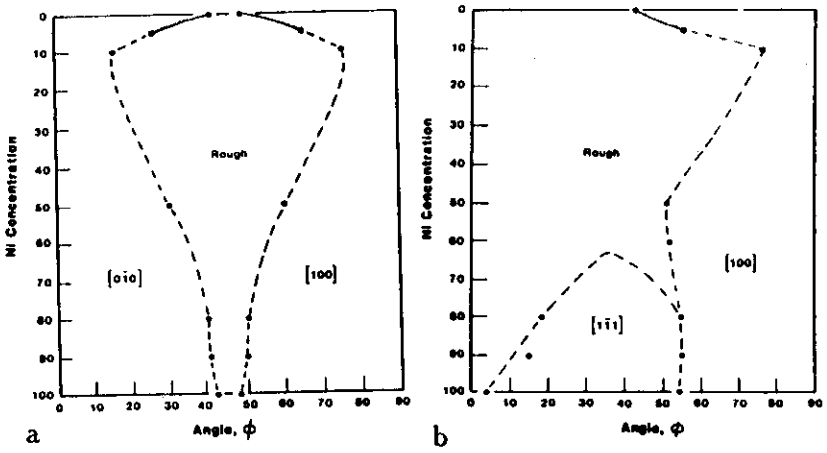

Figure 4. Surface facetting transition diagrams for *MgO-NiO*: (a) along the ⟨001⟩ zone axis (b) along the ⟨011⟩ zone axis.

References

[1] J. W. Gibbs, *The Collected Works of J. W. Gibbs* (Longmans, Green, New York, 1928).
[2] G. Wulff, *Z. Krystallogr. Mineral.*, 34, 499 (1901).
[3] C. Herring, *Phys. Rev.* 82, 87 (1951).
[4] N. Cabrera, *Symposium on Properties of Surfaces*, ASTM, Philadelphia, 1963.
[5] J. W. Cahn, *J. de Phys.*, 43, C6-199 (1982).
[6] C. Rottman and M. Wortis, *Phys. Rev. B* 29,328 (1984).
[7] C. Rottman and M. Wortis, *Physics Reports*, 103, Nos. 1-4, 59 (1984).
[8] T. Ohachi and I. Taniguchi, *J. Cryst. Growth*, 65, 84 (1983).
[9] R. J. Phaneuf and E. D. Williams, *Phys. Rev. Lett.*, 58, 2563 (1987).
[10] W. M. Robertson and P. G. Shewmon, *J. Chem. Phys.*, 39, 2330 (1963).
[11] Z. Y. Wang, M. P. Harmer, Y. T. Chou, *J. Amer. Ceram. Soc.*, 69, 735 (1986).

Reprinted from the Journal of the American Ceramic Society, Vol. 70, No. 5, May 1987

Effect of a Liquid Phase on the Morphology of Grain Growth in Alumina

WOLFGANG A. KAYSSER and MARIANNE SPRISSLER*

Max Planck Institut für Metallforschung, Institut für Werkstoffwissenschaften, 7000 Stuttgart 80, Federal Republic of Germany

CAROL A. HANDWERKER* and JOHN E. BLENDELL*

Institute for Materials Science and Engineering, National Bureau of Standards, Gaithersburg, Maryland 20899

In this investigation we have studied how the presence of a liquid phase affects the grain morphology and grain growth kinetics in Al_2O_3 at 1800°C using the growth of both matrix grains and large spherical single-crystal seeds growing into the matrix. The growth rates of the matrix grains were found to decrease in the following order: undoped Al_2O_3, Al_2O_3 with anorthite, Al_2O_3 with anorthite and MgO, and Al_2O_3 with MgO. Except for the samples doped with MgO alone, the matrix grains were faceted and appeared tabular in polished sections. In samples containing anorthite both with and without MgO, the single-crystal seeds exhibit basal facets with continuous liquid films and slow growth in the {0001} relative to all other crystallographic directions. When only MgO is added, the growth of the single-crystal seeds was not isotropic; however, no faceting was observed. We discuss how anisotropic growth rates caused by the anorthite additions can stimulate discontinuous grain growth in Al_2O_3.

I. Introduction

SMALL additions of MgO to Al_2O_3 have been shown to considerably reduce the grain growth rate,[1,2] to suppress discontinuous grain growth, and to allow sintering to theoretical density.[3] Determining exactly how MgO affects the sintering of Al_2O_3 has been a major research effort over the last two decades.

In order to analyze the sintering and grain growth of Al_2O_3 in a meaningful way, two important features which must be treated are the presence of an unintentional silica based liquid phase between the grains and the effect of this liquid on the grain morphology. In most sintering studies of Al_2O_3, it has been assumed that grain boundaries exist between all the grains in the microstructure. However, it is probable that most sintered Al_2O_3 prepared under typical laboratory conditions has been contaminated by the ubiquitous impurities, SiO_2 and CaO.[4-6] Because of the low solubility of SiO_2 in the lattice, SiO_2 will either be segregated to grain boundaries or, at some critical concentration, exist as a liquid phase. The location of this liquid phase in the microstructure depends on the local wetting conditions for grain boundaries and on the volume fraction of liquid phase.[7]

Since the microstructure of sintered Al_2O_3 was first published,[1] it has been obvious that the grains of undoped Al_2O_3 are anisotropic and faceted and the grains of MgO-doped Al_2O_3 are equiaxed. The anisotropy of the grains is particularly pronounced in the large grains growing during discontinuous grain growth in undoped Al_2O_3 and in Al_2O_3 with additions of MnO.[8] Any theory of microstructure evolution in Al_2O_3 must also address this question of why additions of MgO make Al_2O_3 more isotropic and why certain other additions are associated with the faceting of large grains.

In this investigation we have examined how a liquid phase (anorthite) affects the morphology of Al_2O_3 grains and have analyzed how morphological changes affect discontinuous grain growth. Grain growth in Al_2O_3 samples seeded with small single-crystal spheres was studied with small additions of MgO (0.1 wt%) and a liquid phase using hot-pressing at 1800°C. The liquid phase was obtained by additions of anorthite ($CaO \cdot Al_2O_3 \cdot 2SiO_2$), which forms a eutectic at 1550°C with 8 wt% Al_2O_3 in the quasi-binary section anorthite-Al_2O_3 of the CaO-Al_2O_3-SiO_2 system.[9] The addition of 1 wt% anorthite to Al_2O_3 produces approximately 1.8 vol% of liquid phase at 1800°C.[10] These experiments, where a known amount of liquid of a known composition was present, provide the limiting case for determining the influence of unintentional liquid phases on grain growth in Al_2O_3.

II. Experiments

Mixtures of Al_2O_3 powders and single-crystal spheres were prepared with different impurity additions by standard powder techniques and hot-pressing. The compositions were as follows: (1) undoped Al_2O_3, (2) Al_2O_3 with 0.1 wt% MgO, (3) Al_2O_3 with 1 wt% anorthite, and (4) Al_2O_3 with 0.9 wt% anorthite and 0.1 wt% MgO. $Mg(NO_3)_2 \cdot 6H_2O$ was added to mixtures of Al_2O_3 powder[†] (average particle size <0.3 μm) and single-crystal Al_2O_3 spheres[‡] (diameter, 500 μm; weight fraction, <0.01; Cr content, 0.01 wt%). Anorthite was produced by melting a mixture of Al_2O_3, CaO, and SiO_2 (1:1:2 mole ratio) at 1800°C for 20 min. The melt was cooled at 250 K/min. The anorthite glass was ground in a ball mill to produce powder with an average particle size of <1 μm. Mg was added as $Mg(NO_3)_2 \cdot 6H_2O$. The Al_2O_3 and the dopant powders were homogenized in the ratios listed above by stirring methanol powder mixtures and drying them at room temperature. The dried powders were calcined at 900°C for 1 h to convert the magnesium nitrate to the oxide and to remove adsorbed methanol.

All samples were isostatically compacted at 3 MPa. Samples were hot-pressed at 35 MPa, in carbon dies that had been lubricated with boron nitride, at 1800°C for 1 to 60 min, under a protective Ar atmosphere or under vacuum. The heating and cooling rates for the hot-pressing were 150 K/min. Samples were polished and then etched using hot H_3PO_4. The average intercept length of the grains was determined by lineal analysis.

III. Results

Figure 1 shows the microstructures of samples hot-pressed at 1800°C. The grains in the undoped samples are large, faceted, and appear tabular in 2D. The grain size and the grain shape in the MgO-doped sample are more uniform and the grain size is significantly smaller than in the undoped samples. With anorthite present both with and without MgO, the matrix grains are faceted and are much smaller than the matrix grains in the undoped Al_2O_3 samples. The matrix grains of Al_2O_3 with anorthite are larger than in the samples with both anorthite and MgO. Figure 2 shows the average intercept length, L_3, of undoped Al_2O_3 samples, Al_2O_3 with

Received April 28, 1986; revised copy received September 30, 1986; approved December 12, 1986.

Based in part on the thesis submitted by M. Sprissler for the Ph.D. degree, University of Stuttgart, Stuttgart, Federal Republic of Germany, 1981.

*Member, the American Ceramic Society.

†Now with Daimler Benz, Stuttgart, Federal Republic of Germany.

‡Ugine Kuhlmann, France; A6; nominal impurities (ppm): Mg, <3; Ca, <10; Fe, 20; Si, 50; Na 100.

§Frisch, West Germany.

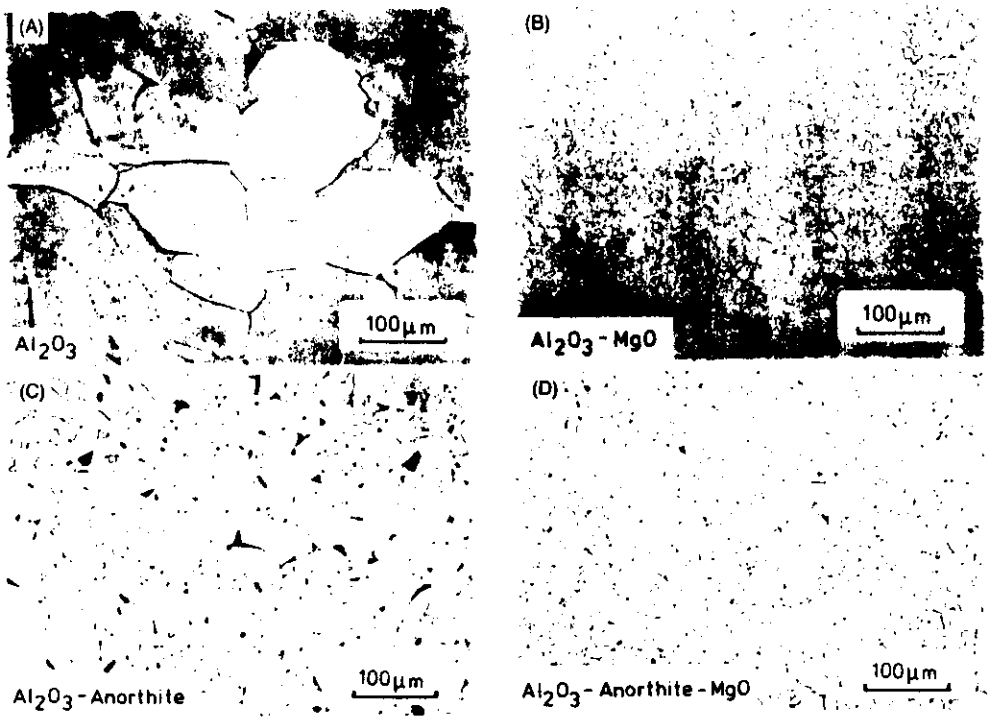

Fig. 1. Alumina matrix grains after hot-pressing (35 MPa) at 1800°C for 30 min: (*A*) undoped Al_2O_3, (*B*) Al_2O_3 + 0.1 wt% MgO, (*C*) Al_2O_3 + 1.0 wt% anorthite, (*D*) Al_2O_3 + 0.9 wt% anorthite + 0.1 wt% MgO.

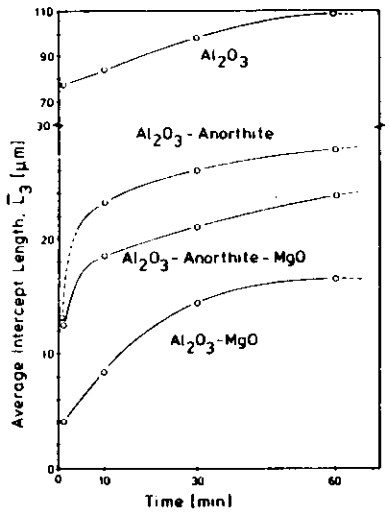

Fig. 2. Average linear intercept, L_3, of alumina matrix grains after hot-pressing (35 MPa) at 1800°C. Note change of scale for data for undoped Al_2O_3.

0.1 wt% MgO samples, Al_2O_3 with 1 wt% anorthite samples, and Al_2O_3 with 0.9 wt% anorthite and 0.1 wt% MgO samples hot-pressed at 35 MPa and 1800°C. L_3 is largest in the undoped Al_2O_3 samples and smallest in the samples containing MgO but without an intentional liquid phase.

The microstructures of samples which contain single-crystal Al_2O_3 spheres in a fine-grained matrix are shown in Fig. 3. In undoped Al_2O_3, the single-crystal seed has grown approximately the same amount as the large matrix grains and the large matrix grains have impinged on the seed crystal. Because the etchant only attacked some interfaces, all interfaces between the seeds and the matrix grains can be seen only when there are many grains intersecting the single-crystal seed. In undoped Al_2O_3 the number of matrix grains intersecting the seed crystals is small and, as a result, the dependence of growth rate on seed orientation could not be determined. When MgO alone is present, the growth of the seeds is comparatively uniform. Addition of anorthite leads to faceted growth in some directions and orientation-dependent, nonfaceted growth in other directions.

Density measurements by the Archimedes method gave 99.1% and 99.7% of theoretical density for undoped and MgO-doped Al_2O_3 samples, respectively. Samples containing anorthite were of high density with some small pores visible at triple junctions after polishing and etching. The large pores seen in the photographs of these samples are polishing artifacts or a result of chemical etching.

In all samples, small pores are visible near the initial boundary of the large single-crystal spheres. The porous interface was especially pronounced in the undoped Al_2O_3 samples. The ring of pores indicates grain boundary-pore separation during the early stage of hot-pressing.

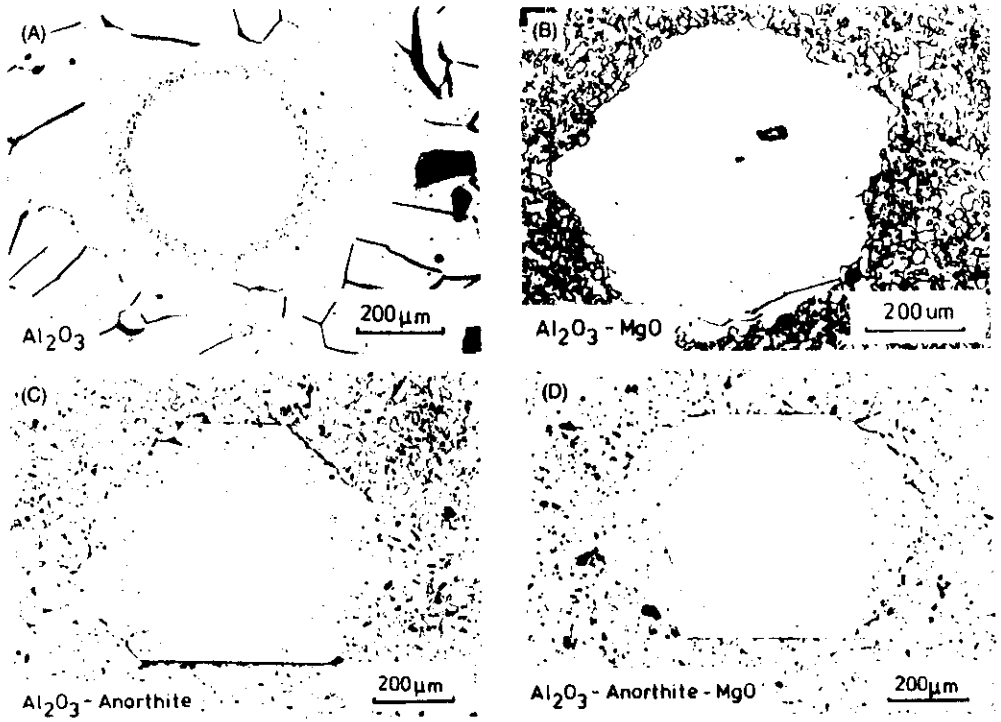

Fig. 3. Alumina with single-crystal seeds after hot-pressing (35 MPa) at 1800°C: (*A*) Al_2O_3, 60 min; (*B*) Al_2O_3 + 0.1 wt% MgO, 60 min; (*C*) Al_2O_3 + 1.0 wt% anorthite, 10 min; (*D*) Al_2O_3 + 0.9 wt% anorthite + 0.1 wt% MgO, 10 min.

IV. Discussion

(1) *Growth of Matrix Grains*

From Fig. 2, an initial, rapid grain growth regime followed by a much slower grain growth regime (hot-pressing times >10 min) can be deduced. The addition of anorthite, of anorthite with MgO, and of MgO dramatically lowers the grain growth rate compared with undoped Al_2O_3 during the two grain growth regimes. Equations of the form $G^3 - G_0^3 = k_3(t - t_0)$, where $G = 1.5L_3$, have been used to permit direct comparison of these results with other results from the literature. These are tabulated in Table I. The ranking of k_3 values is the same as the ranking of k_3 values at 1600°C reported previously for undoped Al_2O_3, Al_2O_3 with an unintentional liquid phase, Al_2O_3 with MgO and an unintentional liquid phase, and Al_2O_3 with MgO additions.[1,2]

These growth constants are considerably higher than growth constants reported earlier for grain growth in more porous Al_2O_3 and MgO-doped Al_2O_3 at 1800°C by Mocellin and Kingery[10] and by Kinoshita.[11] It was reported, however, that pores were present during these previous experiments. In both cases samples were first hot-pressed and subsequently annealed to cause grain growth.

Grain growth rates in Al_2O_3 samples with anorthite and MgO additions at the same levels used in this study have also been measured at 1600°[9] and 1700°C[12] as shown in Table I. The k_3 value for Al_2O_3 with 1 wt% anorthite at 1600°C is in good agreement with the k_3 value at 1600°C ($k_3 = 1.74 \times 10^{-19}$ m^3/s) of Bennison and Harmer[1] for undoped Al_2O_3 containing an unintentional liquid phase. Although the amount of impurities in that study was reported to be ≈0.02%, the matrix growth kinetics are the same as in the samples described here which contain a large amount of liquid phase.

Table I. Values of k_3 for Grain Growth in Al_2O_3

	k_3 ($\times 10^{-18}$ m^3/s)		
	1600°C*	1700°C*	1800°C†
Al_2O_3			980
Al_2O_3 + 1% anorthite	0.3	9.1	12.6
Al_2O_3 + 0.9% anorthite + 0.1% MgO	0.2	4.7	9.2
Al_2O_3 + 0.1% MgO			5.6

*Reference 12. †This study.

(2) *Seeded-Growth Kinetics*

The most striking result of the experiments on samples containing anorthite is the faceting observed as the single-crystal seeds grow into the fine-grained matrix, as shown in Figs. 3(*C*) and (*D*). The facets observed are basal facets as evidenced by the 2-fold nature of the growth front. Although the growth fronts away from the basal facets are nonfaceted, the growth rates in these directions are also functions of the crystallographic orientation, as seen in Figs. 3(*C*) and (*D*). The growth rate normal to the basal facets is much lower than the growth rate of the unfaceted regions. The difference in the growth rate of the two basal facets in Fig. 3(*C*) is due to the section not being through the center of the sphere. The

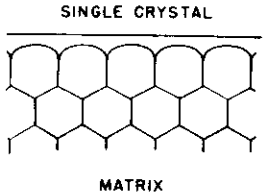

Fig. 4 Schematic microstructure of a basal facet separated from adjacent grains by a liquid layer.

measured diameter of the sphere from the photograph is 5% smaller than the true diameter of the sphere. The observed growth rates are an upper bound on the true growth rate, since sectioning through the center of the sphere at an angle, θ, to the normal to the facet will yield apparent growth rates too large by $\approx 1/\cos\theta$.

Monahan and Halloran performed a similar study of the growth of large sapphire single crystals into a fine-grained Al_2O_3.[13] Although the growth was not isotropic, faceting was not observed in spite of the probable presence of a liquid phase because of the high Si level (1000 ppm). Since they used c-axis sapphire rods[14] and sectioned nearly perpendicular to the rod axis, basal faceting could not have been observed.

The dihedral angles in the fine-grained matrix at the liquid-facet interface are most consistent with a continuous liquid film along the facet. This is shown schematically in Fig. 4. If we assume that the facet forms a grain boundary with the matrix grains, then a dihedral angle ψ of 180° at each triple junction implies one of two possibilities. First, if the torque terms are negligible, then each of the grain boundaries along the facet must have a much higher energy than those perpendicular to the facet, independent of the misorientation between any two matrix grains or a matrix grain and the facet. Second, if all grain boundary energies are comparable and the torque terms are important, then a precise balance of torques and energies must be present at each triple junction. As discussed in a paper by Kooy[15] on faceting during abnormal grain growth, it is unlikely that either of these two possibilities is met. It is more likely that there is a continuous liquid phase along the facet with grain boundaries of the matrix intersecting the liquid along the facet plane.

This basal faceting of the single-crystal seeds is not observed when MgO is present without anorthite (Fig. 3(*B*)). However, the growth rate into the equiaxed matrix grains is not isotropic. In the undoped Al_2O_3 discontinuous grain growth has occurred in the matrix and the single-crystal seeds appear to have had no distinct advantage for growth over the matrix grains. The grain size in the undoped Al_2O_3 samples is the same order of magnitude as the growth layer thickness of the single-crystal seeds and the matrix grains are tabular in 2D and are faceted. Because of the extensive discontinuous grain growth in the undoped Al_2O_3, it is very difficult to quantitatively compare the results for undoped Al_2O_3 with any of the other three sets of results. These results do show qualitatively that pronounced faceting of Al_2O_3 and extreme differences in the growth rate with orientation occur in undoped Al_2O_3 and in Al_2O_3 with anorthite, and Al_2O_3 with anorthite and MgO. No faceting occurs with only MgO added and the growth rate anisotropy is smaller. When anorthite liquid phase is present, the addition of 0.1 wt% MgO has no effect on the faceting behavior during seeded growth.

Continuous liquid films have been observed by TEM in commercial alumina[16] and alumina produced from commercial powders[17] which contain nominally 0.2% impurities and, hence, a small but significant amount of liquid phase. In those samples, almost all interfaces were wetted by the liquid phase. Faceting on $\{10\bar{1}2\}$, $\{0001\}$, and $\{11\bar{2}0\}$ were observed at grain surfaces in contact with the liquid. Interfaces between Al_2O_3 grains and the liquid phase were found to be similar to the one shown schematically in Fig. 4. The only interfaces that did not contain a liquid phase were basal twins, which are of very low energy. ψ was observed to be very close to 180° at twin-grain boundary intersections.

The observation of basal facets with slow growth rates and continuous liquid films can be used to give insight into the microstructural evolution of undoped Al_2O_3 and MgO-doped Al_2O_3. Samples of Al_2O_3 processed under typical laboratory conditions contain significant concentrations of CaO and SiO_2. Although the compositions of the undoped and MgO-doped Al_2O_3 were not measured in this study, random contamination frequently leads to concentrations of Si and Ca of the order of 1000 ppm. In this study it was shown that the kinetics of grain growth along the (0001) are lowered and basal facets form in the presence of a liquid phase. During the sintering of Al_2O_3 with a small amount of liquid phase, grain boundaries and nonbasal liquid-solid interfaces in Al_2O_3 can move rapidly while basal facets wetted by the liquid phase and twin boundaries are relatively immobile. A classical phenomenological description of the conditions for discontinuous grain growth[18] contains exactly these features: some boundaries are immobile and "pinned" while other boundaries are mobile. In this case, the difference in growth rate is due to the liquid film. The concept of a liquid phase affecting sintering and grain growth is not new. For example, Rossi and Burke[19] considered the effect of a liquid phase on the coarsening of pores during final-stage sintering in Al_2O_3.

The liquid phase need not be present initially to affect the microstructure development. Impurity segregation to grain boundaries can reduce the impurity concentration in the grains below the solubility limit, even though the total concentration is above the bulk solubility limit. As sintering and grain growth occur, the grain boundary area is reduced and the solute concentration in the grain boundary must increase to keep the concentration in the grains below the solubility limit. At some critical grain size the capacity of the grain boundary will be exceeded and a liquid phase will appear.

This scenario for the sudden appearance of a liquid phase is qualitatively supported in other studies of the microstructures of undoped Al_2O_3 at different stages of sintering.[20] At early stages the grains seem rather equiaxed. In the final stage of sintering grains become more faceted in general and the grains growing by discontinuous grain growth have pronounced facets. The correlation among faceted grains, discontinuous grain growth, and a CaO-Al_2O_3-SiO_2 phase also was previously reported by Handwerker *et al.*[21] for seeded and matrix grain growth experiments performed using high-purity Al_2O_3 processed under clean room conditions. In a single Al_2O_3 sample, random contamination produced discontinuously growing, faceted grains with an anorthite-based intergranular phase detected by EDS. It has been noted previously that the grain structure in undoped Al_2O_3 becomes more equiaxed when contamination during powder processing and sintering is reduced.[2,22] This correlation among faceting, the presence of an anorthite-based liquid phase, and discontinuous grain growth suggests that the samples of undoped Al_2O_3 examined in this study as well as in most other studies contained substantial amounts of liquid phase.

When MgO is added to Al_2O_3 without an intentional liquid phase, the growth of both the single-crystal seeds and the matrix grains becomes more isotropic. It is important to note that addition of MgO to Al_2O_3 powders with widely different nominal impurity levels creates the same result of a more equiaxed microstructure with no discontinuous grain growth. It is clear from this result that MgO is usually not the only active impurity in the system and that the combined effect of MgO, CaO, and SiO_2 additions must be considered.

V. Conclusions

The kinetics and the morphology of grain growth in undoped Al_2O_3, in Al_2O_3 with 1 wt% anorthite, in Al_2O_3 with 0.9 wt% anorthite and 0.1 wt% MgO, and in Al_2O_3 with 0.1 wt% MgO at 1800°C were determined for both matrix grains and large spherical single-crystal seeds growing into the matrix. In qualitative agreement with previous observations of Al_2O_3 with an uncontrolled amount of liquid phase, MgO lowered the matrix growth rate with and without anorthite present and a large amount of liquid phase without MgO also lowers the matrix grain growth. The growth rates of the matrix grains were found to decrease in the following order: undoped Al_2O_3, Al_2O_3 with anorthite, Al_2O_3 with anorthite and MgO, and Al_2O_3 with MgO. Except for the samples doped with MgO alone, the matrix grains were faceted and appeared tabular in 2D.

In samples containing anorthite both with and without MgO, single-crystal seeds exhibit basal facets with continuous liquid films and slow growth in the (0001) relative to all other crystallographic directions. When only MgO is added, the growth of the single-crystal seeds was not isotropic; however, no faceting was observed.

From the morphologies and the anisotropic growth rates observed in Al_2O_3 in the presence of an intentional liquid phase (1 to 2 vol%), the effect of a smaller amount of liquid phase on the microstructural evolution of Al_2O_3 has been described.

Acknowledgments: We are grateful to Professors G. Petzow, H. E. Exner, M. Mecartney, and R. L. Coble for interesting discussions.

References

[1]S. J. Bennison and M. P. Harmer, "Effect of MgO Solute on the Kinetics of Grain Growth in Al_2O_3," *J. Am. Ceram. Soc.*, **66** [5] C-90–C-92 (1983).
[2]S. J. Bennison and M. P. Harmer, "Grain-Growth Kinetics for Alumina in the Absence of a Liquid Phase," *J. Am. Ceram. Soc.*, **68** [1] C-22–C-24 (1985).
[3]R. L. Coble, "Sintering Crystalline Solids. II. Experimental Test of Diffusion Models in Powder Compacts," *J. Appl. Phys.*, **32** [5] 793–99 (1961).
[4]C. A. Handwerker, "Sintering and Grain Growth of MgO," Sc.D. Thesis, Massachusetts Institute of Technology, Cambridge, MA, 1983.
[5]P. A. Morris, R. H. French, R. L. Coble, F. N. Tebbe, and U. Chowdhry, "Clean Room and CO_2-Laser Processing of Ultra-High Purity Al_2O_3," Proceedings of a Symposium on Defect Properties and Processing of High Technology Nonmetallic Materials. Edited by Y. Chen, W. D. Kingery, and R. J. Stokes. MRS fall meeting, Boston, MA, 1985.
[6]J. E. Blendell, H. K. Bowen, and R. L. Coble, "High Purity Alumina by Controlled Precipitation from Aluminum Sulfate Solutions," *Bull. Am. Ceram. Soc.*, **63** [6] 797–802 (1984).
[7]T. M. Shaw, "Liquid Redistribution during Liquid Phase Sintering," *J. Am. Ceram. Soc.*, **69** [1] 27–33 (1986).
[8]L. B. Cutler, "Nucleation and Nuclei Growth in Sintered Alumina", pp. 320–27 in Kinetics of High Temperature Processes. Edited by W. D. Kingery. MIT Press, Cambridge, MA, 1959.
[9]E. M. Levin, C. R. Robbins, and H. F. McMurdie, Phase Diagrams for Ceramists, 1969 Supplement. Edited by M. K. Reser. American Ceramic Society, Columbus, OH, Fig. 2493.
[10]A. Mocellin and W. D. Kingery, "Microstructural Changes during Heat Treatment of Sintered Al_2O_3," *J. Am. Ceram. Soc.*, **56** [6] 309–14 (1973).
[11]M. Kinoshita, "Boundary Migration of Single Crystal in Polycrystalline Alumina," *Yogyo Kyokaishi*, **82** [5] 295–96 (1974).
[12]M. Spriissler, Ph.D. Thesis, University of Stuttgart, Stuttgart, Federal Republic of Germany, 1981.
[13]R. D. Monahan and J. W. Halloran, "Single Crystal Boundary Migration in Hot-Pressed Aluminum Oxide," *J. Am. Ceram. Soc.*, **62** [11–12] 564–67 (1979).
[14]J. W. Halloran, personal communication.
[15]C. Kooy, "Anisotropic Exaggerated Grain Growth and Sintering in $MnFe_2O_4$ and $Y_3Fe_5O_{12}$", pp. 21–34 in Science of Ceramics, Vol. 1. Edited by G. H. Stewart. Academic Press, New York, 1962.
[16]S. C. Hansen and D. S. Phillips, "Grain Boundary Microstructures in a Liquid Phase Sintered Alumina," *Philos. Mag. A.*, **47** [2] 209–34 (1983).
[17]M. P. Harmer, "Use of Solid-Solution Additives in Ceramic Processing", pp. 679–96 in Advances in Ceramics, Vol. 10, Structure and Properties of MgO and Al_2O_3 Ceramics. Edited by W. D. Kingery. American Ceramic Society, Columbus, OH, 1984.
[18]J. E. Burke, "Grain Growth"; in Ceramic Microstructures '66. Edited by R. M. Fulrath and J. A. Pask. Wiley-Interscience, New York, 1967.
[19]G. Rossi and J. E. Burke, "Influence of Additives on the Microstructure of Sintered Al_2O_3," *J. Am. Ceram. Soc.*, **56** [12] 654–59 (1973).
[20]R. E. Mistler, "Grain Boundary Diffusion, Widths and Migration Kinetics in Al_2O_3, NaCl and Ag", Sc.D. Thesis, Massachusetts Institute of Technology, Cambridge, MA, 1967.
[21]C. A. Handwerker, P. A. Morris, and R. L. Coble, "Grain Boundary-Pore Interactions in High-Purity Al_2O_3"; presented at the 86th Annual Meeting of the American Ceramic Society, Pittsburgh, PA, May 1, 1984 (Basic Science Division, Paper No. 122-B-84).
[22]W. S. Patrick and I. B. Cutler, "Grain Growth in Sintered Alumina," *J. Am. Ceram. Soc.*, **48** [10] 541–42 (1965).

Journal of Crystal Growth 75 (1986) 138–160
North-Holland, Amsterdam

EFFECT OF CHEMICAL COMPOSITION ON SINTERING OF CERAMICS

J.E. BLENDELL and C.A. HANDWERKER

Institute for Materials Science and Engineering, National Bureau of Standards, Gaithersburg, Maryland 20899, USA

Received 4 October 1985; manuscript received in final form 3 February 1986

Recent advances have been made in the understanding of sintering of ceramics. The primary advances have been in the modelling of grain boundary and surface properties and in the measurement of the effect of low levels of impurities and dopants on the energies and properties of interfaces. These results indicate that sintering is strongly affected by crystalline anisotropy, multiple transport mechanisms, complex geometries and impurity effects. In particular the effect of variable concentrations of impurities at the trace level have been found to mask the effects of changing most other systems parameters in ceramics with low intrinsic concentrations of defects. Experiments are described which can be used to isolate specific parameters or processes involved in sintering, such as the surface–grain boundary dihedral angle. Specific examples of impurity effects in MgO and α-Al_2O_3 are presented.

1. Introduction

Impurities and dopant additions can modify every kinetic and thermodynamic parameter which affects the way in which a ceramic material sinters. In many ceramic systems, the intrinsic concentrations of defects, such as lattice vacancies, is orders of magnitude smaller than the lowest concentration of impurities that has been obtained. As a result of the requirements of stoichiometry and electroneutrality, the incorporation of these impurities into the ceramic determines the defect concentration. Because sintering occurs by transport mechanisms involving these types of defects, the sinterability of a sample can depend on its concentration of impurities at the "trace" and "ultra-trace" levels. When chemical composition is not of critical importance, ceramic engineers can often search empirically, with varying success, for the "magic" additive that will make their material sinter. This approach is not appropriate to many applications.

It is not straightforward to identify the specific mechanisms by which impurities affect sintering. Impurities dissolved in the bulk can control lattice diffusion. Impurities segregated to the grain boundaries can change the energies and structures of grain boundaries, the grain boundary diffusivities, and the boundary mobilities. Segregation of impurity atoms to free surfaces can change the energies and structures of surfaces, the surface diffusivities, and the rates of evaporation and condensation from the surrounding vapor phase. The presence of impurities or dopants in excess of their solubility limits leads to precipitation in the bulk and along interfaces and can affect transport properties in their vicinities.

For many applications of sintered ceramic materials in the crystal growth and electronic industries, both the maintenance of a specific chemical composition and the ability to sinter the material to high density are critical to the end use. For example, α-Al_2O_3 for use as feedstock for Czochralski growth of sapphire must both contain low levels of impurities (Si, Fe, Na,...) and be sintered to high densities to maximize the amount of material that can be put into the crucible at the start of crystal growth. As a result of the concurrent restrictions on chemical composition and final sintered microstructure, it is important to understand the relationship between chemical composition and sinterability and to devise techniques for maintaining the composition while producing the required microstructure.

The effect of chemical composition on the sintering process is reviewed in this paper in the light of recent developments in the modelling of the sintering process and of grain boundary and surface properties and in the measurements of the effects of low levels of impurities on the energies and properties of boundaries in polycrystalline ceramics.

In section 2 we will review the current state of understanding of sintering theory. Section 3 will discuss how critical parameters for sintering are affected by impurities and dopants. Techniques for measuring the effect of impurities and dopants will be presented. Specific results will be presented for the measurement of the surface energy to grain boundary energy ratio and the implications of this result will be discussed. Examples using the Al_2O_3 and MgO systems have been used where possible. The production and sintering of ceramics with low levels of impurities is reviewed elsewhere [1,2].

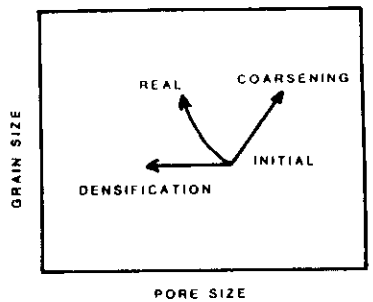

Fig. 1. Schematic of the grain size–pore size trajectories during sintering. For pure densification pores shrink, while for pure coarsening, both pores and grains grow. Real materials follow an intermediate path.

2. Sintering

When powder compacts are heated to high temperature (above $\approx 1/2$ the melting point), individual powder particles change their shape due to capillary forces [3]. The mechanisms by which these shape changes occur are usually described by the term "sintering" and, acting individually, lead either to densification or to coarsening of the powder compact as a whole [4–9]. During densification, the particle size remains constant, the surface area of the compact is reduced, and pore volume is eliminated. During coarsening, the particle size and the pore size increase and the surface area of the compact is reduced without a reduction in pore volume, as shown schematically in fig. 1. Both processes occur simultaneously during sintering but by different mechanisms. The process which dominates the sintering depends on the relative rates of the different mechanisms.

In this paper we will concentrate on the effect of impurities through the transport properties and changes in interfacial energies. The effects due to particle agglomeration, non-uniform particle packing, particle size distribution, non-spherical powders, and similar effects will not be considered. A discussion of some of these effects is presented elsewhere [10].

2.1. Models

For purposes of modelling, sintering is usually divided into three stages, initial, intermediate, and final [6]. During the initial stage the interparticle contact area (or neck size) increases from zero to $\approx 20\%$ of the cross-sectional area of the particle [11,12]. For the intermediate stage the grains are modelled as tetrakaidecahedra (truncated octahedra, which are space filling) with interconnected cylindrical pore channels at the grain edges. All pore channels are intersected by three grain boundaries. During this stage, the densification models predict that the pore channels simply shrink. In the final stage (beginning at approximately 92% of theoretical density) isolated pores are formed when the pore channels break up due to capillarity induced instabilities [13,14] and the isolated pores are located on the grain corners or, after discontinuous grain growth, inside the grains.

There exists an interest in studying the initial, intermediate and the final stages in order to increase our understanding of the basic processes involved in sintering. The final stage of sintering is, however, the most important from a practical standpoint because for a material to have useful properties (mechanical, electrical and optical), high density is usually required.

2.2. Sintering mechanisms

For materials with low yield points, contact flattening between particles occurs by plastic flow (dislocation motion) [15]. For glasses densification occurs by viscous flow [16]. However, for the great majority of ceramic materials the yield point is too high for significant densification or shape change to occur by plastic flow and, because they are crystalline, viscous flow is not possible [17,18]. Rather, sintering occurs by thermally activated atomic mass transport mechanisms. The mass transport mechanisms are lattice diffusion, either by a vacancy or interstitial mechanism, grain boundary diffusion, surface diffusion, and evaporation and condensation (E/C) with transport through the vapor phase. The various mechanisms and paths are shown schematically in fig. 2.

Both densification and coarsening occur simultaneously during sintering. Only lattice diffusion and grain boundary diffusion lead to a net reduction of the pore volume of a powder compact. This reduction in pore volume occurs because both mechanisms can transport material from the grain boundary between the particles to the surface of the neck region. Surface diffusion and vapor phase transport can only transport material from one region of the particle surface to another. When the porosity is interconnected (initial and intermediate stages) these surface processes allow shape changes which lower the surface curvature and lead to a coarsening of the structure without changing the pore volume. In the initial stage, lattice diffusion from the particle surface to the neck region can cause coarsening [11]. Thus, to have densification, grain boundary or lattice diffusion must dominate over surface diffusion and the source of material deposited at the neck must be the grain boundary.

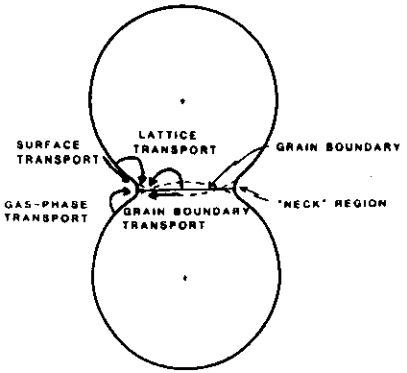

Fig. 2. Atom transport mechanisms and paths during initial stage sintering. Material is removed from the surface and the grain boundary and deposited in the neck region.

2.3. Driving forces

For sintering to occur spontaneously, it must cause a reduction in the total energy of the system. During sintering there is a reduction of the solid–vapor interfacial (or surface) area accompanied by an increase in the solid–solid interfacial (or grain boundary) area. Thus, a necessary condition for sintering to occur at all is that the grain boundary energy be less than the energy of the surfaces being eliminated.

Atom motion occurs due to the defect concentration gradient arising from the stress difference, due to curvature, between the neck region and the grain boundary or particle surface. The equilibrium vacancy concentration at a curved interface (C_v) will be different than at a flat interface (C_v^0) and the difference is

$$C_v - C_v^0 = \frac{-C_v^0 \gamma_s \Omega K}{kT}, \qquad (1)$$

where γ_s is the surface energy, Ω is the vacancy volume, K is the curvature of the interface, T is the temperature, and k is Boltzmann's constant. The stress is taken to be $\gamma_s K$ and, in the convention used here, tensile stresses are negative.

Several initial stage models have been derived which give the concentration gradient causing atom motion. The modelling has been reviewed elsewhere [11,12]. For densification by grain boundary diffusion, the exact form of the stress distribution and the concentration gradient along the grain boundary have been solved analytically for symmetric and asymmetric neck geometries [19]. The stress is tensile at the neck surface and compressive at the center of the grain boundary and, thus, the vacancy concentration is higher at the neck than at the center of the grain boundary. Vacancies will migrate from the neck to the grain boundary. Atoms will migrate in the opposite direction, resulting in densification.

For coarsening, the exact form of the stress distribution has not been determined analytically. The particle surface has a positive curvature (compressive stress - lowered vacancy concentration) and the neck has a negative curvature (tensile stress - increased vacancy concentration). In this case migration of atoms will be from the particle surface to the neck. The problem in determining the stress distribution is in defining the exact curvature along the neck surface and the transition from positive to negative curvature. This problem does not arise in the grain boundary diffusion controlled densification case because the stress at the neck is determined by the force balance at the grain boundary–neck intersection [19].

It must be emphasized that, although the migration of atoms occurs due to the stress gradient between different regions of the particles, the stress gradient is not the driving force for atom motion. Atom motion is assumed to occur by random walk diffusion [20]. An individual atom has no force exerted on it, but rather jumps in a completely random fashion. There is a net migration of atoms due to the vacancy concentration gradient, but the stress gradient is assumed to a first approximation to have no effect on atom motion. Many authors have used the difference in free energy (chemical potential) as the driving force for atom motion. While in sintering this leads to a correct solution for the motion of atoms, there exist situations where the use of the free energy gradient to describe a process occurring by random walk diffusion leads to an incorrect result [21,22].

With few exceptions, the driving force for atom motion, i.e., the differences in curvature among the interfaces in the sintering system, has been modelled using a geometry that is too restrictive. In particular, the curvature at the intersection of the two particles at the grain boundary is modelled as corresponding to an inscribed circle. The actual curvature at the grain boundary–surface intersection is determined by the force balance between the surface and grain boundary tensions. The expression which governs the equilibrium angle, ψ, known as the dihedral angle, and, hence, the curvature, of the grain boundary–surface intersection was derived by Herring [3]. For three general interfaces meeting along a line, the balance of forces is

$$\sum_{i=1}^{3} \left(\gamma_i t_i + \frac{\delta \gamma_i}{\delta t_i} \right) = 0, \qquad (2)$$

where γ_i is the energy of the ith interface and t_i is a unit vector lying in the ith interface and normal to the line of intersection of the interfaces. The vector quantities $\delta\gamma_i/\delta t_i$ have the mathematical form of a torque, and are usually referred to as the torque terms. They may also be viewed as a force acting normal to their corresponding interface. The torque terms are especially important for twin boundaries and can allow three boundaries to all lie in the same 180° [23]. Examples of equilibrium curvatures which are results of this force balance are shown in fig. 3 for lenticular pores on grain boundaries. As the grain boundary energy increases relative to the surface energy, the angle of the interfaces at the grain boundary–surface intersection decreases. When the grain boundary energy is greater than or equal to twice the surface energy, the angle is zero and the particles will not form a grain boundary. When the torque terms are large or when the grain boundary energy approaches zero, which occurs for low angle and twin boundaries, ψ approaches 180°. For isotropic grain boundary (γ_g) and surface energies

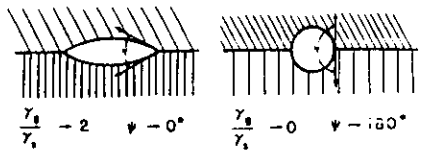

Fig. 3. Shape of pores on grain boundaries for different dihedral angles. As ψ approaches 0°, pores become elongated and as ψ approaches 180°, pores are rounded.

(γ_s), eq. (2) reduces to

$$\gamma_g/\gamma_s = 2\cos(\psi/2). \quad (3)$$

In ceramics, there are few quantitative data on energies of surfaces and grain boundaries as functions of their crystallographic orientation. Fracture data indicate that cleavage will occur in most ceramics only along specific electrically neutral planes, such as the {100} in rock-salt structures. Cleavage along charged planes leads to faceting into neutral planes. In addition, surface facets are frequently observed after heat treatment. These data suggest that surface energy is dependent on the surface orientation. Grain structures in high density ceramics formed by grain growth frequently contain twins and boundaries which intersect with unequal angles. These observations suggest that the grain boundary energy in ceramics is also a function of the boundary crystallography. As a result, it is apparent that eq. (3) does not apply to ceramics.

In the absence of data on γ_s as a function of surface orientation and γ_b as a function of boundary crystallography, eq. (2) cannot be used to give the grain boundary to surface energy ratio from the measured dihedral angles. Regardless of the inability to deconvolute angular data, measurements of the dihedral angles alone are enough to indicate the curvatures expected at the grain boundary–surface intersections during sintering. At a given particle size and neck size, the local curvature increases as the dihedral angle increases. If the dihedral angle distribution in a material is broad, the driving force for sintering will be nonuniform in the powder compact. In addition, the curvature can vary around the neck of two sintering particles since the surface orientation changes around the circumference [24–26].

In the final stage of sintering, if the dihedral angle is different from 180°, then not all pores will shrink. The stability of pores with respect to densification is determined by the difference in curvature between the pore surface and the source of atoms which is the grain boundary. Since the grain boundary is assumed to have no net curvature, pores whose radii of curvature are outside of the solid grain have negative curvatures and atom transport will occur from the grain boundary to the pore. Pores whose radii of curvature are inside the solid grain have positive curvatures and atom transport will occur from the pore surface to the grain boundary. Pore surfaces with no net curvature are at the same chemical potential as the grain boundary and no atom transport will occur. The curvature of the pore surface (the driving force) varies with both the dihedral angle and the number of sides of the pore [27]. The dihedral angle for pore stability for pores with different numbers of sides is shown in fig. 4a. For example, a four-sided pore in three dimensions that has a 70.5° dihedral angle will form a tetrahedron. Since the sides are straight the pore is stable. If $\psi <$ 70.5°, then the pore has a positive radius of curvature and the pore will grow. If $\psi >$ 70.5°, then the pore has a negative radius of curvature and the pore will shrink. Stable pores with positive or zero curvatures are seen in the MgO sample shown in fig. 4b. For a distribution of dihedral angles, the pore stability criterion is much more complicated. Pores will shrink at different rates locally. While overall there is a reduction of pore volume (densification), some pores may be growing (coarsening). Thus, it is seen that the grain boundary to surface energy ratio, as reflected in the dihedral angle is a critical parameter in determining the driving force for sintering.

2.4. Kinetics

During sintering the migration of atoms will occur simultaneously along all the available paths, that is, in the lattice, in the grain boundary region, along the surface of the particles or in the vapor phase. The net rate of atom motion is a combination of the rate for each mechanism scaled by the appropriate geometric factor [28]. For example, in the initial stage modelling the rate of sintering by grain boundary diffusion scales with the particle size to the fourth power while that for lattice diffusion scales with the third power of the particle size. To accurately model the sintering behavior of real materials a combination of mechanisms must be included [9]. For multiple mechanism models the time dependence exponent is not an integer and the particle size dependence of the

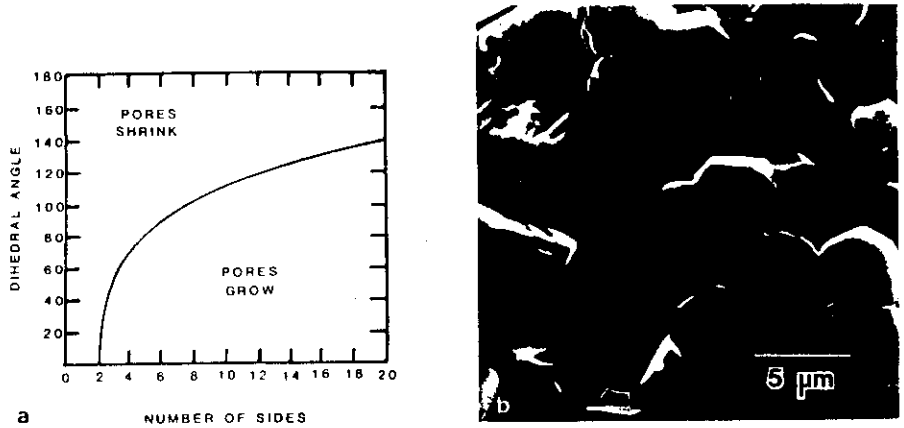

Fig. 4 (a) Stability of pores for different dihedral angles and number of sides [27]. As ψ decreases, a pore must have fewer sides in order to shrink. (b) Photograph of MgO sample showing pores that are stable or growing. All the pores left in the sample have the center of curvature of the sides lying outside the pore.

sintering rate changes as sintering proceeds due to the geometrical changes.

In a multicomponent material all species can migrate. For metal alloys there is no coupling between the species and segregation can occur if the migration rate is very different for the different species. In ionic materials (ceramics) there is an electric field coupling between ions of different charge. This coupling requires that the net migration rates of the different species be in the stoichiometric ratio. The slow moving ions will feel a force tending to speed them up while the motion of the fast moving ions will be retarded [29,30]. The different ions can migrate along different paths and therefore the effective diffusion coefficient will be determined by the slowest ion along its fastest path [31,32]. For the case of combined lattice and boundary diffusion in a single component system, the effective diffusion coefficient is

$$D_{\text{eff}} = D_l + \pi\delta D_b/d, \quad (4)$$

where d is the grain size, D_l is the lattice diffusion coefficient and δD_b is the product of the grain boundary width and the grain boundary diffusion coefficient. For an $A_\alpha B_\beta$ compound

$$D_{\text{eff}} = \frac{(\alpha+\beta)D^{\text{A}}_{\text{eff}}D^{\text{B}}_{\text{eff}}}{\left(\beta D^{\text{A}}_{\text{eff}} + \alpha D^{\text{B}}_{\text{eff}}\right)}. \quad (5)$$

For lattice diffusion by a vacancy mechanism the ionic diffusion coefficient, D_l, is

$$D_l = D_v X_v, \quad (6)$$

where D_v is the vacancy diffusion coefficient and X_v is the mole fraction of vacancies. For boundary, surface, or vapor phase diffusion and lattice diffusion by an interstitial mechanism the mole fraction of vacancies is taken to be unity and the ionic diffusion coefficient equals the defect diffusion coefficient.

Grain growth is also occurring during sintering. Because the different mechanisms for shrinkage have different grain size and pore size dependences, the dominant mechanism will change as grain growth occurs. Thus, lattice diffusion may begin to dominate at long times when the grain size is large, even though the boundary diffusion coefficient is much higher than the lattice diffusion coefficient. The dominant mechanism may

change with temperature since the different diffusion coefficients have different temperature dependences. Surface diffusion, which generally has the lowest activation energy, will dominate at low temperatures while, at high temperature lattice diffusion will dominate. During any sintering experiment, it is also necessary to compensate for the nonisothermal interval during heating. Theoretical calculations show that under certain conditions, processes occurring during heating can dominate the initial stage kinetics [33].

Geometrical constraints require that the migration rates for different mechanisms be within specific ranges. For example, in the case of densification in the initial stage by lattice or boundary diffusion, it is necessary that surface diffusion be rapid enough to redistribute the material that is removed from the grain boundary region. If surface diffusion is too slow, the curvature at the neck will decrease and the densification rate will decrease [11,34]. However, if surface diffusion is too rapid, coarsening, not densification, will dominate throughout the initial stage.

The modelling that has been done usually assumes that reactions at the interface (creation or annihilation of vacancies) are not rate controlling. If interfacial reactions are important then the modelling is much more complicated and the predicted time and particle size dependences are different from those usually used [6]. While interfacial control does not seem to be important for most ceramics, it can not be ruled out without some supporting evidence, such as creep measurements.

2.5. Microstructure in the final stage

The final stage of sintering starts when the break up of interconnected pore channels leads to isolated pores which lie along three- or four-grain junctions [7,13,14]. The instability analysis of Mullins [35,36] gives the wavelengths of the perturbations which lead to breakup of the continuous channels into discrete spherical particles. Recent calculations [14] have been performed showing the effect of dihedral angle, ψ, on the stability of channels along the intersection of three grains. It was found that channels become more stable with respect to perturbations as ψ decreases and the diameter for which the channel surface becomes unstable also decreases as the dihedral angle decreases. Since channels with a large curvature (large ψ) shrink faster than channels with a small curvature (small ψ), the results of the perturbation analysis lead to the prediction that in a single sample the channels with the larger ψ will breakup into discrete particles at a lower local density than for channels with smaller dihedral angles. For a system with a distribution of dihedral angles, isolated pores will coexist with open pore channels during the transition to the closed pore stage.

In the final stage pores do not necessarily shrink, as discussed in section 2.2. There are two mechanisms by which pores coarsen: mass transfer between isolated pores and pore coalescence during grain growth. Due to the distribution of dihedral angles and defects in particle packing, some pores grow while adjacent pores shrink. The pores with the appropriate dihedral angles and number of sides can serve as sources of mass for shrinking pores. Pores that remain attached to grain boundaries during migration will coalesce as grains disappear [37]. In the following discussion, grain growth without pores will first be described, followed by a review of the current modelling of the interactions between pores and grain boundaries.

The driving force for grain growth is the curvature (K) of the grain boundaries [38], not $\gamma_g K$ (the grain boundary energy–curvature product), as is usually assumed. The curvature is determined by the number of grain sides and by the orientation dependence of the grain boundary energy. For a material with isotropic grain boundary energy, at three-grain junctions the grain faces must meet at 120°. In a 2D array of hexagonal grains, the grains will have straight sides of equal length and will be stable. Grains with fewer than six sides will have curved boundaries with the center of curvature lying inside the grain and will shrink. Grains with more than six sides will have the centers of curvature for the sides outside the grains and will grow. If the boundary energy is not isotropic the relationship is much more complicated and depends on the specific grain boundary misorientation with each of the surrounding grains. Recent Monte Carlo simulations of grain growth with isotropic grain boundaries energies show normal grain growth while inclusion of a distribution of grain boundary energies leads to a bimodal grain size distribution after grain growth [39].

During grain growth pores must either move along with the grain boundary or become separated and "trapped" inside grains. In ceramics, pores that are trapped shrink at much lower rates than pores that remain on boundaries. Anion lattice diffusion is typically orders of magnitude slower than cation lattice diffusion [40,41]. Since ambipolar coupling requires that the ions be transported in the stoichiometric ratio, the migration of cations will also be low and, hence, pore shrinkage by lattice diffusion alone produces little densification. During the final stage of sintering, the critical process in determining the final density is, therefore, pore–boundary separation, since pores that are separated from boundaries shrink too slowly to be removed within reasonable intervals.

The mechanisms for pore migration are surface diffusion, lattice diffusion, and evaporation and condensation through the vapor phase [42]. The dominant mechanism at a given temperature depends on pore size. There are two regimes where pores can remain attached to the grain boundaries; pores, which are small enough, move along with the grain boundaries without affecting their motion; and pores, which are large enough, are immobile but retard the motion of the boundary. The intersection of the two regimes leads to a pore–boundary separation region of the type shown in fig. 5 [43,44].

The condition for separation of large, relatively immobile pores from boundaries during migration is derived by assuming an average retarding force per pore, a space-filling grain geometry with pores located only at 4-grain junctions, and the driving force for boundary migration (curvature) being inversely proportional to the grain size. This relationship is generally known as the Zener limit for grain size as a function of volume fraction of a second phase [43,45].

The conditions for separation of small, mobile pores with different dihedral angles, have been recently modelled [46]. It is assumed that the equilibrium dihedral angle is maintained at the pore–grain boundary intersection. A curved

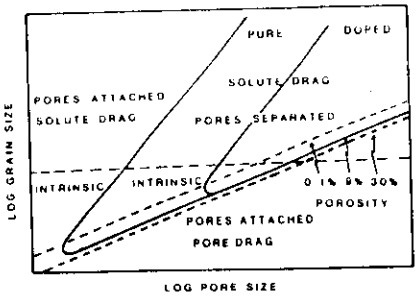

Fig. 5. Schematic map showing the pore–boundary separation conditions for "pure" and doped samples [44]. Large pores retard boundary motion and small pores are able to migrate with the boundary. Boundary motion is either limited by solute drag effects, limited by pore drag, or at the intrinsic mobility.

boundary will change the shape of the pore to maintain the dihedral angle. The driving force for pore migration results from the curvature difference due to this shape change, as shown in fig. 6. The pore migrates by atom motion from the leading edge to the trailing edge of the pore. If a steady state solution for the diffusion flux cannot be obtained for a pore migration rate equal to the velocity of the boundary, the pore will be left behind the moving boundary. For lenticular pores with the same in-boundary radius, the velocity for

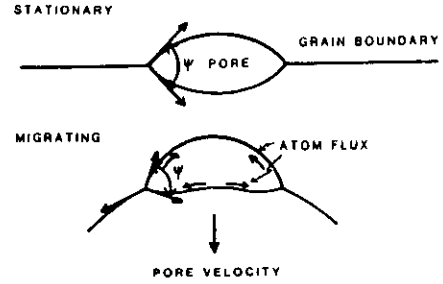

Fig. 6. Pore shapes for pores on stationary or migrating boundaries [46]. When the boundary migrates, the pore changes shape to maintain the dihedral angle. When the pore can not migrate with the boundary, pore-boundary separation occurs.

pore boundary separation was found to increase with decreasing dihedral angle. Thus, pore–boundary separation is seen to depend on the grain boundary curvature (driving force for boundary migration), the pore size (through the rate of migration) and the dihedral angle, which couples the driving force for the pore migration to the driving force for boundary migration.

The dihedral angle is seen to play a major role in determining the microstructure evolution during sintering. The curvature of the pore surface increases as the dihedral angle increases. The value of ψ determines both the rate of neck growth during the initial stage and the pore size at which the transition from the intermediate to final stage occurs. In the final stage, the dihedral angle not only determines the driving force for shrinkage but also affects the pore–boundary separation condition. As mentioned above, pores that are separated from grain boundaries shrink at much lower rates than pores attached to boundaries. The maximum shrinkage rate will be for pores with the largest dihedral angle consistent with avoiding pore–boundary separation. In an anisotropic material there will be a distribution of dihedral angles and, therefore, a distribution of shrinkage rates. This distribution will change during sintering, since, when a pore shrinks to zero size, the dihedral angle corresponding to that pore is no longer present in the population. In sintering, the largest dihedral angles will be eliminated by either pore shrinkage or pore–boundary separation and the measured distribution will shift to smaller dihedral angles [47].

While it is not possible to directly control the pore size or the grain size, the dihedral angle is available to direct external control. The pore size and the grain size are complicated functions of the microstructure evolution and depend on the initial powder packing, diffusion coefficients and particle geometry. The dihedral angle is determined by the interfacial energies and can be changed by controlling the composition. Thus, pore–boundary separation conditions can be modified by changes in composition and this leads to control of the final pore size and density. Changes in the dihedral angle will not affect the grain size except in the limit of large, immobile pores. For the small pore case, the pores can either migrate with the boundary or are separated from it without affecting the grain boundary velocity.

3. Solute incorporation in the lattice, into the grain boundary, and on the surface

Of primary importance in determining how impurities and dopant affect the sintering of ionics is the identification of where the impurities are located in the material: in solution in the bulk, as defect clusters in the bulk, segregated to high-angle grain boundaries, low angle boundaries, or dislocations, or as discrete precipitates in the bulk or along preexisting defects, such as dislocations and grain boundaries. The solubility of a solute in an ionic matrix depends on the strain energy associated with its incorporation into the matrix, the long-range and short-range interactions of the solute with the matrix, and the requirements of lattice site balance and electroneutrality [5,48]. A solute in the lattice will have a different equilibrium solubility than at internal interfaces and external surfaces where several constraints of the lattice have been relaxed [49]. For example, the free energies of formation for various defects, such as Schottky pairs (cation and anion vacancies), can be different for the bulk and at the interface. Electroneutrality in the bulk requires that, in the absence of impurities, anion and cation vacancies be created in the stoichiometric ratio. At interfaces, an excess of the more easily formed defects will exist and the interface will be charged. To maintain charge neutrality in the crystal as a whole, a region of opposite charge, called the "space-charge layer" will exist adjacent to the charged interface. Segregation to such a charged interface is very different from that which would have been predicted in the absence of charged regions.

Impurities are present in the starting chemicals used to produce the precursor powders, and more impurities are introduced during powder production and processing. Many of the impurities in the starting materials can be removed by special processing techniques, for example, by liquid–liquid extraction, multiple distillations or repeated

precipitations [1,2]. By producing and handling the powders in a clean room and by using special laboratory ware, contamination of the ceramic precursor can be minimized. The need to heat-treat the powders without contamination means that the crucibles and the furnace refractories must be of high purity and as inert as possible. To provide a diffusion barrier, samples may be sintered packed in powder of the same composition as the sample and enclosed in a high-purity covered crucible. Ideally the sample, the crucibles, and the refractories would all be of the same composition. In spite of all such precautions, some compositional degradation may and generally does occur. The most common impurities introduced during processing are Ca, Si, Al, Na, Fe, K, Cl, OH, and C. It must also be remembered that for chemical analyses to be meaningful, the same precautions must be taken during the preparation of samples and measurement to ensure that no additional contamination occurs.

The contamination of MgO during routine (typical) experimentation frequently leads to concentrations of several hundred ppm of Ca and Si [1]. The single crystals of MgO with the lowest background impurity levels have been reported to contain 90 ppm total cation impurities [50], with Al being the major contaminant. Although the samples were not analyzed for carbon or chlorine, it is felt that there are high levels of these anions due to the growth conditions. High purity $MgCO_3$ (hydrated) prepared using liquid–liquid extraction and impurity masking techniques under clean room conditions was found to contain Ca at 2 μg/g Mg metal as the only element of valence $\geq +2$ above the detection limit (1–5 μg/g) as measured by induction coupled plasma emission spectroscopy. The concentrations of Na and K varied significantly from sample to sample and were measured by atomic absorption to be between 1 μg/g (the detection limit) and 20 μg/g. However, on subsequent heat treatment of the high purity carbonated, the Ca and Na concentrations were observed to have increased to 270 μg/g and 120 μg/g, respectively.

For the purpose of our discussion of the effects of solutes on the sintering of ionics, it is useful to divide solubility behavior into three distinct ranges: extensive solubility, limited but measurable solubility, and a solubility below detection limits (< 1 ppm). The effect of a specific impurity on the transport properties, interfacial energies and interfacial structures will depend on the solubility range in which it lies. Theoretical and experimental results for various solutes in MgO are used in this section to illustrate the effects expected in each solubility range. In the following sections on transport and interfacial properties, results from the systems Al_2O_3, NiO, CoO, MnO, FeO, NaCl, KCl, BaF_2 and LiF have also been included.

In systems showing extensive solid solubility, the solute ions are usually isovalent with the matrix and the ionic size is close to that of the matrix ion that the solute replaces. Examples of systems showing extensive solubility are NiO–MgO and CoO–MgO. In both systems the end members exhibit complete solid solubility. When the ionic size or the valence of the impurity differs from that of the matrix ion, more limited solid solutions are formed. In the CaO–MgO system, the maximum solubility of CaO in MgO is 7.8 wt% at 2643 K [51]. Even though Ca is isovalent with Mg, the solubility is still limited due to the size mismatch. In the MgO–Al_2O_3 system, the maximum solubility of Al_2O_3 in MgO is 18 wt% at 2268 K [52]. The solubilities of SiO_2 and ZrO_2 in MgO are so small as to be not currently measureable [53].

From the solubilities of Ca, Al, and Si in MgO it is expected that segregation of these ions should occur at grain boundaries and free surfaces at all temperatures. Recent electrostatic calculations on the segregation of isovalent impurity cations to the electrically neutral surfaces in MgO, the {100} and the {110}, have been performed by Tasker et al. [54]. The results suggest that Ni^{2+} is repelled from the free surfaces and that Ca^{2+} is segregated positively. At high Ca concentrations where a monolayer coverage is predicted, reconstruction of the surfaces is also expected. No equivalent calculations have been performed for grain boundaries in MgO although qualitatively the same results are expected. In a STEM study no enrichment of Ni above the detection limit was found at MgO grain boundaries [55]. In a study of Sc segregation to grain boundaries in MgO [56], grain boundary

segregation of Sc, Si, and Ca was observed by Auger electron spectroscopy, as seen in fig. 7.

The solubility of Si in MgO is very low [53]. This is due to the combined effects of the size difference, charge difference, electronegativity difference and bonding type. Si impurities will be seen as discrete second phase particles (which may incorporate other ions) or as a glassy phase. Calculations [57] suggest that the disjoining pressure prohibits simple monolayer coverage. Only some boundaries are covered with SiO_2 where it exists as a glass several monolayers thick. Other boundaries will be free of a second phase, i.e. not "wetted".

The solubility of an ion can be different when another ion is also present. If one ion has an ionic size larger than the host, and the other is smaller, then the strain effect can be partially compensated and the solubility will be larger than for either ion alone. This is seen for the case of Mg and Ti in Al_2O_3 [58]. The maximum solubility when both are present is increased relative to that for either individually. Similarly, the electrostatic effects can be compensated. Simplistically, addition of both a monovalent cation and a trivalent cation to MgO would not lead to the formation of vacancies since there is no charge imbalance as occurs when only one aliovalent ion is incorporated.

Because several constraints (elastic, site balance and electroneutrality) of the lattice have been relaxed at interfaces, the concentrations of impurities will be different there than in the bulk. If the concentration at the grain boundary or free surface is larger than in the bulk, the amount of solute that can be incorporated into a particle compact or polycrystal without precipitation will depend on the interfacial area. During coarsening in the initial stage and grain growth in the final stage of sintering, the interfacial area decreases and precipitation of new phases may occur [59].

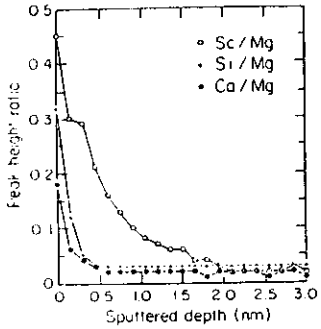

Fig. 7. Comparison of solutes, segregated to grain boundaries in MgO, as a function of distance from the boundary (from Chiang et al. [56]).

3.1. Mass transport

Calculations of the point defect formation, association and migration energies in many oxides, including MgO, and α-Al_2O_3, have recently been performed [48,60,61]. These calculations which allow for lattice relaxations are based on the shell model of ions and use electron-gas potentials and two-body interaction only. The methods for calculation and the defect formation, association, and migration energies for MgO and α-Al_2O_3 are reviewed in substantial detail elsewhere [62]. In terms of a discussion of the effect of impurities on mass transport during sintering, the most important parameters are the formation energies for Schottky, Frenkel, and anti-Frenkel defects and how these unassociated defects and clusters of defects are affected by the presence of impurities. In MgO the formation of Schottky pairs (one cation and one anion vacancy) is dominant with an energy of formation of 7.5 eV (3.7 eV per defect). For α-Al_2O_3, the formation of Schottky defects in the stoichiometric ratio (two cation vacancies and three anion vacancies) is also favored over Frenkel and anti-Frenkel defects and has a formation energy of 25.2 eV (5 eV per defect). Using these values, the intrinsic cation and anion vacancy concentrations at various temperatures have been calculated, and are given in table 1. At temperatures as high as the melting point for both materials, the intrinsic defect concentrations are orders of magnitude lower than the lowest impurity concentrations achieved in either single crystals or powders.

In terms of Kröger–Vink notation [63], the incorporation of NiO, CoO or CaO, as a substitutional solid solution, into MgO is expressed as

$$MO_{MgO} \rightarrow M^{\times}_{Mg} + O^{\times}_{O}, \qquad (7)$$

where M is Ni, Co, or Ca, the subscript denotes the site on which the ion resides, and the asterisk indicates that the species is electrically neutral. The incorporation of Na_2O, Al_2O_3 and SiO_2 into MgO is expressed as

$$Na_2O_{MgO} \rightarrow 2\,Na'_{Mg} + V^{\cdot\cdot}_{O} + O^{\times}_{O}, \qquad (8)$$

$$Al_2O_{3\,MgO} \rightarrow 2\,Al^{\cdot}_{Mg} + V''_{Mg} + 3\,O^{\times}_{O}, \qquad (9)$$

$$SiO_{2\,MgO} \rightarrow Si^{\cdot\cdot}_{Mg} + V''_{Mg} + 2\,O^{\times}_{O}. \qquad (10)$$

As can be seen from the incorporation equations for trivalent and tetravalent impurities in MgO, vacancies on the magnesium lattice are formed as required by electroneutrality and site balance. When the vacancy concentration of one ion is raised, the vacancy concentration on the other sublattice is lowered as required by the Schottky equilibrium. For example, when only trivalent impurities are present in MgO, the concentration of Mg vacancies is equal to the trivalent impurity concentration and the anion vacancy concentration decreases. In order for MgO to contain the intrinsic vacancy concentration, the total trivalent cation concentration must be less than 1 ppb at 2000 K and less than 1 ppm at the melting point. For 20 ppm Al in MgO at 2000 K, the $[V''_{Mg}] = 10^{-5}$ (10 ppm) while $[V''_{O}] = 1.2 \times 10^{-14}$. Since the diffusion coefficient is proportional to the vacancy concentration (eq. (6)), Mg lattice diffusion would be significantly enhanced while oxygen lattice diffusion would be suppressed. The type of defects formed upon addition of impurities is not limited to unassociated vacancies or interstitials. Calculations of defect association energies in MgO [48] indicate the trivalent cations lead to the formation of unassociated vacancies, dimers, and trimers while quadravalent cations are incorporated only as part of a defect associate with Mg vacancies. Incorporation of monovalent cations in substitutional sites leads to formation of oxygen vacancies which then form associates with the cation. Since Mg vacancy formation is suppressed and Na moves by a cation vacancy mechanism low mobilities of Na in the MgO lattice are expected.

Table 1
Intrinsic concentration of Schottky defects in MgO and Al_2O_3

$0_{MgO} \rightarrow V''_{Mg} + V^{\cdot\cdot}_{O}$, $E_f = 7.5$ eV

T (K)	$[V''_{Mg}] = [V^{\cdot\cdot}_{O}]$
1000	1.2×10^{-19}
1500	2.5×10^{-13}
2000	3.5×10^{-10}
2500	2.7×10^{-8}
3000	5.0×10^{-7}
3125	8.9×10^{-7}

$0_{Al_2O_3} \rightarrow 2\,V'''_{Al} + 3\,V^{\cdot\cdot}_{O}$, $E_f = 25.2$ eV

T (K)	$[V'''_{Al}] = \frac{3}{2}[V^{\cdot\cdot}_{O}]$
1500	8.4×10^{-18}
1750	2.3×10^{-15}
2000	1.6×10^{-13}
2345	1.2×10^{-11}

The above defect equilibria and incorporation mechanisms apply only to the lattice. Colbourn and Mackrodt [64] have also calculated the formation energies of intrinsic defects at {100} in MgO to be slightly lower (0.3–0.4 eV) than in the bulk. However, when impurities segregate to interfaces, the defect reactions are much more complex and, to date, no calculations combining both segregation and defect equilibria at interfaces have been performed.

An important implication of interfacial segregation for mass transport during sintering is that the diffusivities along interfaces may change as the particle size/grain size changes without any change in the total impurity concentration in the material [59]. If an impurity segregates to an interface, the "solubility" of a solute in a polycrystal can be significantly higher than a single crystal. For a given impurity concentration, the solute concentration at interfaces will increase as interfacial area is eliminated and diffusion along those interfaces will be affected. If the bulk and the interfaces are saturated with solute, any reduction in grain boundary area will lead to precipitation of a second phase.

The effect of impurities on mass transport in ceramics can be seen from comparing the measured diffusivities of nominally the same material.

The lattice, grain boundary, and gas diffusion constants in MgO have recently been reviewed [65]. Lattice diffusivities span four orders of magnitude at the same temperature, as shown in fig. 8. Grain boundary diffusivities span three orders of magnitude. Surface diffusion data is in better agreement. The lattice diffusion data for Al_2O_3 shows an even wider range of measured lattice diffusion coefficients for nominally the same material.

Greater attention has recently been focussed on the effects of impurities on mass transport. Diffusion of Fe tracer in undoped and Mg-doped Al_2O_3

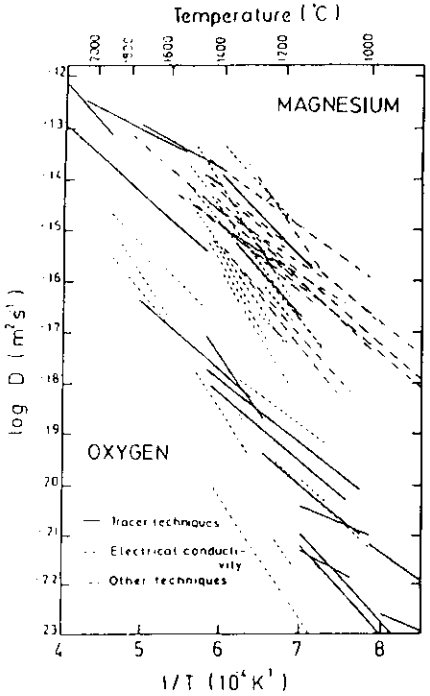

Fig. 8. Lattice diffusion coefficients of magnesium and oxgen in MgO (from Vieira and Brook [65]). Measured magnesium diffusion coefficients vary by four orders of magnitude at typical sintering temperatures.

[66] samples was observed to exhibit Si-dominated diffusion behavior at measured Si concentrations of 2 ppm. In a study of high temperature conductivity and creep of polycrystalline undoped, Ti-doped, and Fe-doped Al_2O_3 [67], it was found that the compositions of samples were different with respect to impurities as well as dopants and that the composition did not change in a systematic way with heat treatment. The concentration of Si ranged from 96 to 700 ppm; Mg from 10 to 50 ppm; Ca from 3 to 73 ppm; Mn from 21 to 61 ppm; and Fe in the samples not Fe-doped from < 10 to 32 ppm. In some cases, second phases were observed. The scatter in mass transport data is not surprising considering these typical experimental difficulties.

The effect of dopants on the surface diffusion coefficient (ωD_s) has been measured by two different techniques with conflicting results. Measurements of the rate at which grain boundary grooves developed in pure and MgO-doped Al_2O_3 [24] showed no effect of impurities on ωD_s for temperatures below 1570 K. MgO was found to increase ωD_s above 1570 K. A study of scratch smoothing on basal planes (0001) of undoped and MgO-doped Al_2O_3 single crystals [68] showed that at 1920 and 1970 K the presence of MgO decreased the surface diffusion. Whether the difference arises due to the presence of other impurities in the different samples or reflects an orientation dependence of the surface diffusion coefficient is not known.

3.2. Interfacial properties

The structures and the energies of surfaces and grain boundaries and the segregation to these interfaces are, with few exceptions, understood only qualitatively for ceramics [69]. Most of the experimental data for "undoped" material are actually for material with significant impurity concentrations. Until recently, calculations of surface and boundary energies were based on perfect interfaces and on defect- and impurity-free, stoichiometric materials at 0 K. According to one prominent researcher in the field these surfaces are merely "science fiction" [70]. However, these models of ionic surfaces do provide a starting

point to assess how the "model" experiments deviate from the model calculations. The mathematical approach and the results of various calculations are reviewed elsewhere [71–73]. In this paper several recent results are discussed which have particular importance to sintering. These are: calculations of surface energy anisotropy; the change in grain boundary energy with orientation; and multicomponent segregation effects.

The change in interfacial energy, γ, with impurity adsorption was treated by Gibbs [74] and is, for i species with chemical potentials, μ_i, at constant T and p:

$$\left.\frac{\delta\gamma}{\delta\mu_i}\right|_{T,p,\mu_{j\neq i}} = -\Gamma_i, \tag{11}$$

where Γ_i is the surface excess concentration of the ith species. For a positive surface excess (adsorption or segregation of the ith species to an interface), the interfacial energy must decrease. It is a common misconception that impurity segregation or adsorption must decrease the energy of the highest energy interfaces more than that of the lower energy interfaces and interfaces will become more isotropic. There is no general relationship between the relative energies of surfaces before and after adsorption or segregation.

For a given material at constant temperature, the variation of surface energy, γ_s, with surface orientation can be easily visualized by reference to the Wulff plot. The Wulff plot is the polar projection of the three-dimensional variation of γ_s with orientation and is the plot of the vector $\boldsymbol{r} = \gamma_s(\boldsymbol{n})\cdot\boldsymbol{n}$, where $\gamma_s(\boldsymbol{n})$ is the surface energy of the plane whose normal is $\boldsymbol{n}$. The equilibrium shape of a material can be derived by constructing the planes normal to $\boldsymbol{r}$ for all orientations. The inner envelope of planes (the Wulf construction) corresponds to the equilibrium shape which must have the same symmetry as the material. In ceramics which facet, the shape of the Wulff construction can be deduced from the observed orientations between facetting planes. As shown in fig. 9 for Al_2O_3, the facetting on the as-fired surface of a sintered undoped Al_2O_3 sample leads to the equilibrium shape shown in fig. 10. Changes in the Wulff plot with composition changes are discernable through transitions in the equilibrium shape. However, independent methods are required to determine the magnitudes of γ_s.

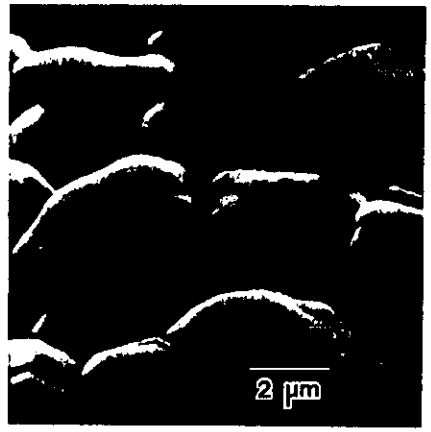

Fig. 9. Faceting on a fired surface of high purity Al_2O_3.

In ceramics, estimates of surface energies come primarily from cleavage data. Cleavage occurs most easily along electrically neutral planes with the lowest bonding energy and, in general, corresponds to the free surfaces with the lowest γ_s. The energies from cleavage are upper limits to γ_s since relaxation, reconstruction and adsorption can occur after cleavage to lower γ_s. Selected values of γ_s are shown in table 2. As illustrated by the range of energies for MgO, LiF, and NaCl, the strength of

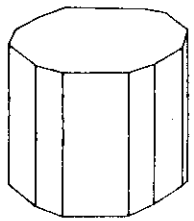

Fig. 10. Equilibrium Wulff shape for Al_2O_3 derived from faceting.

Table 2
Surface energy from cleavage measurements

Material	Fracture plane	Temperature (K)	γ_s (J/m^2)	Ref.
MgO	(100)	77	1.20	[76]
LiF	(100)	77	0.30	[76]
NaCl	(100)	77	0.30	[5]
BaF_2	(111)	77	0.28	[76]
Al_2O_3	$(10\bar{1}2)$	298	6.00	[77]
Al_2O_3	(0001)	298	> 40	[77]

bonding plays a significant role in determining γ_s. In Al_2O_3 there is no pronounced cleavage plane and the above values of γ_s correspond to a surface composed of complex facets. Several compilations have been made of surface energy data for ceramics, primarily from cleavage experiments [75–77]. There are no data for the energies of specific planes other than cleavage planes.

In the static lattice calculations of surface energy, a general requirement is that the surface must be electrically neutral and have no net dipole moment. For rock-salt structure ceramics these requirements are easily met only for {100} and {110} surfaces. Impurities or major reconstruction is required to stabilize higher index planes. In the absence of reconstruction or impurities, highly charged surfaces, such as {111}, should never be observed. Calculations do appear to accurately model the {100} surface energies and structures. It is accurately predicted that {100} is the lowest energy surface and thus, cleavage will occur to create two {100} surfaces in rock-salt structure ceramics. Low energy electron diffraction (LEED) results [78] also show that the surface structure of MgO {100} is very close to that assumed in the calculations [79]. However, {100} {110}, and {111} surface facets have been observed in LiF [80]. In other experiments, such as the study of dihedral angles in MgO [81], no surface facetting of rock-salt structure ceramics is observed. This indicates less variation of the surface energy with surface plane and, hence, no singular planes on the Wulff plot.

Similar calculations of interfacial energies have been performed for ⟨001⟩ twist boundaries in MgO, NiO, MnO, FeO, and CoO [82–84] and ⟨001⟩ and ⟨011⟩ tilt boundaries in NiO and MgO [82]. In these calculations only boundaries constructed of periodic units can be modelled. These special boundaries are usually described as either being of high coincidence, meaning that there are many atoms in the boundary which reside on lattice sites of both grains or alternatively described as being of low Σ, where a number followed by Σ is the inverse of the number of atoms coincident with lattice sites in both grains. A boundary which is a $\Sigma 3$ has 1/3 of atom sites shared by both grains; a $\Sigma 1$ is a perfect crystal. For high coincidence ⟨001⟩ twist boundaries the grain boundaries were found to be only slightly more stable at 0 K than the surfaces from which they are made and no high coincidence (low Σ) boundaries should form.

At first analysis, the prediction of unstable ⟨001⟩ twist boundaries seems to be in direct conflict with experimental results. In experiments using MgO smoke particles which are {100} cubes, the misorientation between cube pairs was measured and the frequencies of ⟨001⟩ twist boundaries with high coincidence misorientations were found to be much greater than for those with random misorientations [85–88]. Secondary grain boundary dislocations in ⟨001⟩ twist boundaries near coincidence have been found which bring the boundaries into perfect coincidence [89]. This implies that the lowest energy configuration of the interface is at the coincidence misorientation. However, there exists experimental evidence that impurities stabilized the high angle ⟨001⟩ twist boundaries and that the cusps in the frequency-misorientation curves are due to these impurities. In the published discussion following the paper by Chaudhari and Charbnau [87], it was stated that the cusps in the frequency plot for MgO were seen in samples which also contained ⟨111⟩ twins, another energetically unfavorable interface [88]. In other samples no cusps and no twins were observed and the predominant interface was of perfect coincidence ($\Sigma 1$), i.e,. single crystals formed. It was subsequently found that ⟨111⟩ twins in MgO smoke particles only occur in the presence of water vapor [88]. These combined results imply that water vapor stabilizes the high coincidence (low Σ) ⟨001⟩ twist boundaries and that random

high angle grain boundaries remain less energetically favorable than two {100} surfaces.

The issue of how the energies of interfaces change as a result of segregation has begun to be addressed using the same simulation procedures as for electrically neutral surfaces and for special grain boundaries. For isovalent impurity cations in MgO calculated segregation of Ca^{2+}, Sr^{2+}, or Ba^{2+} up to monolayer coverage decreases both $\gamma_s\{100\}$ and $\gamma_s\{110\}$ [54]. Segregation of Ni^{2+} or Ba^{2+} was found to increase $\gamma_s\{100\}$ but to decrease $\gamma_s\{110\}$ slightly. A curious result of the calculations was that on segregation of Ba^{2+} and Sr^{2+} to MgO surfaces the surface energy decrease due to segregation is greater than the surface energy of the {100} and the {110} without segregation. If taken literally, this implies that γ_s becomes negative. Although this is a non-physical result, the important trend is that the energy of the system can be reduced substantially with segregation.

Since many different impurities which segregate to interfaces are present simultaneously in ceramics [56, 90–83], it is important to determine the segregation behaviour of the assemblage of impurities and how the interfacial energies are changed. Equilibrium solute segregation has been calculated for grain boundaries in KCl using the calculus of variations to minimize the free energy [94]. The space charge, elastic field, and dipole contributions have been included as have the effects of temperature and solute concentration. It was found that for two divalent cations in KCl with different ionic sizes, one solute can be depleted from the grain boundary while the other can be significantly enriched due almost solely to the effects of solute–solute interactions. Solute–solute repulsion has been observed recently for segregation of Mg^{2+} and Ca^{2+} to {0001} surfaces of Al_2O_3 doped with 40 ppm Mg and with Fe, Ca, V, and Ni impurities totaling < 50 ppm [95]. Segregation of Mg^{2+} was detected only in the regions where Ca^{2+} was absent. In the absence of Mg^{2+}, Ca^{2+} segregated to the free surface.

For sintering the important parameter is not the absolute magnitude of the interfacial energies. Rather the relative magnitudes and orientation dependences of the interfacial energies are necessary for determining the driving force for sintering and predicting the microstructure evolution. The angle formed at the intersection of a grain boundary with the free surface (the dihedral angle) is an easily measurable parameter which can provide information about the relative magnitudes of the interfacial energies.

The dihedral angle can be measured from thermal grooves formed on the free surfaces of polycrystalline samples. The use of cylindrical samples with individual grain boundaries cutting through the z-axis ("bamboo wires") allows the surface orientation to be varied for a single grain boundary orientation [96]. Use of a polycrystalline material with thermal grooves allows a variety of different grain surface and grain boundary orientations to be examined but the determination of the exact misorientation between grains corresponding to a specific dihedral angle is difficult. For measurement of dihedral angles on surfaces initially polished flat and then heat treated to form grain boundary grooves, a technique using metal reference lines has been developed to allow measurement of the total population of grooves from a sample surface [47]. A series of parallel lines are placed on the sample surface after heat treatment using photolithography and the angles are measured from SEM micrographs taken at known tilt angles, as shown in fig. 11.

Using this technique the effect of MgO additions to Al_2O_3 was measured [47]. The results are shown in fig. 12. It is seen that when MgO is present the distribution of dihedral angles is narrower, but the mean is unchanged. The mean value is 117° which is considerably lower than the value of 152° that had been previously used [97]. This low value of the mean dihedral angle and the distribution of values has several implications for sintering. The narrowing of the distribution means that the curvature at particle–particle contacts is more uniform leading to a narrowing of the range of shrinkage rates occurring in the material. The transition from continuous pore channels to isolated pores will occur over a narrower range of local densities and the pore–boundary separation conditions will be nearly the same throughout the sintering compact. The low value of the dihedral angle also allows higher grain boundary velocities

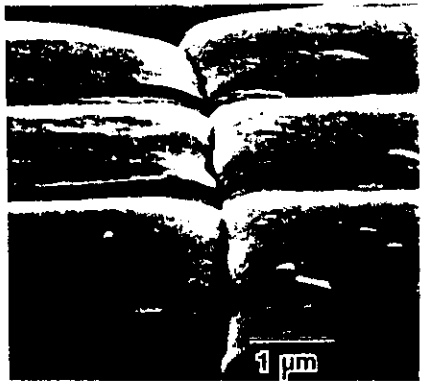

Fig. 11. Metal reference lines on thermally grooved surface of Al_2O_3 [1]. The lines allow the angle of the groove to be accurately measured.

for which pores can remain attached to grain boundaries. All of these effects of narrowing the distribution in dihedral angle and lowering the mean value improve the sinterability of Al_2O_3.

3.3. Solute drag on boundary migration

Using the intrinsic grain boundary mobility (M_0) derived from reaction rate theory [98], the

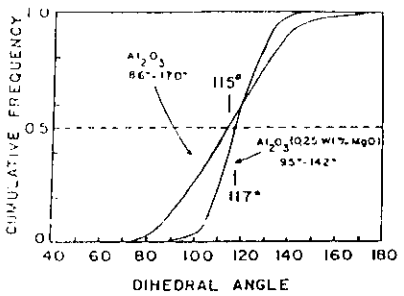

Fig. 12. Distribution of dihedral angles measured using metal reference line technique [47] for doped and undoped Al_2O_3. The addition of MgO is seen to narrow the distribution, but the mean remains unchanged.

velocity (V) of a high angle grain boundary for a driving force (F) is:

$$V = \frac{D_b}{\delta}\frac{\Omega F}{kT} = FM_0, \tag{12}$$

where δ is the boundary width and Ω is the ionic volume. In a multicomponent system, the boundary diffusion coefficient of the slowest species should be used. This calculated velocity is then an upper limit, with mobilities being lower due to the details of the boundary structure. A model has been developed assuming that only a fraction of the boundary sites are available as sources and sinks for atoms migrating across the boundary [99]. The velocity is then reduced by a factor proportional to the density of active sites.

The presence of a solute which interacts with the grain boundary can have a dominant effect on boundary migration [37,100,101]. Near a stationary boundary the solute will have a concentration distribution due to the combined electrostatic and strain interaction [49] which is symmetrical and thus will not exert a net force on the boundary. When the boundary migrates the distribution will be asymmetric and this results in a net force on the boundary which retards boundary migration. Because the solute concentration is not at equilibrium, solute will diffuse across the boundary. The boundary is moving and the solution to this moving boundary problem gives the concentration profile near the boundary. If a steady-state solution exists then the impurity can migrate along with the boundary. If no steady-state solution exists, the boundary will break away from the solute.

An approximate expression of the force–velocity expression is:

$$F = \frac{V}{M_0} + \frac{\alpha C_0 V}{1 + \beta^2 V^2}, \tag{13}$$

where C_0 is the solute concentration in the bulk, α is related to the impurity drag at low velocities, and β^{-1} is the velocity with which the solute atoms migrate across the grain boundary. As shown in fig. 13, there are two regions of boundary migration in the presence of an interacting solute. At low velocities the solute can migrate with the

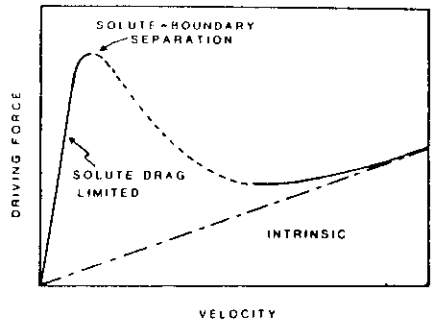

Fig. 13. Driving force–velocity relationship for grain boundaries with a solute that interacts with the boundary [100]. At low driving forces the solute retards the boundary motion, while at high driving forces the boundary is able to break away from the solute and migrate with its intrinsic mobility.

boundary and the velocity is limited by the diffusion of the solute. At high velocities the boundary sheds the solute and moves at the intrinsic velocity.

The boundary migration observed in doped materials is often not uniform [37]. This is expected based on the above analysis. If a boundary in the solute drag region develops a fluctuation in velocity, the faster moving area will have less solute since less can keep up at that velocity. Since the boundary has less solute its effective mobility is larger and it can move faster. This leads to a further reduction in the solute concentration depending on the size of the fluctuation and the increase in mobility with lowered solute concentration. Thus, fluctuations can grow and lead to nonuniform rates of migration even along the same boundary. These trends have been seen for boundary migration during recrystallization in KCl [37,102].

Under the proper conditions the presence of a solute can control grain growth in a ceramic material. The solute lowers the rate of boundary migration during sintering, and allows pores to remain attached to the boundaries. In fig. 5 the conditions of pore attachment for solute drag limited boundary migration during sintering are shown schematically. The pores would continue to shrink and higher final densities would be achieved. Conclusive experimental evidence of this effect during sintering does not currently exist for any system.

4. Discussion

While there exists a qualitative understanding of how many processing and materials parameters affect microstructure evolution during sintering, what is lacking is the ability to make quantitative predictions about these effects. This is due to a variety of reasons. One major problem is the models developed for ideal geometries are far too restrictive to describe the changes that are occurring in a real powder compact. The variation in particle size and packing, anisotropy of properties and the interrelationships among different transport mechanisms have not yet been adequately modelled. As a result of these deficiencies in the models, experimental results do not agree with calculations, even when experiments are done on ideal geometries. The models need to be extended to include anisotropy and multiple mechanism effects. This requires that our understanding of the atomistics of diffusion processes and the driving forces for transport be improved to include these effects.

Even if more physically meaningful models are developed, the data base of materials parameters required to test the sintering models does not exist for any ceramic. In MgO and Al_2O_3, lattice diffusivities measured at the same temperature vary over four orders of magnitude. This is due to differences in experimental technique and differences in chemical composition.

Thus while we can not get specific information on materials parameters from kinetic studies of sintering, the effect of processing parameters can be studied. Qualitatively the effect of particle size, powder packing, and particle size distribution are understood. The change in the dominant transport mechanism with changes in geometry during sintering has been adequately modelled, and the models for non-isothermal sintering have also been developed and are in good agreement with experi-

ment. What has not been included in the models is the effects of impurities, which can dominate all other effects.

There have been comparisons of the sintering behaviour of systems with varied, but documented, chemical compositions. MgO powders of moderate impurity levels (total cation impurities 500 to 1000 μg/g Mg metal basis) sinter easily to high density whereas MgO powders with approximately 400 μg/g total cation impurities (including 270 μg/g of Ca and 120 μg/g Na) do not sinter beyond approximately 80% of theoretical density [1,103]. The unsinterability of high purity BeO has also been reported [104]. These results and the many others in the literature indicate the effect of composition on sintering but do not allow the mechanism by which sintering is affected to be determined. Sintering is a complex process and measuring only a few parameters, such as the density and grain size, as a function of composition will not alone lead to a better understanding of the sintering processes. This approach fails because changing the composition changes too many sintering parameters simultaneously.

To determine the effects of impurities on kinetic processes, experiments must be designed to isolate a single process and to change chemical composition in a uniform and reproducable way. A direct measurement of the process should be used where possible, but for many of the materials parameters important to sintering, this presents formidable experimental problems. The chemical composition of samples must be measured throughout the entire sample preparation and heat treatment cycle to assess the changes in contamination during each processing step. During heat treatment, vapor transport may change the concentrations of volatile species, with either enrichment or depletion depending on the composition of the sample environment. In order for the data from isolated processes to be useful for describing sintering in a material, both the sintering studies and the studies of separate properties must be performed using material of the same chemical composition.

Because of the importance of the final stage of sintering on the properties of ceramics, we have concentrated on the effects of impurities and dopants on microstructure evolution in the final stage. The most important parameter in the final stage of sintering is the pore–boundary separation condition. Pores that become separated from grain boundaries are "trapped" within grains and no further pore shrinkage occurs. To develop a controlled microstructure it is necessary to understand the separation conditions and how they can be influenced by composition.

To gain a better understanding of the pore–boundary separation condition, the mobility of grain boundaries (or the grain growth rate in the absence of pores) and the pore mobility must be measured as a function of composition. Although these properties have been measured for several systems, all three measurements have not been performed for the same material. The grain boundary motion in LiF in the absence of pores has been found to depend on part-per-million levels of trivalent impurities even in the presence of high levels of divalent impurities [102]. In recrystallization experiments in KCl and LiF, the grain boundary velocity at a single temperature varied over four orders of magnitude, consistent with different impurities either migrating with or being left behind the moving boundary [94,102]. Recent experiments have shown that MgO additions lower the grain growth rate in polycrystalline Al_2O_3 samples without pores [105]. There have been studies of pore migration in single crystal samples of KCl [106] in which the mechanism was identified. The effect of impurities was not explicitly investigated.

Ideally the surface and grain boundary energies as a function of orientation and composition, and the impurity segregation profiles should also be known. While the compositional profiles can be measured with some difficulty, and an upper limit on the surface energy can be obtained from cleavage measurements, it is experimentally very difficult to make isolated measurements of the grain boundary energy. The grain boundary energy can be measured calorimetrically during grain growth, but only an average value of the grain boundary energy is obtained. What are needed instead are measurements of the grain boundary energy for known orientation differences across the boundary. Since the energies vary considerably with orientation, the pore–boundary separation condition will also vary. The surface energy determined from cleavage is that for an unrelaxed surface without segregation of impurities. During sintering, equilibrium segregation to all interfaces will occur and the energy of surfaces with segregation will be lowered. The surface energy measured from cleavage techniques will be less sensitive to impurity effects due to the lack of segregation.

The dihedral angle is an easily measurable parameter that yields important information about the surface energy and boundary energy anisotropies. Changes in the dihedral angle distribution can be used to monitor the microstructure evolution during sintering. The pore–boundary separation condition, the driving force for pore shrinkage and grain growth are all dependent on the dihedral angle. Measurements of the dihedral angle distribution in MgO-doped and undoped Al_2O_3 have shown that the presence of MgO changes the distribution and allows sintering to full density. It is seen that the optimum distribution of dihedral angle is narrow, so that sintering will be more uniform, and has a mean value that is a trade-off between high pore shrinkage rates (high dihedral angles) and a high pore-boundary attachment force (low dihedral angle). The exact relationship between dihedral angle and the microstructure evolution is complex and has not yet been fully developed although, as discussed above, many aspects of the relationship are known. Because the necessary materials parameters have not been measured for ceramics it is not possible to predict what the exact distribution of the dihedral angle should be for any material. To increase our understanding of the basic phenomena of sintering, comprehensive studies of surface and grain boundary properties, and how they change with composition, are necessary.

A classic example of the dominance of sintering by dopants is the case of Al_2O_3 sintered with and without MgO. Undoped α-Al_2O_3 can be sintered to high density (99.5%) without much difficulty regardless of the cation impurity levels (except for high levels of Na and Si). However the last 0.5% porosity is not removed due to pore–boundary separation. Additions of MgO at levels as low as 200 ppm (below the solubility limit) cause pores to remain attached to grain boundaries and the MgO-doped material sinters to theoretical density [107]. Much of the difficulty in understanding the mechanism by which MgO affects the sintering arose because it was assumed that MgO had only a single effect. Recent results [108] show that MgO has many effects, which, in combination, improve the sinterability of Al_2O_3. It has been shown that MgO raises the effective diffusion coefficient (D_{eff}) [109], lowers the grain growth rate [105] and either does not change the surface diffusion coefficient (ωD_s) significantly [24] or lowers ωD_s by a factor of 10 [70]. An increase in D_{eff} allows pores to shrink faster and thus stay attached to grain boundaries during grain growth, since smaller pores are able to migrate faster. Lowering the grain growth rate also allows pores to remain attached to grain boundaries. A decrease in ωD_s has two effects on microstructure development: coarsening by surface diffusion is suppressed and the mobility of pores by surface diffusion is lowered. The combination of these two effect produces minimal changes in the pore–grain boundary separation condition [108]. We suggest that an additional major effect of MgO additions is the narrowing of the dihedral angle distribution which leads to a more uniform microstructure. While this effect alone does not explain the role of MgO on the sintering of Al_2O_3, it does demonstrate that the driving force for sintering can be altered, along with the kinetics, due to the addition of a dopant.

5. Summary

During the last 40 years of sintering research, an understanding has developed of how many different variables affect microstructure evolution during sintering. The effects of changes in powder particle size and size distribution, initial compact density, heating rate, sintering temperature, time, atmosphere and diffusion coefficients (lattice, boundary and surface) have been modelled for ideal geometries and are experimentally documented in a qualitative fashion. Investigating the effect of these variables has led to a realization that other properties in a sintering system must be included to develop predictive models of mi-

crostructure evolution. These effects include: crystalline anisotropy, multiple transport mechanisms, complex geometries, and impurity effects. In this paper, we have emphasized the effects of variable concentrations of impurities at the trace level that can mask the effects of changing any other system parameter.

Impurities dominate transport in the lattice, along the grain boundary, and along the free surface in ceramics with low intrinsic concentrations of lattice defects. Impurities that segregate to grain boundaries or free surfaces lower the energies of the interfaces. The curvature of the pore surface is determined by the force balance at the pore–grain boundary intersection and will change as the energies of the interfaces change. The curvature can be directly related to the dihedral angle, ψ, the angle between the two pore surfaces, at the pore–grain boundary intersection. Changes in the interfacial energies by impurities will be reflected in changes of ψ.

Because pores that are separated from grain boundaries (trapped inside grains) do not shrink, pores must stay attached to boundaries to achieve high density. Impurities control the migration of pores by diffusion or evaporation/condensation, the migration of grain boundaries by solute drag and the pore–boundary separation condition, by changing ψ which determines the force required for separation.

The dihedral angle, ψ, is one parameter which can be used to monitor the effect of impurities on sintering. A narrow distribution of ψ leads to more uniform sintering with all pores either attached to or separated from grain boundaries. A wide distribution of ψ leads to a heterogeneous microstructure with some pores attached to boundaries and some pores entrapped within grains. The distribution of dihedral angles in a sintered polycrystalline material can be measured using a metal reference line technique on thermal grooves formed at the intersection of grain boundaries with free surfaces. Measurements of chemical composition in conjunction with measurements of ψ allow an effect of impurities on microstructure evolution to be evaluated.

Acknowledgements

The authors are grateful to Robert L. Coble for critical discussions leading up to this paper, and to David L. Olgaard and Katharine G. Frase for reviewing the manuscript.

References

[1] C.A. Handwerker, Sintering and Grain Growth of MgO, ScD Thesis, Massachusetts Institute of Technology (1983).
[2] J.E. Blendell, H.K. Bowen and R.L. Coble, Am. Ceram. Soc. Bull. 63 (1984) 797.
[3] C. Herring, Surface Tensin as a Motivation For Sintering, in: The Physics of Powder Metallurgy, Ed. W.E. Kingston (McGraw-Hill, New York, 1951) p. 143.
[4] J.E. Burke, J. Am. Ceram. Soc. 40 (1957) 80.
[5] W.D. Kingery, H.K. Bowen and D.R. Uhlmann, Introduction to Ceramics (Wiley, New York, 1976).
[6] R.L. Coble and R.M. Cannon, Current Paradigms in Powder Processing, in: Processing of Crystalline Ceramics, Eds. R.F. Davis, H. Palmour III and T.M. Hare (Plenum, New York, 1978).
[7] (a) R.L. Coble, J. Appl. Phys. 32 (1961) 787;
(b) R.L. Coble, J. Appl. Phys. 36 (1965) 2327.
[8] H.E. Exner, Rev. Powder Met. Phys. Ceram. 1 (1979) 7.
[9] D.L. Johnson, Solid State Sintering Models, in: Sintering Processes, Ed. G.C. Kuczynski (Plenum, New York, 1980) p. 97.
[10] M.F. Yan, Mater. Sci. Eng. 48 (1981) 53.
[11] W.S. Coblenz, J.M. Dynys, R.M. Cannon and R.L. Coble, Initial Stage Solid State Sintering Models: A Critical Analysis and Assessment, in: Sintering Processes, Ed. G.C. Kuczynski (Plenum, New York, 1980) p. 141.
[12] H.E. Exner and G. Petzow, A Critical Evaluation of Shrinkage Equations, in: Sintering Processes, Ed. G.C. Kuczynski (Plenum, New York, 1980).
[13] T.A. Gupta, J. Am. Ceram. Soc. 61 (1978) 191.
[14] W.C. Carter and A.M. Glasser, Dihedral Angle Effects on the Stability of Pore Channels, J. Am. Ceram. Soc. (June 1984) C124.
[15] M.F. Yan, Sintering of Ceramics and Metals, in: Advances in Powder Technology, Ed. G.Y. Chen (Am. Soc. Metals, Metals Park, OH, 1982) p. 99.
[16] G.W. Scherrer, J. Am. Ceram. Soc. 60 (1977) 236.
[17] F.R.N. Nabarro, Deformation of Crystals by the Motion of Single Ions, in: Report on a Conference on the Strength of Solids (Physical Soc., London, 1948) p. 75.
[18] C. Herring, J. Appl. Phys. 21 (1950) 437.
[19] H.E. Exner and P. Bross, by Acta Met. 27 (1979) 1007.
[20] P.G. Shewmon, Diffusion in Solids (McGraw-Hill, New York, 1963).
[21] J.W. Cahn, Acta Met. 28 (1980) 1333.

[22] C.A. Handwerker, Diffusion Induced Grain-Boundary Migration (DIGM) in Thin Films, in: Diffusion Phenomena in Thin Films, Eds. D. Gupta and P.S. Ho (Noyes, 1986).
[23] J.M. Blakely, Introduction to the Properties of Crystal Surfaces (Pergamon, New York, 1973).
[24] J.M. Dynys, Sintering Mechanisms and Surface Diffusion for Aluminum Oxide, ScD Thesis, Massachusetts Institute of Technology (1982).
[25] G.C. Kuczynski, L. Abernethy and J. Allen, Sintering Mechanism of Aluminium Oxide, in: Kinetics of High Temperature Processes, Ed. W.D. Kingery (MIT Press, Cambridge, MA, 1959) p. 163.
[26] R.L. Coble, J. Am. Ceram. Soc. 41 (1958) 55.
[27] W.D. Kingery and B. Francois, The Sintering of Crystalline Oxides, I. Interaction Between Grain Boundaries and Pores, in: Sintering and Related Phenomena, Eds. G.C. Kuczynski, N. Hooten and C. Gibben (Gordon and Breach, New York, 1967) p. 471.
[28] C. Herring J. Appl. Phys. 21 (1950) 301.
[29] D.W. Ready, J. Am. Ceram. Soc. 49 (1966) 366.
[30] R.M. Cannon, Diffusional Creep and Grain Boundary Sliding in Al_2O_3, ScD Thesis, Massachusetts Institute of Technology (1975).
[31] R. Gordon, Ambipolar Diffusion and its Application to Diffusional Creep, in: Mass Transport Phenomena in Ceramics, Eds. A.R. Cooper and A.H. Heuer (Plenum, New York, 1975) p. 445.
[32] R.M. Cannon and R.L. Coble, Review of Diffusional Creep of Al_2O_3, in: Deformation of Ceramic Materials, Eds. R.E. Tressler and R.C. Bradt (Plenum, New York, 1975) p. 61.
[33] J.E. Blendell and R.L. Coble, Effect of Heating Rate on the Interpretation of Initial Sintering Data, presented at 81st Meeting Am. Ceram. Soc., 1979, paper 54-b-79; Am. Ceram. Soc. Bull. 58 (1979) 342.
[34] M.A. Spears and A.G. Evans, Acta Met. 30 (1982) 1281.
[35] F.A. Nichols and W.W. Mullins, Trans. AIME 233 (1965) 1840.
[36] F.A. Nichols, J. Mater. Sci. 11 (1976) 1072.
[37] M.F. Yan, R.M. Cannon and H.K. Bowen, Grain Boundary Migration in Ceramics, in: Ceramic Microstructures '76, Eds. R.M. Fulrath and J.A. Pask (Westview, Boulder, CO, 1977) p. 276.
[38] S.M. Allen and J.W. Cahn, Acta Met. 27 (1979) 1085.
[39] G.S. Grest, D.J. Srolovitz and M.P. Anderson, Acta Met. 33 (1985) 499.
[40] A.E. Paladino and W.D. Kingery, J. Chem. Phys. 37 (1962) 957.
[41] Y. Oishi and W.D. Kingery, J. Chem. Phys. 33 (1960) 480.
[42] F.A. Nichols, J. Nucl. Mater. 30 (1969) 148.
[43] R.J. Brook, J. Am. Ceram. Soc. 52 (1969) 56.
[44] C.A. Handwerker, R.M. Cannon and R.L. Coble, Final-Stage Sintering of MgO, in: Structure and Properties of MgO and Al_2O_3 Ceramics, Ed. W.D. Kingery (Am. Ceram. Soc., Columbus, OH, 1985) p. 619.
[45] C. Zener, private communication to C.S. Smith, Trans. AIME 175 (1948) 15.
[46] C.H. Hsueh, A.G. Evans and R.L. Coble, Acta Met. 30 (1982) 1269.
[47] C.A. Handwerker, J.M. Dynys, R.L. Coble and R.M. Cannon, J. Am. Ceram. Soc., submitted.
[48] W.C. Mackrodt, Calculated Point Defect Formation, Association, and Migration Energies in MgO and Al_2O_3, in: Structure and Properties of MgO and Al_2O_3 Ceramics, Ed. W.D. Kingery (Am. Ceram. Soc., Columbus, OH, 1985) p. 62.
[49] K.L. Kliewer and J.S. Koehler, Phys. Rev. 140 (1965) A1226.
[50] J.R. Booth, W.D. Kingery and H.K. Bowen, J. Crystal Growth 29 (1975) 257.
[51] R.C. Roman, J.B. Barr, R.N. McNally and A.M. Alper, J. Am. Ceram. Soc. 46 (1963) 313.
[52] A.M. Alper, R.N. McNally, P.G. Ribbe and R.C. Doman, J. Am. Ceram. Soc. 45 (1962) 263.
[53] A.F. Henriksen and W.D. Kingery, Ceramurgia Intern. 5 (1979) 11.
[54] P.W. Tasker, E.A. Colbourn and W.C. Mackrodt, J. Am. Ceram. Soc. 68 (1985) 49.
[55] B.A. Bender, D.B. Williams, and M.R. Notis, J. Am. Ceram. Soc. 63 (1980) 149.
[56] Y.M. Chiang, A.F. Henriksen and W.D. Kingery, J. Am. Ceram Soc. 64 (1981) 385.
[57] D.R. Clarke, J. Am. Ceram. Soc., submitted.
[58] S.K. Roy and R.L. Coble, J. Am. Ceram. Soc. 51 (1968) 1.
[59] W.S. Coblenz and C.A. Handwerker, Shrinkage of a Grain with Segregated Solute, presented at Am. Ceram. Soc. Fall Meeting, Basic Science Division, 1984, paper 42-B-84P; Am. Ceram. Soc. Bull. 63 (1984) 933.
[60] (a) W.C. Mackrodt and R.F. Stewart, J. Phys. C12 (1979) 431;
(b) W.C. Mackrodt and R.F. Stewart, J. Phys. C12 (1979) 5015.
[61] C.R.A. Catlow, R. James, W.C. Mackrodt and R.F. Stewart, Phys. Rev. B25 (1982) 1006.
[62] C.R.A. Catlow and W.C. Mackrodt, Eds., Computer Simulation in Solids (Springer, Berlin, 1982).
[63] F.A. Kröger and H.J. Vink, Relations Between Concentrations of Imperfections in Crystalline Solids, in: Solid State Physics, Vol. 3, Eds. F. Seitz and D. Turnbull (Academic Press, New York, 1956) p. 307.
[64] E.A. Colbourn and W.C. Mackrodt, Point Defects and Chemisorption at the {100} Surface of MgO, in: Structure and Properties of MgO and Al_2O_3 Ceramics, Ed. W.D. Kingery (Am. Ceram. Soc., Columbus, OH, 1985) p. 190.
[65] J.M. Vieira and R.J. Brook, Lattice-, Grain Boundary, Surface-, and Gas Diffusion Constants in Magnesium Oxide, in: Structure and Properties of MgO and Al_2O_3 Ceramics, Ed. W.D. Kingery (Am. Ceram. Soc., Columbus, OH, 1985) p. 438.
[66] I.K. Lloyd and H.K. Bowen, J. Am. Ceram. Soc. 64 (1981) 744.

[67] M.M. El-Ariat, L.D. Hou, S.K. Tiku, H.A. Wang and F.A. Kröger, J. Am. Ceram. Soc. 64 (1981) 174.
[68] C. Monty and J. LeDuigou, High Temp. High Pressure 14 (1982) 709.
[69] R.W. Balluffi, P.D. Bristowe and C.P. Sun, J. Am. Ceram. Soc. 64 (1981) 23.
[70] A.M. Stoneham, J. Am. Ceram. Soc. 64 (1981) 54.
[71] M.P. Tosi, Cohesion of Ionic Solids in the Born Model, in: Solid State Physics, Vol. 16, Eds. F. Seitz and D. Turnbull (Academic Press, New York, 1964) p. 1.
[72] P.W. Tasker, Phil. Mag. A39 (1979) 119.
[73] P.W. Tasker and T.J. Bullough, Phil. Mag. A43 (1981) 313.
[74] J.W. Gibbs, The Scientific Papers of J. Willard Gibbs (Dover, New York, 1961; reprinted by Peter Smith Co., 1983).
[75] J.J. Gilman, J. Appl. Phys. 31 (1960) 3208.
[76] R.M. Cannon, T.D. Ketcham and T.W. Coyle, Toughened Optical Materials, in: Emerging Optical Materials, Ed. S. Musikant (SPEI, Bellingham, WA, 1982) p. 173.
[77] J.J. Duga, Surface Energy of Ceramic Materials, DCIC Report 69-2 Battelle Memoral Laboratories, Columbus, OH (1969).
[78] M.R. Welton-Cook and W. Berndt, J. Phys. C15 (1982) 5691.
[79] P.W. Tasker, Surfaces of Magnesia and Alumina, in: Structure and Properties of MgO and Al_2O_3 Ceramics, Ed. W.D. Kingery (Am. Ceram. Soc., Columbus, OH, 1985) p. 176.
[80] C.Y. Wang, M.P. Harmer and Y.T. Chou, J. Am. Ceram. Soc., submitted.
[81] H. Kamizono and K. Hamano, Yogyo Kyokai Shi 86 (1978) 476.
[82] D.M. Duffy and P.W. Tasker, Properties of Grain Boundaries in Rock Salt Structured Oxides, in: Structure and Properties of MgO and Al_2O_3 Ceramics, Ed. W.D. Kingery (Am. Ceram. Soc., Columbus, OH, 1985) p. 275.
[83] D. Wolf, Comparison of the Calculated Properties of High-Angle (001) Twist Boundaries in MnO, FeO, CoO and NiO with MgO, in: Structure and Properties of MgO and Al_2O_3 Ceramics, Ed. W.D. Kingery (Am. Ceram. Soc., Columbus, OH, 1985) p. 290.
[84] D. Wolf, J. Am. Ceram. Soc. 67 (1984) 1.
[85] P. Chaudhari and J.W. Matthews, J. Appl. Phys. 42 (1971) 3063.
[86] P. Chaudhari and J.W. Mathews, Appl. Phys. Letters 17 (1970) 115.
[87] P. Chaudhari and H. Charbnau, Surface Sci. 31 (1972) 104.
[88] R.R. Cowley, R.L. Segal, R.St.C. Smart and P.S. Turner, Phil. Mag. A39 (1979) 163.
[89] (a) C.P. Sun and R.W. Balluffi, Phil. Mag. A46 (1982) 49;
(b) C.P. Sun and R.W. Balluffi, Phil. Mag. A46 (1982) 63.
[90] (a) W.D. Kingery, J. Am. Ceram. Soc. 57 (1974) 1;
(b) W.D. Kingery, J. Am. Ceram. Soc. 57 (1974) 74.
[91] C.W. Li and W.D. Kingery, Solute Segregation at Grain Boundaries in Polycrystalline Al_2O_3, in: Structure and Properties of MgO and Al_2O_3 Ceramics, Ed. W.D. Kingery (Am. Ceram. Soc., Columbus, OH, 1985) p. 368.
[92] J.R.H. Black and W.D. Kingery, J. Am. Ceram. Soc. 62 (1979) 176.
[93] W.D. Kingery, T. Mitamura, J.B. Vander Sande and E.L. Hall, J. Mater. Sci. Letters 14 (1979) 1766.
[94] (a) M.F. Yan, R.M. Cannon and H.K. Bowen, J. Appl. Phys. 54 (1983) 764;
(b) M.F. Yan, R.M. Cannon and H.K. Bowen, J. Appl. Phys. 54 (1983) 779.
[95] S. Baik, D.E. Blakely and R. Raj, J. Am. Ceram. Soc. 68 (1985) 225.
[96] L.E. Murr, R.J. Horylev and G.I. Wong, Surface Sci. 26 (1971) 184.
[97] W.D. Kingery, J. Am. Ceram. Soc. 37 (1954) 42.
[98] D. Turnbull, Trans. AIME 191 (1951) 661.
[99] H. Gleiter, Acta Met. 17 (1969) 853.
[100] J.W. Cahn, Acta Met. 10 (1962) 789.
[101] K. Lucke and H.P. Stuwe, On the Theory of Grain Boundary Motion, in: Recovery and Recrystallization of Metals, Ed. L. Himmel (Gordon and Breach, New York, 1967) p. 171.
[102] A.M. Glaeser, H.K. Bowen and R.M. Cannon, J. Am. Ceram. Soc. 69 (1986) 119.
[103] R.A. Brown, J. Am. Ceram. Soc. 44 (1965) 483.
[104] T. Ikegama, I. Matsuda, Y. Morioyshi and H. Suzuki, J. Am. Ceram. Soc. 61 (1978) 532.
[105] (a) S.J. Bennison and M.P. Harmer, J. Am. Ceram. Soc. 66 (1983) C90;
(b) S.J. Bennison and M.P. Harmer, J. Am. Ceram. Soc. 68 (1985) C22.
[106] (a) P.J. Lemaire and H.K. Bowen, J. Am. Ceram. Soc. 65 (1982) 41;
(b) P.J. Lemaire and H.K. Bowen, J. Am. Ceram. Soc. 65 (1982) 49.
[107] R.L. Coble, J. Am. Ceram. Soc. 45 (1962) 123.
[108] M.P. Harmer, Use of Solid-Solution Additives in Ceramic Processing, in: Structure and Properties of MgO and Al_2O_3 Ceramics, Ed. W.D. Kingery (Am. Ceram. Soc., Columbus, OH, 1985) p. 679.
[109] M.P. Harmer and R.J. Brook, J. Mater. Sci. 15 (1980) 3017.

Diffusion-Induced Grain Boundary Migration in Ceramics

M.D. Vaudin, J.E. Blendell and C.A. Handwerker

Material Science and Engineering Laboratory
National Institute of Standards and Technology
Gaithersburg, MD 20899

Abstract

High stresses at grain boundaries and surfaces are produced by diffusion of solutes into polycrystalline materials where the lattice parameters of the solution vary with solute concentration. When $D_{gb} >> D_{lattice}$ boundaries may migrate in response to these stresses. Recent observations of diffusion-induced grain boundary migration in the Al_2O_3/Cr_2O_3 system using optical, SEM and TEM techniques are discussed in terms of the coherency strain theory in which boundary migration is driven by the elastic energy produced by solute diffusion.

Introduction

Diffusion-induced grain boundary migration (DIGM) is one of many phenomena that may occur during diffusion of a solute in a polycrystalline material. In diffusion regimes where there is substantial solubility of the diffusing species and the lattice parameters of the solid solution vary with composition, high stresses can develop at grain boundaries, particularly when lattice diffusion is orders of magnitude slower than grain boundary diffusion. The grain boundaries may migrate in response to these stresses; such migration frequently produces characteristic "wavy" boundary morphologies. Diffusion-induced grain boundary migration has been observed in many metal systems and a smaller number of ceramic and semiconductor systems. Liquid film migration (LFM) is a similar phenomenon in which there is a film of liquid between two grains and the film migrates as a result of diffusion and stress generation in the grains next to the liquid film. These subjects have been extensively reviewed by Handwerker (1) and King (2).

In the coherency strain model of DIGM, migration is induced by differences in strain energy across the boundary. The strain arises from the change in lattice parameter with composition, q. In cubic materials, the strain, δ, in the grain boundary plane is given by:

$$\delta = (a(q_b)-a(q_o))/a(q_o) = \eta(q_b - q_o) \qquad (1)$$

where $a(q_b)$ is the lattice parameter at the composition q_b in the grain boundary plane and q_o is the composition of the original material. The second equation assumes that da/dq is constant (Vegard's Law) such that $\eta = (1/a(q_o))da(q))/dq$; typically this is a valid assumption for small concentration changes. If the solid solution is constrained to remain coherent with the bulk material, the grain boundary layer will increase its energy by the coherency strain energy, which is given by:

$$f_{coherent} = Y(n)\delta^2 \qquad (2)$$

where Y(n) is an orientation dependent elastic modulus with extrema at <100> and <111>. For the two grains either side of an asymmetric grain boundary, Y(n) will be different leading to a driving force for migration of the boundary. For non-cubic materials, η and $D_{lattice}$ are both tensor properties so that the elastic strains and solute profiles on either side of a boundary may differ. The elastic energy density is a complex function of material properties and grain misorientation. However, for any crystal class, solute diffusion leads to an energy increase in the system if there is a solute-induced lattice parameter change, and the energy <u>difference</u>, E_{diff}, across the boundary between the grains produces a driving force for migration of the boundary. If the migrating boundary has non-zero curvature, K, E_{diff} will contain an additional term which, for migration away from the center of curvature, is $-2\gamma K$ where γ is the grain boundary energy. When migration forms "wavy" boundaries, the magnitude of the curvature term increases with increasing migration distance; when the curvature and coherency strain terms cancel, $E_{diff} = 0$, and migration ceases. Song, Ahn and Yoon (3) in LFM experiments in the W-Ni-Fe system measured the curvature at which the migration direction reverses, i.e. the maximum curvature, and found it to be the right order of magnitude for cancelling the effect of coherency stress. The coupled diffusion and migration cause compositional changes in regions swept by the boundaries, and the resultant change of lattice parameter causes the alloyed regions to lose coherence with their parent grains when the boundary has migrated beyond a critical distance.

In this paper observations of DIGM in the alumina/chromia system using TEM and SEM techniques will be described and discussed in the light of the coherency strain theory. Migration of boundaries up to 10 μm has been observed in specimens of alumina (with MgO added as a sintering aid) exposed to chromia vapor at 1500°C. This migration is a near surface phenomenon occurring in the top 5 to 10 μm of the specimen. The temperature range of interest (1200°C to 1550°C) is well away from both the solidus ($T_m(Al_2O_3)$ = 2045°C) and the miscibility gap which exists below 950°C. This system was examined earlier by the authors at lower temperatures where no migration was observed and its reexamination was prompted by a private communication from D.N. Yoon who observed DIGM in the alumina-chromia oxide scale formed on stainless steel.

Experimental

Slices of alumina 6 mm square were cut from a bar and polished to a 1 μm diamond finish. For each DIGM experiment, one polished slice was suspended on spacers of the same alumina above a bed of chromia powder in an alumina boat and the system was isolated with another alumina boat and an alumina crucible as shown in Fig. 1. A total of 12 DIGM experiments were carried out at temperatures of 1300°C to 1550°C; the times at these temperatures varied from 30 to 120 minutes. One feature of the experimental set-up that proved useful when observing the DIGM was that part of each specimen was "shaded" from direct unimpeded exposure to the chromia vapor by being placed over the alumina spacer, and developed a different surface morphology from the "unshaded" parts of the specimen, as will be described below.

After heat treatment the specimens were examined using optical microscopy and SEM. Parts of each specimen were then polished using 0.25 μm diamond paste and 0.05 μm alumina powder to remove the layer of chromia that was deposited on the surface of most of the specimens and the specimens were again examined optically and in the SEM. The crystallographic orientation of some surface features of the specimens was determined with an electron back scatter pattern (EBSP) detector and analyzer in the SEM (4). One specimen (1550°C/0.5 hr) was thinned to electron transparency by dimpling and ion-milling from the back side, and was then examined in the TEM.

Observations

Grain surfaces

In all 12 DIGM experiments, the morphology of the surface of the specimens changed as the chromia vapor condensed on the alumina grain surfaces. It was clear that the grain surface morphologies depended on the duration and temperature of the experiment and also on whether the grains were in a shaded or unshaded part of the specimen. In addition, since in some specimens adjacent grains have markedly different appearances, it was inferred that grain orientation affected the surface morphology. Fig. 2 is a SEM micrograph from the unshaded region of the 1500°C/1 hr specimen and demonstrates significant variation in grain surface morphology: facetting is not observed, but the grain surfaces are no longer planar but "rumpled"; the wavelength and amplitude of the morphological instability varies from grain to grain; the morphologies in some grains appear to be crystallographically aligned.

For short times and lower temperatures SEM and EDS observation showed that a chromia-rich deposit formed on the surface in the form of hemispherical islands which for some grain orientations remained isolated and in other cases joined to form a complete layer. From EBSP observations of grains where the chromia coverage was incomplete it was determined that the chromia-rich islands were epitactic with the alumina substrate. The curvature (K) of the lattice planes in the islands was about 20 μm^{-1}, implying a dislocation density (K/b) of the order of 10^{10} cm^{-2}. In extreme cases, particularly in the shaded region of the specimen, many grains remained flat and had light contrast in secondary electron SEM images, and EDS detected little or no Cr_2O_3 at the surface. Since chromia is at least 10 orders of magnitude higher in electrical conductivity than alumina, light contrast in the SEM correlates with chromia depletion. For the 1300°C/1 hr specimen, the misorientation between the specimen normal and the c-axis for several grains was measured using EBSP's and correlated with the appearance of the grain (see Table 1). It can be seen that the closer the grain surface was to basal orientation, the more likely it was to be of light contrast. The optical micrograph in Fig. 3(a) which is from a shaded region of the 1500°C/2 hr specimen shows that in the flat grains residual scratches from the polishing have become decorated with chromia.

Grain Boundaries

In the as-treated specimens there is clear evidence of DIGM in specimens heated to 1400°C or higher, particularly in the shaded regions of the specimens. In Fig. 3(a), some of the grains have remained flat and significant migration (up to 10 μm) has occurred, particularly into the flat grains; grain boundaries between "rumpled" grains have migrated less suggesting that in the surface layer the solution of chromia and/or the development of the rumpled morphology tend to suppress DIGM. The migrated boundaries are in most cases extremely facetted with a lath-like appearance. From EDS spectra the migrated grain boundary regions have chromia concentrations of 10%-15% and the flat grains have essentially 0% Cr_2O_3. An unshaded area from the same specimen (Fig. 3(b)) has a completely different appearance. All the grains have rumpled surfaces and the wavelengths of the surface morphologies are longer than the rumpled grains in Fig. 3(a). Evidence of DIGM is less clear and where it can be seen (at arrowed positions) it appears that chromia has plated over the surface after the migration stopped. The grain boundary regions in this specimen have greater than 60% Cr_2O_3 and the grains have about 30%. It should be born in mind that the generation volume for x-rays at this voltage (20 KeV) extends to at least 1 μm in depth and therefore an EDS spectrum represents a weighted average over this depth. The profiles of chromia concentration in these various areas are the result of simultaneous deposition and diffusion of chromia accompanied, in the grain boundary regions, by grain boundary migration; thus the profiles are expected to vary with depth.

After polishing the specimens to remove the surface layer of nearly pure chromia, optical and scanning microscopy showed that the boundary migration penetrated below the surface layer, producing the same facetted interface morphology. Fig. 4(a) is an optical micrograph of the 1550°C/1 hr specimen and shows that in the regions where the chromia layer has been completely removed, the areas over which the grain boundaries have migrated are lighter than the surrounding grains. This is in contrast to the regions in which the grains are chromia-rich and are lighter than the grain boundaries. Evidently, the reflectivity of a chromia/alumina solid solution is proportional to chromia content which correlates with the electrical conductivity of chromia being much higher than that of alumina. In the SEM the contrast is reversed as described above, and a SEM image of the polished surface of the 1550°C/0.5 hr specimen (Fig. 4(b)) shows the migration regions as darker than the grains. The micrographs in Figs. 3 and 4 indicate that the migration distance varies from boundary to boundary. Migration distances were measured for 4 specimens: 1400°C/0.5 hr, 1400°C/2 hr, 1500°C/0.5 hr and 1500°C/2 hr. The boundaries fell into two categories, those where the migration distance was relatively uniform along the length of the boundary and those where there was significant variation in distance (by factors of 2 or 3 in some cases). The data for the boundaries with uniform migration are presented in Table 2.

TEM observations of a thin foil taken from the 1550°C/0.5 hr specimen revealed many of the classic features of DIGM. Almost all the boundaries observed had migrated and some grain boundaries had migrated in both directions. Close to the original positions of the grain boundaries there was, in most cases, an array of dislocations across which there was no detectable misorientation. However, EDS analysis showed that between these dislocations and the current position of the grain boundary there was from 1% to 3% Cr_2O_3 dissolved in the Al_2O_3, suggesting that these were misfit dislocations accommodating the change in alumina lattice parameters caused by the solute. Fig. 5 is a bright field image of the corner of a grain where the grain boundaries have migrated from 0.8 to 1.2 μm away from the center of the strongly diffracting grain. The interface between the pure and alloyed alumina is clear both from the misfit dislocations which run from the top to bottom surfaces of the foil (and are close to end on in the micrograph) and also from the complex distribution of fringes which are particularly visible in the boundary on the left of the micrograph. The misfit dislocations in this boundary appear to be of two different types with two different line directions. One type is regularly arranged at the interface whereas only one of the other type (which are in the minority) has incorporated into the interface structure, where it is associated with a step. The chromia concentration in the alloyed region of boundary A is 1.8% and the average dislocation spacing is 0.45 μm. The average dislocation spacing and chromia concentration in a total of five boundaries was measured and these data are summarized in Table 3.

Discussion

These observations of DIGM in the alumina/chromia system are similar to observations in metal systems such as Au/Ag. The most obvious differences lie in the extremely facetted, finger-like nature of the morphology that is created by the DIGM, and the surface rumpling that occurred in all the experiments. The observations of surface rumpling that vary as a function of temperature, orientation and solute supply (shaded or unshaded) all point to a nucleation and growth mechanism of epitaxy with the density of nucleation

sites being a function of surface orientation. Surface diffusion and vapor transport in this system are very rapid at these temperatures such that a radical of CrO^+ or CrO_2^- condensing on the alumina surface will rapidly diffuse to a site of low energy such as a surface step, scratch, pre-existing epitaxial island, grain boundary or dislocation.

The tendency of both free surfaces and grain boundaries in ceramics to be facetted has been noted by several authors (5, 6). The surface morphologies developed here are not equilibrium shapes as the surface layer is thickening and changing its stress state throughout the experiment. Hence the regular surface facetting observed in, for example, equilibrated NiO/MgO solid solutions (5) is not expected here. In contrast to surface morphologies, the TEM observations presented here do not show facetting of the grain boundaries; this difference in facetting is likely to be because the TEM foil is from several microns below the original specimen surface, although the exact depth is not known.

The variation of average migration distance with time and temperature has the expected trends: increasing the temperature or time increases the migration distance. For each experiment some migration may have occurred as the specimen was heated to the experimental temperature, but after allowing for this effect, the data in Table 2 show that migration at the surface is not linear with time. The coherency strain theory only predicts a constant migration rate if there is no change in grain boundary length and no change in curvature. When the curvature is changing and the grain boundary length is increasing, the rate should decrease with time.

As discussed above, the driving force for DIGM for the non-cubic crystal classes is a complex issue. An algorithm to calculate the driving force as a function of boundary normal, solute concentration, diffusion tensor and distortion tensor for any crystal class has been developed and will be published soon. The elastic energy density $f_{coherent}$ can be expressed as $A(q - q_o)^2$, where A is dependent on boundary normal. Symmetry arguments show that for alumina/chromia, which is rhombohedral, A is the same for all prismatic planes since the diffusion tensor and the distortion tensor are isotropic for boundary normals in the basal plane. At room temperature, for prismatic planes $A = 1.10\ GJm^{-3}$ and for the basal plane $A = 1.01\ GJm^{-3}$; the difference of $900\ MJm^{-3}$ indicates that considerable driving forces for boundary migration can be developed. Anisotropy of diffusion may be a significant factor in determining the size of the driving force since changes in solute concentration are squared in the expression for $f_{coherent}$.

In the simplest analysis, the solute-induced elastic strain is approximately ηq, where η is the average of the distortion tensor η_{11}, η_{22} and η_{33}. For alumina/chromia $\eta_{11} = \eta_{22} = 0.041$ and $\eta_{33} = 0.049$ and $\eta = 0.044$. A solute concentration of q in the basal plane produces a stress of Aq/η_1, which for $q = 0.03$ gives a stress of 680 MPa. Such a high stress will lead to the formation of dislocations to relieve the stress when the depth of the diffusion zone is greater than a certain critical layer thickness (7). Dislocation generated due to diffusion have been observed in TEM. Because the boundary planes in the TEM foil studied are approximately perpendicular to the plane of the foil, and the dislocation spacings are small compared to the foil thickness, only a limited portion of each misfit dislocation network is visible. In addition the line directions of the dislocations are typically normal to the foil which is an unfavorable orientation for Burgers vector determination. However, correlations have been made between the data in Table 3 on misfit dislocation spacing D and solute concentration q in the alloyed region. We can make two assumptions: (1) that this elastic strain is <u>all</u> relieved by dislocations; and (2) the Burgers vectors of these dislocations

are parallel to the grain boundary plane and have magnitude b. Based on these assumptions, the magnitude of b is given by $b = D\eta q$. Calculated values of b are listed in Table 3 and should be compared with the two smallest Burgers vectors in alumina, $1/3\langle 2\bar{1}\bar{1}0\rangle$ and $1/3\langle 1\bar{1}00\rangle$, with magnitudes 4.76 Å and 5.12 Å respectively. If the relief of elastic strain is incomplete, the calculated b will be greater than these values; and if the Burgers vectors are not parallel to the interface the calculated b will be less than these values. The degree of agreement between calculated and allowed values of b is within 20% which is good. The misfit dislocations in boundary A of Fig. 5 are arranged in facets and steps as described above. Analysis of the relationship between the grain boundary plane and facetting of misfit dislocation arrays is the subject of future work and will not be discussed further here.

Acknowledgements

We gratefully acknowledge useful discussions with Dr. W. Craig Carter and partial financial support from the Office of Naval Research.

References

1. C.A. Handwerker in "Diffusion Phenomena in Thin Films and Microelectronic Materials", Noyes Publication, Park Ridge, NJ, 1988, edited by D. Gupta and P. Ho, 245-322.

2. A.H. King, Int. Mater. Revs. 32, 173-?? (1987).

3. Song, Y. D., Ahn, S. T., and Yoon D. N., Acta Metall. 33 1907-1910 (1985).

4. D.J. Dingley, Scanning Electron Microscopy (USA) Part 2, 569-575 (1984).

5. C.A. Handwerker, M.D. Vaudin and J.E. Blendell, J. De Physique, 49[C5,#10], 367-373 (1988).

6. M.D. Vaudin, M. Rühle and S.L.Sass, Acta Metall. 31, 1109-1116 (1983).

7. W.A. Jesser and D. Kuhlmann-Wilsdorf, Phys. Stat. Sol. 19, 95-105 (1967).

Figure Captions

1. Experimental set-up showing specimen suspended above bed of chromia powder

2. SEM micrograph of unshaded region of 1500°C/1 hr specimen showing variation of surface morphology between grains

3(a) Optical micrograph of shaded region of 1500°C/2 hr specimen showing finger-like morphology of migration and decorated scratches

3(b) Optical micrograph of unshaded region of 1500°C/2 hr specimen showing different surface morphology from 3(a) because of extensive plating on of chromia

4(a). Optical micrograph of 1500°C/1 hr specimen after polishing

4(b). SEM micrograph of 1550°C/0.5 hr specimen

5. TEM micrograph of 1550°C/0.5 hr specimen

Table I

SURFACE BRIGHTNESS FOR DIFFERENT SURFACE NORMALS

1300°C - 1 hr.

Surface Normal Angle Relative to [0001]	Brightness
35.5°	Bright
39.9°	Bright
17.5°	Bright
11.9°	Bright
29.7°	Bright
38.2°	Dark
57.61°	Dark
85.9°	Dark
87.6°	Dark
67.7°	Dark
43.3°	Dark

1300°C - 2 hr.

20.2°	Bright
10.1°	Bright
12.3°	Bright
79.1°	Dark

Table II

Migration distances as a function of time and temperature

	0.5 hrs	2 hrs
1500°C	3.4 μm	4.9 μm
1400°C	1.9 μm	3.0 μm

Table III

MISFIT DISLOCATION SPACING

D:-Spacing (nm)	q:-Cr_2O_3 Concentration	b:-Burgers vector (nm)
480	0.027	0.58
460	0.018	0.38
620	0.020	0.55
440	0.030	0.59
560	0.030	0.38

Fig. 1

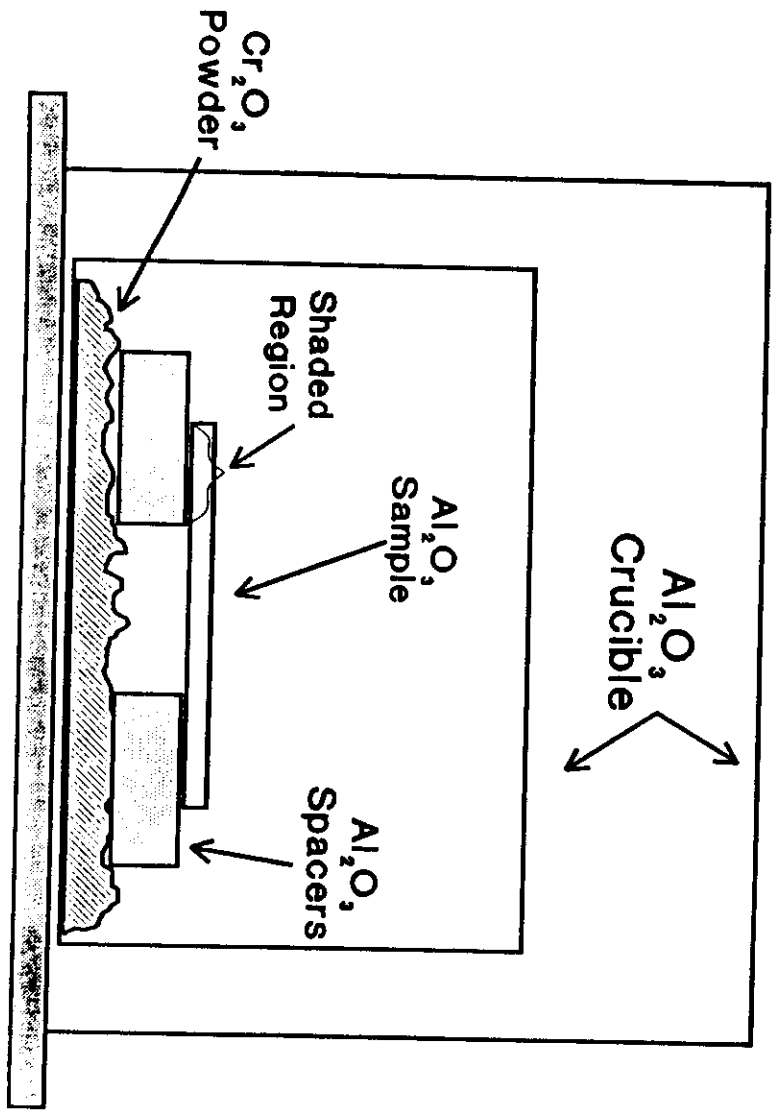

1500°C - 120 mins

Fig 3(a)

1500°C - 120 mins

Fig 3(b)

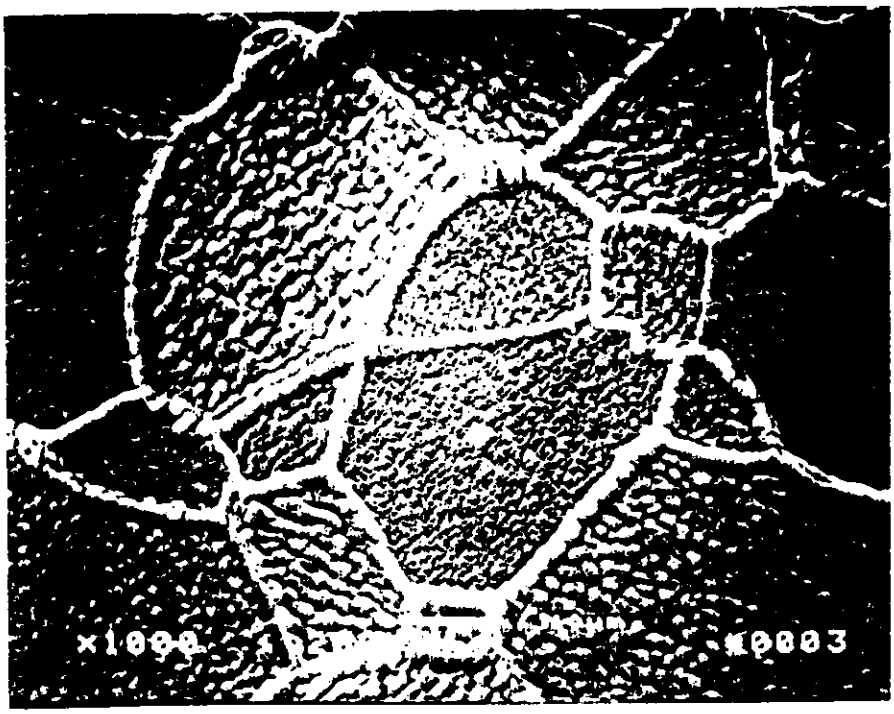

AC.3 7/n(a0 (3)

AC. 1 polished 7/17/90

(a)

AC.2 7/31/90

(b)

Reprinted from Ceramic Transactions, Vol. 7, 1990

Migration of Sapphire Interfaces into Vitreous Bonded Aluminum Oxide

Y. Finkelstein
Rafael Laboratories
Haifa, Israel

S.M. Wiederhorn, B.J. Hockey, C.A. Handwerker and J.E. Blendell
National Institute of Standards and Technology
Gaithersburg, MD 20899

ABSTRACT

Grain boundary migration in aluminum oxide at 1600°C was investigated by sintering together alternating plates of presintered polycrystalline alumina and sapphire. Two types of vitreous bonded alumina and two orientations of sapphire, {0001} and {11$\bar{2}$0}, were used in this study. A comparison of the mobility of these two planes at 1600°C showed the (11$\bar{2}$0) plane (normal to the a-axis) to have at least 3 times the mobility of the (0001) plane (normal to the c- axis). A-axis oriented sapphire did not advance through the alumina in a uniform manner; instead, the advancing interface was very irregular. Droplets of glass, spinel particles and sometimes grains of aluminum oxide were entrapped within the sapphire after the front had passed. By contrast, c-axis oriented sapphire tended to remain flat as it advanced through the alumina. The kinetics of migration are interface controlled, and the morphologies of the advancing sapphire interface are rationalized in terms of interfacial attachment kinetics, the composition of the intergranular glass phase, and interfacial surface energies of the sapphire plane relative to the average surface energy of the aluminum oxide grains in the alumina.

INTRODUCTION

The kinetics of grain boundary migration in Al_2O_3 have been examined by several researchers using measurements of the growth of a large grain, resulting either from discontinuous grain growth or the deliberate addition of a single crystal, into a fine-grained matrix [1-7]. From the change in migration distance of the large grain with time, a "grain boundary" velocity is calculated, which after adjustment for the change in grain size with time, and, yields a grain bounary mobility. From this mobility parameter, effects of composition and temperature are then analyzed. In Al_2O_3, the calculated mobilities vary by over three orders of magnitude for nominally similar compositions. As demonstrated by Kaysser et al. [6] and Handwerker et al. [7], two of the factors leading to this large variation in mobility are a dependence of the growth kinetics on crystal plane and chemical composition. In particular, Kaysser et al. found that the growth rate of large single crystal spheres into a fine- grained Al_2O_3 matrix containing an anorthite-based glass is orientation dependent, with growth in the ⟨0001⟩ slowest relative to all other directions. For this material, basal facets formed on grains that were wet by continuous liquid films. Even in MgO-doped alumina, where no liquid phase was observed, the growth rate was also a function of the crystallographic orientation of the single crystal sphere.

In this study, model crystal growth experiments were performed on Al_2O_3 to separate effects of crystal growth anisotropy from effects of the chemical composition. Growth rates of single crystals into a fine grained matrix of Al_2O_3 were measured with either the a- axis or the c-axis orientation of the single crystals normal to the interface. In the part of the study reported here, two commercial grades of Al_2O_3 were used as the fine-grained matrix. Fine grain aluminum oxides prepared under clean room conditions were also investigated, but will be reported elsewhere. Results are discussed with regard to growth anisotropy and grain boundary mobility of aluminum oxide.

EXPERIMENTAL PROCEDURE

Polished disks of dense alumina were placed in an alternating sequence with sapphire disks having either an a-axis or a c-axis normal to the growth interface, according to the geometry shown in Fig.1. The microstructures of the two grades of alumina are shown in Fig.2. One of the grades, Coors AD96 (Fig.2a), contained ≈ 96 wt% aluminum oxide and ≈ 8 vol% glass; the grain size was ≈8 μm. The total chemical composition of the AD96 alumina determined by induction coupled plasma emission spectroscopy (ICPES) for the major elements in wt% is: Ca, 0.13; Fe, 0.026; Mg, 0.45; Na, 0.2; Si, 0.96; Li, 0.015; K, 0.018. For minor elements, the composition in ppm by weight is: B, 7.4; Ba, 64; Ga, 66.5; Mn, 7.9; Sr, 11; Ti, 60; Zn, 35; and Zn, 30. At the temperatures used for the present study, 1600°C, glass wetted all of the grain boundaries and grains of alumina that were bounded by glass were frequently facetted. From an earlier study of the as-received material [8], the glass composition (wt%) determined by quantitative EDS analysis was: SiO_2, 56.2; Al_2O_3, 25.9; MgO, 8.5; Na_2O, 5.1; CaO, 2.8; K_2O, 0.7; FeO, 0.9. $MgAl_2O_4$ grains are also present in the alumina. The amount of spinel in AD96 is estimated to be 1.5 wt% calculated from the ICPES analysis assuming that the MgO/SiO_2 ratio from the EDS glass analysis is correct. After heat treatment at 1600°C for 24 hours, the composition (wt%) of the glass was found to be: SiO_2, 52; Al_2O_3, 32; MgO, 12; CaO, 5.

The second commercial material, Friedrichsfeld FF-99 (Fig.2b), was a hot-pressed aluminum oxide containing ≈ 99 wt% aluminum oxide. The as-received grain size of this material was ≈3 μm. The chemical composition of Friedrichsfeld alumina by ICPES for major elements in wt% is: Ca, 0.076; Fe, 0.029; Mg, 0.19; Na, 0.029; and Si, 0.13. The composition for minor elements in ppm by weight is: B, 14; Ba, 42; Ga, 65; Li, 18; Mn, 4; Sr, 4.5; Ti, 40; Zn, 31; and K, 36. This material also contained grains of $MgAl_2O_4$ dispersed within the structure. Although examination by optical microscopy revealed little if any glassy phase within this alumina, high resolution transmission electron microscopy revealed glass pockets at many of the triple junctions and along many of the grain boundaries. No attempt was made to determine if all of the grain boundaries were wetted by the glass. From an analysis of the larger pockets of glass in the as-received material, the glass was close to an anorthite composition, $CaO{\cdot}Al_2O_3{\cdot}2SiO_2$, so that, although the material contained spinel crystals, the intergranular glass had no detectible MgO. The lack of MgO in the glass (detectable at a level of 0.1 wt%) implies that *before heat treatment*, the MgO is present in the FF99 as spinel at a concentration of 1.2 wt%. After heat treatment at 1600°C for 24 hours, EDS analysis did reveal the presence of MgO within the glass phase (composition in wt%: SiO_2, 48; Al_2O_3, 29; CaO, 16; MgO, 6) indicating dissolution of spinel during

[1] The use of brand names is not to be interpreted as an endorsement by N.I.S.T.

the migration experiments.

The sapphire and polycrystalline disks were polished plane and parallel with a mirror finish using the following sequence: 9μm diamond paste on a cast-iron lap wheel; 3μm diamond paste on a solder-faced polishing wheel; and 1μm diamond paste on a solder-faced polishing wheel. All disks were ultrasonically cleaned in a detergent and rinsed in alcohol between grit sizes. After polishing, the specimens were glued with nitrocellulose epoxy into a stack, which was then annealed in air at 1600°C. A light load, ≈0.1 MPa, was applied to the stack to maintain mechanical stability during the annealing treatment. Annealing periods ranged from 1 hr. to 69 hr. After annealing, the stack of disks was sectioned perpendicular to the original plane of the disks, and then polished to prepare specimens that could be examined by optical microscopy. Specimens for examination by transmission electron microscopy (TEM) were made from similar sections that had been reduced in thickness to ≈100 μm. Disks ≈3 mm in diameter were ultrasonically cut from the polished sections and were then thinned to electron transparency by standard ion milling procedures.

RESULTS

Optical examination of cross-sections obtained from stacked arrays clearly revealed the effect of annealing on the growth of sapphire into polycrystalline alumina. Figures 3 and 5 provide representative views of the overall morphology of sapphire intergrowth into the fine grained aluminas under different conditions, while Fig.4 summarizes migration rate data for a-axis and c-axis growth into AD96. In both Figs.3 and 5, the migration interface is clearly distinguished by virtue of relief-polishing of the polycrystalline alumina, while the original contact interface is marked by a roughly planar array of pores, now contained within the single crystal region. By inspection of Fig.3, it can be seen that over the range of annealing times used in this study substantial intergrowth of the sapphire occurs; migration distances are generally multiple grain diameters. Figure 3 also shows that while grain growth within AD96 occurs during annealing, changes in grain dimensions are relatively small, when compared to sapphire growth distances. Most importantly, Fig.3 illustrates the pronounced effect of growth orientation on the growth rate of sapphire into AD96. In this regard, comparison of either Figs.3a with 3c or 3b with 3d shows that under identical conditions growth

along the a-axis direction (⟨1120⟩) is significantly greater than that along the c-axis direction (⟨0001⟩).

In order to quantify the dependence of migration distance in AD96 on both time and orientation, the average migration distance, L_m, for both ⟨0001⟩ and ⟨11$\bar{2}$0⟩ orientations was measured after annealing for from 1 to 69 hours at 1600°C. The results are shown in Fig.4 where the total interface migration distance is plotted as a function of annealing time. As can be seen, data for both growth orientations can be fitted to a straight line in the log-log representation. On the basis of a linear least squares fit, the slopes (i.e. the power law time exponents) are 0.88 for a-axis growth and 0.995 for c-axis growth. Considering the experimental errors involved, the growth for both directions can be considered to increase linearly as the time, i.e. $L_m = At$. Note, however, that growth along the a-axis is roughly three times faster than that along the c-axis.[2]

Similar experiments aimed at quantifying the growth rates of sapphire into the second alumina, FF99, were terminated due to excessive grain growth and bubble formation accompanied by extensive cracking which led to non-reproducible results for annealing times greater than 24 hours. Nevertheless, a relative comparison of the a-axis and c-axis intergrowth into FF99 and AD96 after 24 hours at 1600°C can be made; these results are shown in Fig.5. While noting that a strict comparison is complicated by the fact that the two aluminas differ not only in glass phase composition but in volume fraction of glass and that abnormal grain growth has occurred in FF99, it was found that the rate of sapphire intergrowth along the a-axis direction was nearly the same for both aluminas (Figs.5a and b). In contrast, the rate of c-axis intergrowth into FF99 was only one third of the rate of intergrowth into AD96 (Figs.5c and d), or alternatively, only one-ninth the growth rate along the a-axis direction. These results strongly suggest that glass phase composition has a pronounced effect on migration rate, specifically by altering the effect of growth orientation.

In conjunction with the observed differences in growth rate for a-axis and c-axis growth, there is also a significant difference in the morphology of the growth interface for these two directions. In general, the c-axis growth interface was relatively flat, exhibiting large (greater than the grain size) planar

[2]The velocity ratio was determined at the midpoint of the data, ≈24 hr., in Fig.4.

regions (e.g. Figs.3c-d and 5c-d) separated by individual grains which were partially encapsulated inthe advancing sapphire. By contrast, the a-axis growth interface was wavy, with undulations occurring over multiple grain dimensions (e.g. Figs.3a-b and 5a-b). The thickness of the glass layer at the AD96/a-axis interface did vary from grain to grain, however, no correlation could be seen between the thickness of the glass layer and the growth rate. The thickness of the glass layer at growth interfaces was more uniform for c-axis oriented growth than for a-axis oriented growth. Regardless of sapphire orientation, there was no glass buildup between the growing sapphire anf the matrix grains suggesting that all of the glass within the AD96 is eventually trapped within the sapphire. Sometimes, long stringers of glass were left behind as the sapphire crystal grew into the polycrystalline matrix. These occur as a consequence of a growth instability of the sapphire-glass interface.

Detailed observations by transmission electron microscopy (TEM) further highlighted the difference in the morphology of the growth interfaces associated with growth along the c- and a-axis in sapphire. As illustrated in Fig.6, for most AD96 grain orientations, the advancing sapphire surface was planar on (0001), although steps of varying height, apparently corresponding to growth ledges were found at high magnification, Fig.6c. Typically, a narrow layer of glass, of the same composition as the binder glass in AD96, separated the sapphire and the matrix grains. Across the glassy layer, the grains adjacent to the growing sapphire were either planar, smoothly curved, or facetted (as in Fig.6b) depending upon their specific orientation or proximity to large glassy multi-grain junctions (Fig.6c). In regions where facetting of the AD96 grains was observed, the facet planes invariably corresponded to low index orientations in Al_2O_3 such as $\{0001\}$, $\{\bar{1}012\}$, $\{10\bar{1}1\}$, $\{11\bar{2}0\}$, and $\{11\bar{2}3\}$. Similar observations of facet planes were made earlier by Hanson and Phillips [9]. Further observations also showed that a non-planar interface in (0001) oriented sapphire occurred only when the orientation of the dissolving AD96 grains was also close to the (0001) basal orientation. These cases corresponded to the aforementioned partially encapsulated grains, which exhibited interfaces that were highly facetted with long basal ledges.

In contrast to the above description of c-axis sapphire, interfaces associated with the growth of a-axis oriented sapphire into AD96 were not planar, Fig.7. This is evidenced by large scale undulations along the interface and by the fact that the advancing sapphire surface is generally inclined in cross-section

views, Fig.7a. In general, the specific details of the interface separating the advancing a-axis sapphire from the dissolving AD96 grains varied considerably and was clearly dependent on the specific orientation of the adjacent AD96 grain, Figs.7b-d. As a consequence, the morphology of the glassy layer present at the interface also varied considerably. In this regard, a relatively thick layer of glass is seen in Fig.7b along that portion of the interface where the dissolving AD96 grain is planar along (0001), but is not apparent along the curved portion of the interface. Similarly, a glassy layer is not apparent along the highly irregular interfaces separating the advancing a-axis sapphire and the partially encapulated, tabular shaped grain in Fig.7c, but is clearly present at the portion of the growth interface seen in Fig.7d. While facetting of the AD96 grain surfaces and the a-axis sapphire surface was not uncommon, the development of larger planar $\{11\bar{2}0\}$ segments during a-axis growth, as seen in Fig.7d, was not typically observed.

Finally, X-ray energy dispersive analysis (EDS) was used in conjunction with either TEM or SEM to identify the nature of the entrapped inclusions in the intergrowth regions, Figs.3 and 5. While many of the features seen in these micrographs correspond to pores inherent to both types of aluminas, a large proportion were found to be glassy inclusions. The origin of these glassy inclusions apparently relates to instabilities along the advancing growth front due to the presence of large glassy pockets at multi-grain junctions in the aluminas, or to special orientation effects on the dissolution-precipitation process, as seen in Fig.7b. In addition to encapsulated pores and glass inclusions, crystalline inclusions are also found with the intergrowth regions (see e.g. Fig.5b). Most of these inclusions, were readily identified as the small (1 μm) grains of $MgAl_2O_4$ which are inherent to the microstructure of both AD96 and, more abundantly, FF96. Occasionally, however, encapsulated grains of Al_2O_3 were also found. Though rare and energetically unfavorable, the presence of Al_2O_3 grains undoubtedly relates to the strong effect of orientation and/or the thickness of an interfacial glassy layer on the local driving force for dissolution-precipitation as depicted in Figs.7b and c.

DISCUSSION

The major observations in this study are: (1) The average migration distance of the sapphire into the aluminas within experimental error increases linearly with time; (2) average growth rates depend on the orientation of the

sapphire seed crystal and on the composition of the surrounding glass; (3) facetting occurs at both growing and dissolving interfaces; (4) local growth depends on the orientations of both the growing and dissolving grains; and (5) growth results in the encapsulation of glass inclusions, and of $MgAl_2O_4$ and Al_2O_3 grains in the sapphire. We first discuss formulations of the driving force for the growth of a large grain into a fine grain matrix and how this driving force is affected by facetting of the grains in the matrix. Analogies are made between the growth of isolated facetted crystals from high temperature solutions and the growth of an assemblage of grains separated by liquid films. We then discuss effects of composition on growth rates and interface instability on liquid encapsulation.

The driving force for the migration of a large grain into a fine grain matrix is typically described in terms of the curvature of grain boundaries whose energies do not depend on crystal orientation [10]. Such isotropic grain boundaries are curved in a well prescribed way in order to balance the forces at intersections where three grains meet, i.e. the triple junctions. For a grain much larger than the average matrix grain size, the boundaries adjacent to the large grain will be curved, with the center of curvature lying outside the large grain. Because of surface tensions inherent in such a geometry, large grains will grow at the expense of the smaller ones, and the driving force for growth can be related uniquely to the grain size of the matrix. Assuming an average grain size, G, and an average mobility for the grain boundaries, M, the displacement, L_m, of the large grain is given by the following equation [5]:

$$L_m = M \cdot (3\Gamma/G) \cdot t \qquad (1)$$

where Γ is the grain boundary energy and t is the annealing time. The term, $3\Gamma/G$, is proportional to the pressure difference ($p = 4\Gamma/G$, assuming a spherical surface of radius $G/2$) across the grain boundary due to curvature and is the driving force for migration.

In the present experiment, the surface energy in Eqn. 1 is the interfacial energy between the vitreous phase in the solid and the aluminum oxide grains. If this interfacial surface energy could be assumed to be constant, then Eqn. 1 would apply exactly. However, as indicated by the facetting, the interfacial energy is not a constant and some discussion of the effect of surface energy anisotropy on growth is warranted. Equation 1 can be shown to be valid for solids in which the grains are completely wetted by a liquid, provided that

all grains maintain their equilibrium shape during growth. In this case, the chemical potential of the grains in the liquid is given by $4\Gamma_i V_m/G_i$, where the subscript i indicates that the interfacial energy and the grain dimension, G_i, refers to one of the facets of the grain, and V_m is the molecular volume of the solid. The grain dimension, G_i, is measured perpendicular to the facet. As a consequence of the Wulff theorem [12], Γ_i/G_i for each grain is a constant, so that the surface energy and grain width for any of the facets of the grain can be used in Eqn. 1.

When a facetted single crystal grows into a polycrystal containing a low fraction of liquid phase, the growth rates of different faces and the physical constraints on the crystal are such that the grains will have shapes that differ substantially from the equilibrium shape. Various factors such as densities of growth ledges on close-packed faces may limit growth. In addition, the pressure of adjacent grains on one another may prevent the crystals from realizing their final equilibrium shape [13], and, as a consequence, will increase the chemical potential of the constrained grains within the polycrystalline solid over that of unconstrained crystals in solution. Thus, large variations in local driving force for dissolution and growth are expected, leading to uneven growth of the sapphire crystals into the alumina composites.

Because the boundaries of grains have random orientation and shape, Eqn. 1 can be used phenomenologically to calculate an average mobility, but should be used with the understanding that the local motion of the interface is expected to depend on the shape, size and orientation of the individual grains, and on the particular constraints to which each grain is exposed. As the driving force for crystal growth in Eqn. 1 depends only on the grain size of the alumina, differences in interface velocity can be attributed to first approximation to differences in interface mobility of the growing sapphire alone. Using equation 1, the interface motion shown in Figs.3, 4 and 7 can be analyzed. For a-axis sapphire growth into AD96 after 24 hours at 1600°C, a mobility of $\approx 1\text{x}10^{-14}$ $m^3/N{\cdot}s$ is obtained for an average grain size of ≈ 10 μm and a value of $0.3 J/m^2$ for Γ.[4] This value of the mobility is approximately one-fifth of the value, $5.4 \text{ x } 10^{-14}$ $m^3/N{\cdot}s$ obtained by Monahan and Halloran [5] for growth of single crystal sapphire rods at 1672°C in a direction approximately

[3]This conclusion is reached by using Eqn. 666 in Ref.11

[4]This value of Γ is the value used by Monahan and Halloran and in earlier calculations in the literature.

normal to the (0001) into undoped alumina contaminated with glass. This difference in mobility is probably attributable to differences in temperature and composition of the glass within the alumina. Based on the interface velocity data in Fig.4, it can be concluded that the apparent mobility of the c-plane of the sapphire is one-third that of the a-plane. As the average grain size of the aluminum oxide and the compositon of the glass adjacent to the sapphire were independent of the orientation of the sapphire, this difference in apparent mobility of the a- and c-interfaces cannot be attributed to a transport controlled mechanism, but must be a consequence of differences in the kinetic processes at the two types of sapphire interface.

The dependence of growth rate on crystal orientation was demonstrated earlier by Kaysser et al. [6]. Examination of specimens by optical microscopy after sintering clearly demonstrated facetting and slow growth of the sapphire spheres along the basal plane during growth only when glass was present. The results of the present study confirm those of the earlier one, and furthermore demonstrate the presence of a continuous glass layer along the facetted basal plane in all cases studied, as was originally hypothesized by Kaysser et al.

The planar (0001) growth-interfaces, observed here and in reference 6, can be explained qualitatively if it is assumed that the interface formed by contact of the basal plane with silicate glasses is the lowest energy interface for sapphire; i.e., the basal interface corresponds to the deepest minimum or possibly a cusp in the Wulff plot for this structure. That this assumption is probably true, is justified by the fact that the plate-like crystals that develop during exaggerated grain growth in vitreous bonded systems are often bounded by basal planes. Moreover, basal planes form prominent habit planes on natural crystals, solution-grown crystals, and micro-facetted surfaces. If the basal plane has a lower surface energy relative to all other planes, then the number of steps on this plane will be minimized in order to minimize the total energy of the surface and, for the same reason, growth should occur by the lateral motion of the steps, i.e. a ledge growth mechanism. In this regard, the basal growth interfaces are found to contain ledges with a spacing larger than the grain size, which appear to correspond to growth ledges, Fig.6c. Thus, the basal plane will remain flat while it grows, and, since new material is added primarily at the surface steps, the rate of growth will be slow, because of the low concentration of these steps. Conversely, the formation of growth steps on planes having relatively high surface energies is more favorable, since these

growth steps can have a lower surface energy and, as a consequence, lower the total energy of the surface by facetting (see reference 14 for a discussion of facetting of high energy surfaces).

Aluminum oxide grains adjacent to the growing interface will also influence the shape of the growth interface. As these crystals vary in size and shape and have random orientations relative to the growing crystal, the chemical potential of the grains (based on size and shape alone) will vary along the matrix grain-liquid interface. The growth rate along the advancing sapphire will be uneven because of this variation of the chemical potential of the aluminum oxide grains from point to point along the interface. If the sapphire growth surface is free to change shape without substantially increasing the interfacial free energy, as it does for a-axis growth, then grains with some orientations will rapidly dissolve in the glass and re-precipitate on the sapphire surface to form a rough interface such as those seen in the present study. If grains adjacent to the a-axis sapphire dissolve fast enough, then grains with the slowly dissolving faces (grains bounded by (0001) planes) will become entrapped in the sapphire and be left behind by the advancing front to dissolve later or to remain in apparent metastable equilibrium. By contrast, growth of c-axis sapphire, as discussed above, will limit the migration of the interface and the flatness of the basal surface will be maintained regardless of the size, shape or orientation of the alumina grains across the glass layer. In this manner, many of the microstructural features observed in the current paper can be explained. Quantitative aspects of the microstructure will require additional theoretical investigation.

From the data on the composition dependence of growth rate anisotropy, it is clear that the composition, as well as the amount of glassy phase, affects growth. The growth of the a-axis sapphire was approximately the same for both aluminas, but the advance of the c-axis sapphire into AD96 was a factor of three slower than that of the a-axis and the advance of the c-axis into FF99 was a factor of nine slower than that of the a-axis. Both theory and experiment on flux growth of crystals indicate that the composition of the flux, in our case a silicate-based flux, can change the growth rate anisotropy, the facet planes, and the adsorption of impurities on crystal faces during growth. For example, sapphire grown in PbF_2 solutions with Mg, Mn, Ti, Cr, or Fe dopants exhibit dopant incorporation only in certain crystal directions, the amount of dopant incorporated also being a function of orientation [15]. In

other studies, the growth shapes of sapphire in PbF_2-Bi_2O_3 fluxes change from (0001) platelets in the undoped melt to a more equi-dimensional shape with facets on $(01\bar{1}2)$, (0001), and $(10\bar{1}1)$ planes with La_2O_3 additions [16].

In the two aluminas examined here, the change in growth rate anisotropy cannot, at this stage, be attributed with certainty to a difference in a specific impurity. However, from the measured compositions of the glasses located between grains of Al_2O_3, the impurities most important in promoting anisotropic growth in alumina in the present study can be ascertained. In both cases we are dealing with multicomponent, alumina- rich systems with three phases in equilibrium: alumina, spinel, and a liquid, but the compositions of the two liquids are significantly different and depend on the overall composition of the alumina. The most significant compositional difference between the glasses bonding the aluminum oxide grains is in the calcium and magnesium concentrations. For the AD96: $CaO/SiO_2 = 0.10$; $MgO/SiO_2 = 0.23$; for the FF99: $CaO/SiO_2 = 0.33$; $MgO/SiO_2 = 0.13$. Therefore, the concentration of CaO in FF99 is $\approx$3 times that in the AD96, whereas the concentration of MgO in FF99 is $\approx 1/2$ that of the AD96. The presence of CaO and SiO_2 have previously been observed to promote anisotropic growth of alumina. By contrast, additions of MgO to alumina containing CaO and SiO_2 tended to decrease anisotropy [6, 17]. Based on the EDS analysis of glass compositions, this decrease in anisotropic growth with higher MgO and lower CaO concentrations is also observed in our study. Other elements present in the glass (Na, K, Li) may also play a role in the determination of growth morphology in alumina by extending the range of glass formation and by promoting higher solubilities of alkaline earth oxide in silicate glasses. However, these effects still remain to be explained as nothing definitive can be said regarding the effect of these elements on growth morphology. To isolate quantitatively the effects of various components of silicate-based fluxes on growth anisotropy, growth studies similar to the ones discussed here are suggested, using ultra-clean starting powders and clean room processing to control composition and purity level.

The liquid entrapment that was observed is consistent with the calculations and experimental observations of Voorhees and Schaefer [18] on the instability of the growing interface. Our system is analogous to theirs: two solid grains are separated by a liquid layer and migration of the liquid layer occurring by dissolution of one grain and precipitation onto the other grain. The

growing interface is unstable with respect to small perturbations due to the divergence of the diffusional fluxes, identical to the case of a freezing interface during solidification. The presence of the dissolving interface across the liquid layer stabilizes the growing interface, and the degree of stabilization increases as the thickness of the liquid layer decreases. During growth of the sapphire, the glass layer will increase in thickness as glass (located originally between grains that have dissolved) is added to the interface between the sapphire and the matrix. When the layer reaches a critical thickness the growing interface becomes unstable and pockets of glass are left behind in the sapphire. This reduces the layer thickness, so that the growing interface is stable again until sufficient additional dissolution of the aluminum oxide grains occurs. In this way the glass layer reaches a maximum thickness, rather than increasing without limit as the small grains dissolve. In addition, if the wavelength of the perturbation is large compared with the grain size, small grains can be entrapped when the growing interface becomes unstable. These small grains will dissolve at a later time.

This study is not the first to report the formation of liquid inclusions during the growth of sapphire. Janowski et al. [19] observed liquid entrapment under most growth conditions using PbF_2-Bi_2O_3 and BiF_3-Bi_2O_3 melts; entrapment was most prevalent for fast growth conditions and for a platelet morphology, i.e. the grain morphology we observe in our experiments. It is important to note that examples in crystal growth, such as liquid entrapment and solute adsorption, can be used to good advantage to explain phenomena observed during grain growth in the presence of a liquid phase.

SUMMARY

This paper presented a study of interface migration in vitreous bonded aluminum oxide. In the course of experiments, in which sapphire of either a-axis or c-axis orientation was held against two commercial grades of fine grain vitreous bonded aluminum oxide, the migration rate of the sapphire was measured and the morphologies of the sapphire-glass and the matrix grain-glass interfaces determined. The interface mobility of the a-axis orientation was at least 3 times that of the c-axis orientation for the commercial aluminas studied. The interface mobility also appeared to depend strongly on the chemical composition of the glass in the alumina as well as on the orientation of the sapphire. From the observations of facetting at the glass-alumina interfaces

and the orientation and composition dependencies of growth, the migration of the sapphire interface is believed to be interface rather than transport limited. The growth kinetics of the c-axis oriented interface resulted in a relatively planar interface which was attributed to a low density of growth ledges on the basal plane. The relatively nonplanar interface formed for the a-axis orientation was attributed to local variations in the chemical potential of the alumina due to random orientations of the alumina grains across from the growing a-axis sapphire. In particular, grains with basal planes facing the sapphire dissolve very slowly compared with their neighbors. These grains become entrapped in the growing sapphire as their neighbors dissolve. Finally, entrapment of liquid droplets behind the a-axis interface is consistent with the absence of a liquid build-up in front of the advancing sapphire interface, and can be explained by the theory of Voorhees and Schaefer. For many of these phenomena, the crystal growth literature has provided useful analogues which aid in our understanding of grain growth processes in the presence of a liquid phase.

REFERENCES

1. A. Mocellin and W.D. Kingery, "Microstructural Changes During Heat Treatment of Sintered Al_2O_3," J. Am. Ceram. Soc. **56**, 309-14 (1973).

2. S.J. Bennison and M.P. Harmer, "Effect of MgO Solute on the Kinetics of Grain Growth in Al_2O_3," J. Am. Ceram. Soc. **66**, C90-C92 (1983).

3. S.J. Bennison and M.P. Harmer, "Grain-Growth Kinetics for Alumina in the Absence of a Liquid Phase," J. Am. Ceram. Soc. **68**, C22-C24 (1985).

4. M. Kinoshita, "Boundary Migration of Single Crystal in Polycrystalline Alumina," Yogyo Kyokaishi **82**, 295-29[illegible] (1974).

5. R.D. Monahan and J.W. Halloran, "Single-Crystal Boundary Migration in Hot-Pressed Aluminum Oxide," J. Am. Ceram. Soc. **62**, 564-567 (1979).

6. W.A. Kaysser, M.Sprissler, C.A. Handwerker and J.E. Blendell, "Effect of a Liquid phase on the Morphology of Grain Growth in Alumina," J. Am. Ceram. Soc. **70**, 339-343 (1987).

7. C.A. Handwerker, P.A. Morris, and R.L. Coble, "Effects of Chemical Inhomogeneities on Grain Growth and Microstructure in Al_2O_3," J. Am. Ceram. Soc., to be published January, 1989.

8. S.M. Wiederhorn, B.J. Hockey, R.F. Krause, Jr. and K. Jakus, "Creep and Fracture of a Vitreous-Bonded Aluminum Oxide," J. Mater. Sci. **21**, 810-824 (1986).

9. S.C. Hansen and D.S. Phillips, "Grain Boundary Microstructures in a Liquid-Phase Sintered Alumina (α-Al_2O_3)," Phil. Mag. A, **47**, 209-234 (1983).

10. For example, see R.J. Brook, "Controlled Grain Growth," pp. 331-364 in *Treatise on Materials Science and Technology*, Vol. 9, F. F. Y. Wang, eds., Academic Press, New York (1976).

11. J. W. Gibbs, *The Scientific Papers of J. Willard Gibbs*, Dover Publications, Inc. New York, (1961).

12. A discussion of the Wulff construction was given by C. Herring, pp.5 to 81 in *Structure and Properties of Solid Surfaces*, R. Gomer and C.S. Smith eds., The University of Chicago Press, Chicago (1953).

13. P.L. Flaitz and J.A. Pask, "Penetration of Polycrystalline Alumina by Glass at High Temperatures," J. Am. Ceram. Soc. **70**, 449-455 (1987).

14. J.W. Martin and R.D. Doherty, *Stability of Microstructure in Metallic Systems*, Cambridge University Press, Cambridge (1976).

15. C.A. Wallace and E.A.D White, The Morphology and Twinning of Solution-Grown Corundum Crystals, pp. 431-435 in *Crystal Growth*, Ed. H. S. Peiser, Pergamon Press, Oxford (1967).

16. A.B. Chase, "Habit modification of corundum crystals grown from molten PbF_2-Bi_2O_3," J. Am. Ceram. Soc. **49**, 233-236 (1966).

17. H. Song and R.L. Coble, "Liquid phase sintered Al_2O_3: I, Origin and growth kinetics of plate-like abnormal grains," J. Am. Ceram. Soc. submitted.

18. P.W. Voorhees and R. Schaefer, Personal Communication.

19. K. R. Janowski, A. B. Chase, and E. J. Stofel, Growth defects in flux-grown rubies, Trans. AIME **223**, 2087-2091 (1965).

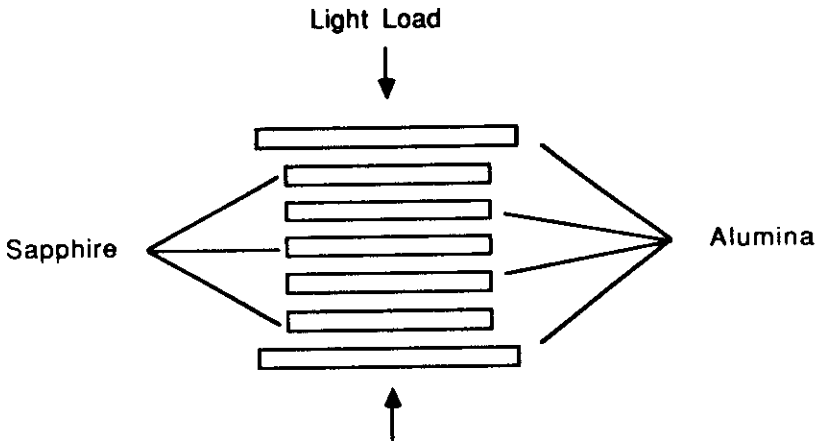

Figure 1. Experimental technique for bonding alumina to sapphire. The applied stress was less than 0.1 MPa, which is less than the value of 1 MPa usually accepted for the sintering stress, so that effects of stress on the sintering process is expected to be minimal. Each stack would have at least two different orientations of sapphire, and one or more grades of alumina.

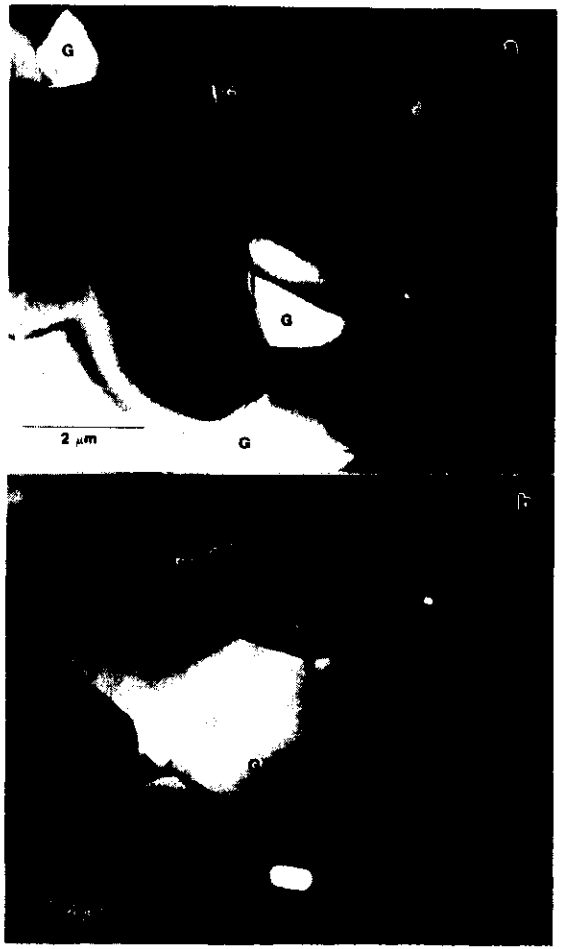

Figure 2. Transmission electron micrographs of the as-received aluminas: (a) Coors AD96; (b) Friedrichsfeld FF99. The AD96 has a larger grain size ≈8 μm than the FF99, ≈3 μm, and contains more glass, ≈8 versus ≈1 vol.% respectively. Consequently, the alumina grains in the AD96 are completely surrounded by glass, and large pockets of glass can be seen in the AD96. By contrast, the glass in the FF99 only appears in relatively small triangular triple junctions.

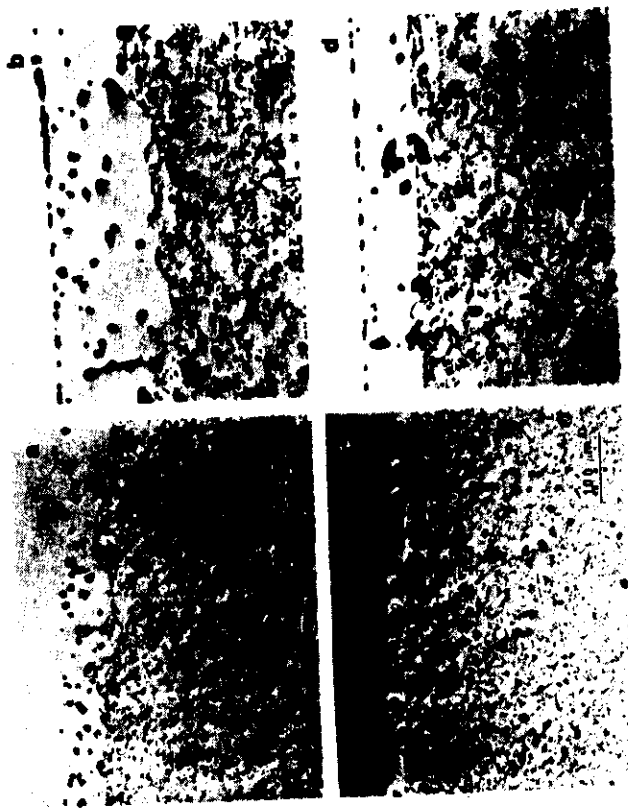

Figure 3. Growth of sapphire into Coors AD96 alumina as a function of time and orientation at 1600°C. The two figures on the left represent 16 hours exposure, the two on the right 69 hours exposure. The upper two figures are the a-axis orientation, the lower two the c-axis orientation. The following features should be noted: grain encapsulation, mainly spinel; glass encapsulation; the relatively rough interface formed by the a-axis orientation compared to the much flatter interface for the c-axis orientation.

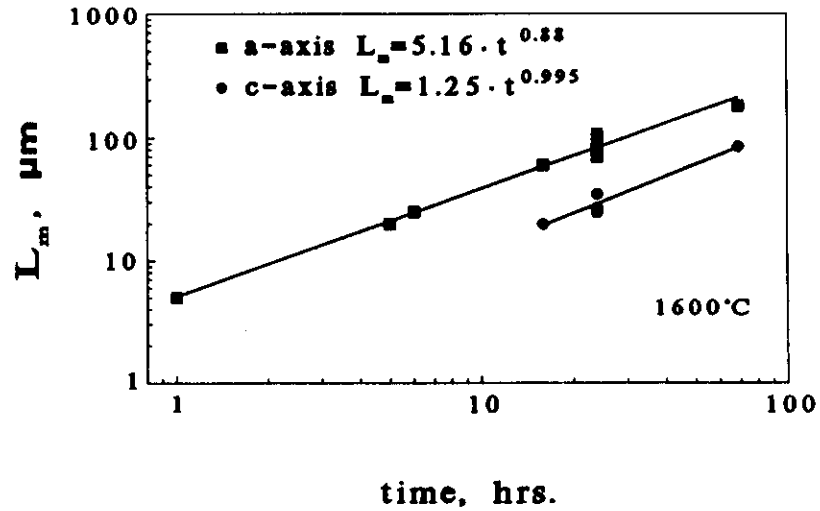

Figure 4. Total interface migration for Coors AD96 as a function of annealing time at 1600°C. The migration for the a-axis direction in the AD96 was approximately three times that of the c-axis orientation indicating a higher mobility for the a-axis growth direction.

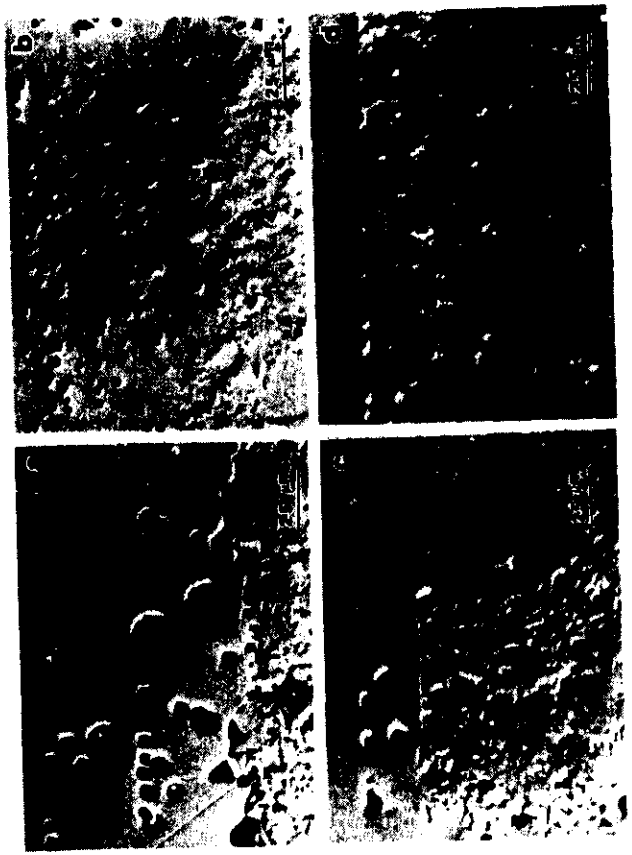

Figure 5. Growth of sapphire into alumina as a function of commercial grade and sapphire orientation, 24 hours exposure at 1600°C. The two figures on the left are Coors AD96; the two on the right are Friedrichsfeld FF99. The upper two figures are the a-axis orientation; the lower two are the c-axis orientation. The advance of the sapphire into the aluminas was about the same for the a-axis orientation. By contrast, the advance of the sapphire into the alumina for the c-axis orientation was much greater for the Coors AD96.

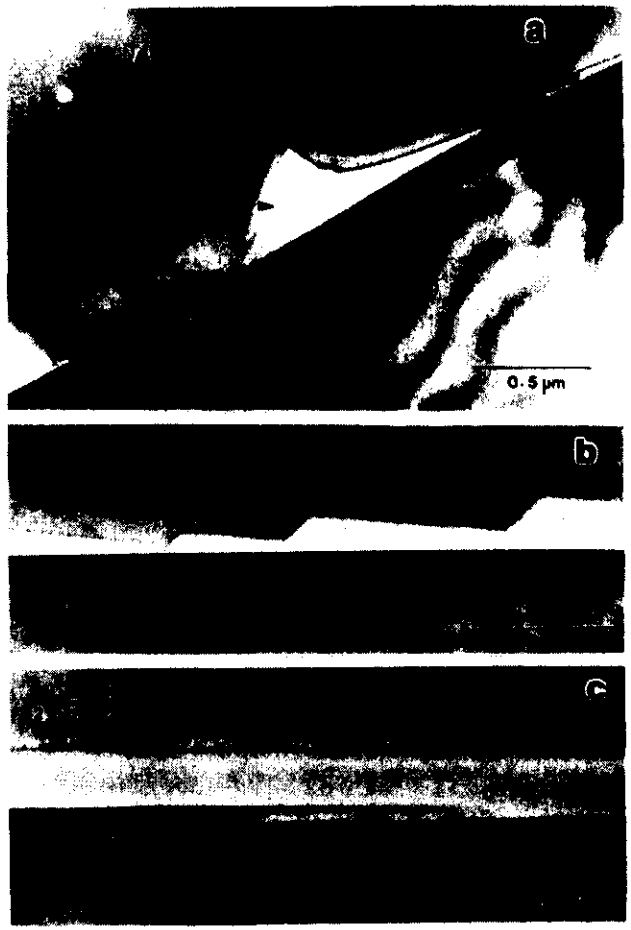

Figure 6. Growth interface after migration of c-axis sapphire into AD96 alumina at 1600°C. In each figure, the growth direction is from the bottom to the top of the figure. Over the entire interface, a narrow glass layer separates the growing sapphire and dissolving alumina grains. The sapphire growth surface is planar on (0001) except for isolated growth steps, while adjacent alumina grain surfaces are either planar or facetted depending on their orientation.

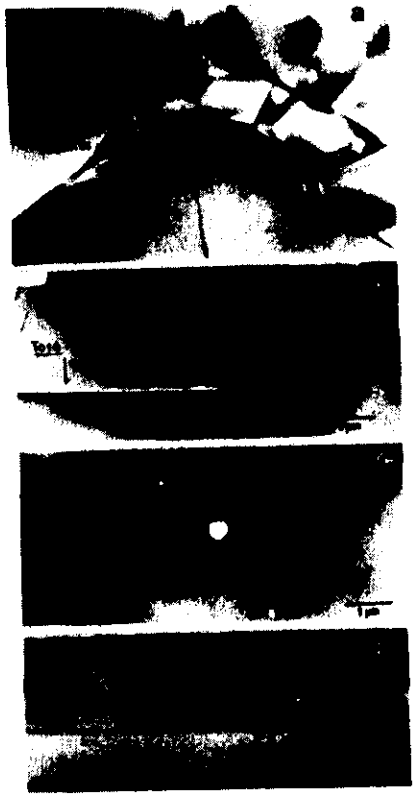

Figure 7. A number of significant features associated with the growth of the a-axis sapphire into AD96 at 1600°C are shown in the above micrographs: (a) portion of irregular interface formed by migration of the a-axis sapphire into the AD96. Typically, variations in migration rate and interfacial morphology were found from grain to grain; (b) Tabular alumina grain with (0001) basal plane situated at migration boundary. Note the flatness of the (0001) grain surface, entrapped glass, and concave curvature of migrating a-axis sapphire; (c) Tip of a tabular grain nearly fully encapsulated by the migrating a-axis sapphire. Little glass is apparent at the interface; (d) Linear portion of migrating boundary. The migrating a-axis sapphire has developed a planar $(12\bar{1}0)$ surface, while the adjacent alumina grain surface has also developed facets.